Pressure based active load control of a blade in dynamic stall conditions

TU Delft

Jorge Fernández Barrio

Pressure based active load control of a blade in dynamic stall conditions

by

Jorge Fernández Barrio

to obtain the degree of Master of Science
at the Delft University of Technology,
to be defended publicly on Friday March 20, 2020 at 09:00 AM.

Student number:	4632311	
Project duration:	October 8, 2018 – March 20, 2020	
Thesis committee:	Dr. ir. B. W. van Oudheusden,	TU Delft, supervisor and chair of committee
	Dr. A. Sciacchitano,	TU Delft, supervisor
	Dr. D. Ragni,	TU Delft, committee member
	Ir. C. Mertens	TU Delft, supervisor

An electronic version of this thesis is available at http://repository.tudelft.nl/.

TU Delft

Preface

There have been so many times when I have imagined myself writing this, that actually doing it feels unreal. Even though this is meant to be the preface, these words actually mark the end of a chapter of my life. The journey that brought me here has been full of ups and downs, and has led me through paths that I could never have imagined. I hope to have learned from this experience, and to use this new-found knowledge about myself in the chapters that are to come.

A lot of people has helped me in one way or another throughout this journey. I want to thank Bas, Andrea and Dani, for all the feedback, the time, and dealing with my lack of planning during all these months. Special thanks go to Christoph. For understanding when I needed to be pushed, and when I needed reassurance. For being so unphased even when things did not work out. Thanks for all that and more.

To the down under and its people. I think every single one of you has heard my rants about the basement. My complaints about the place were not indicative of my feelings towards you. There is so many people that have been a really important part of this journey stemming from here that is impossible to mention all of you, although I feel the need to name a few: Dorian, Joel, Niels, Carlos, Tomás, Chris. To you, and to the ones I did not mention, you did more than you think.

It is impossible to write my acknowledgements and leave out one of my most important support groups during this time. Having you around has made this much easier, you have no idea how much. Sara, Jeroen, David, Carlos, Coco, Joan, Spyros. For all the experiences, the beers and the climbing. I'm sure there is more of those in the future.

This last paragraph has to include one of my closest friends, and ever-lasting flatmate, Iñigo. There is few people that know me more than you do, and that knows my journey more closely. Could not thank you enough for being there. Finally, the most important people in my life: family. I know sometimes it must feel like I take you for granted. But I could not be more blessed and privileged to have you in my life. You are my safe place, the people I can go to for comfort, and if life was fair half of this thesis would just be about you. Papá, Mamá, Sandra. Gracias.

Jorge Fernández Barrio
Delft, March 2020

Abstract

A proportionate controller is investigated experimentally for unsteady load alleviation purposes on a 2D wing model with a trailing-edge flap. This study is supposed to be a simplified version of a Smart Rotor, a mechanism which deals with the reduction of unsteady loads acting on a wind turbine, and aims to understand the behaviour of this type of control under dynamic stall conditions. The controller acts on the velocity of the flaps, and pressure sensors are used to detect the unsteady loads, which are generated by actuating the wing model in a sinusoidal motion. Two different regimes are considered: attached flow (oscillations around zero angle of attack, where little flow separation is expected) and dynamic stall (oscillations close to the static stall angle). The influence of actuation frequency and controller time lag is also studied, as these parameters were found to be crucial for such a concept during the literature review. A reduction of 87.5% in the standard deviation of the lift is obtained for a frequency of 0.2Hz and time lag in the control system of 12ms for attached flow conditions. The reduction of the standard deviation of the lift deteriorates for increased frequency and time lag. The proposed controller is also able to reduce the loads during dynamic stall, although the reduction is smaller, close to 40% in the reduction of the lift coefficient. A maximum reduction of 59% in the peak-to-peak loads experienced during dynamic stall is observed, for 0.2Hz and a time lag of 12ms. Time lag is again crucial for this reduction, and larger and faster actuation systems are needed to fully compensate for the larger drop in loads. However, the active load control of the loads during dynamic stall can negatively affect the aerodynamic damping of the model since the flap reacts to the detachment of the dynamic stall vortex from the surface of the airfoil. The flap actuation is also shown to delay the onset of dynamic stall, by increasing the static stall angle with respect to the case without flap deflection.

Contents

List of Tables

List of Figures

Nomenclature

Symbols

α	Angle of attack of the airfoil	[°]
α_0	Mean angle of oscillations	[°]
α_t	Geometric angle of attack	[°]
α_{amp}	Amplitude of the oscillations	[°]
β	Flap Angle	[°]
$\ddot{\alpha}$	Pitching acceleration	$[°/s^2]$
$\ddot{\beta}$	Flap acceleration	$[°/s^2]$
$\ddot{h}$	Heaving acceleration	$[°/s^2]$
Δf	Force acting on airfoil panel per unit span	[N/m]
Δp	Pressure difference between upper and lower surface	[Pa]
Δs	Panel length	[m]
Δt_{DS}	Time elapsed from the static stall angle to the onset of dynamic stall	[s]
Δx	Panel length in x-coordinate	[m]
Δy	Panel length in y-coordinate	[m]
$\dot{\alpha}$	Pitching velocity	$[°/s]$
$\dot{\beta}$	Flap velocity	$[°/s]$
$\dot{h}$	Heaving velocity	$[°/s]$
ϵ	Blade Root Bending Moment	[N.m]
ϵ'	High-pass filtered Blade Root Bending Moment	[N.m]
μ	Air viscosity	[kg(m·s)]
ρ	Air density	[kg/m^3]
τ	Time constant	[-]
θ	Angle of airfoil panel with respect to the normal axis	[°]
$\Xi_{cycle,0}$	Aerodynamic damping of the baseline case	[-]
$\Xi_{cycle,f}$	Aerodynamic damping contribution due to the flap actuation	[-]
Ξ_{cycle}	Aerodynamic Damping over one cycle	[-]
A	Wind turbine rotor swept Area	[m^2]
a_t	Non-dimensional distance from half point of the plate to the pitching axis	[-]
AR	Aspect Ratio	[-]

b_t	Half-chord	[m]
B_{C_l}	Bias error of the lift coefficient	[-]
B_{C_m}	Bias error of the moment coefficient	[-]
c	Airfoil chord	[m]
$C(k)$	Theodrosen Function	[-]
C_l	Lift Coefficient	[-]
C_m	Moment coefficient around the pitching axis	[-]
C_P	Wind Turbine Power Coefficient	[-]
C_p	Pressure coefficient	[-]
c_t	Non-dimensional distance from half point of the plate to the hinge-point	[-]
$C_{l,max}$	Maximum value of the lift coefficient for each cycle	[-]
$C_{l,min}$	Minimum value of the lift coefficient for each cycle	[-]
$C_{m,0}$	Moment coefficient of the baseline case	[-]
$C_{m,f}$	Moment coefficient contribution due to the flap actuation	[-]
DS_{onset}	Phase of dynamic stall onset	[-]
$e(t)$	Error signal	[-]
EQ_f	Single equivalent load	[N]
f	Frequency of oscillations	[Hz]
$F(s)$	Actuation signal	[°]
h	Heaving position	[m]
h_t	Wind tunnel height	[m]
k	Reduced frequency of oscillations	[-]
K_d	Derivative Gain	[-]
K_i	Integral Gain	[-]
K_p	Proportional Gain	[-]
L	Lift	[N]
M	Moment around the pitching axis	[N.m]
m	Moment around the pitching axis of the airfoil per unit span	[N]
n	Normal force acting on the airfoil per unit span	[N/m]
N_c	Number of calibration runs	[-]
N_p	Number of airfoil panels	[-]
N_{cycles}	Number of cycles for each case of the experiment	[-]
p	Pressure	[Pa]
P_w	Wind Turbine Power	[Watt]

r	Reduced pitch rate	[N]
r_f	Radial position of the flap	[m]
r_s	Radial position of the sensor	[m]
Re	Reynolds number	[°]
s	span	[m]
$S_{\overline{C_l}}$	Precision index of phase-averaged lift coefficient	[-]
$S_{\overline{C_m}}$	Precision index of phase-averaged moment coeffiecient	[-]
t	Student's t distribution	[-]
u	Set point	[-]
$U_{\overline{C_l}}$	Uncertainty at 95% confidence of the phase-averaged lift coefficient	[-]
$U_{\overline{C_m}}$	Uncertainty at 95% confidence of the phase-averaged moment coefficient	[-]
V	Air Velocity	[m/s]
V_∞	Free-stream velocity during the experiments	[m/s]
W	Work done on the airfoil	[J]
$X(s)$	Process Variable	[-]
$x*$	Non-dimensional distance in x-coordinate	[-]
x_m	X-coordinate of the pitching axis	[m]
x_p	X-coordinate of pressure tap	[m]
$y*$	Non-dimensional distance in y-coordinate	[-]
y_m	Y-coordinate of the pitching axis	[m]
y_p	Y-coordinate of pressure tap	[m]

Acronyms

1P	One time Per revolution
2D	Two-Dimensional
2D	Two-Dimensional
2P	Two times Per revolution
3D	Three-Dimensional
3P	Three times Per revolution
AC	Alternating Current
ATEG	Adaptive Trailing Edge Geometry
DAQ	Data Acquisition System
DEL	Damage Equivalent Loads
DOF	Degree of Freedom
ETM	Extreme Turbulence Model

HAWC Horizontal Axis Wind turbine simulation Code

HSL High Speed Laboratory

IEC International Electrotechnical Commission

ILC Iterative Learning Control

LEV Leading Edge Vortex

LQR Linear Quadratic Regulator

LTI Linear Time Invariant

LTV Linear Time Variant

MBC Multi Blade Coordinate

MIMO Multiple-Input Multiple-Output

MPC Model Predictive Control

NACA National Advisory Committee for Aeronautics

NREL National Renewable Energy Laboratory

NTM Normal Turbulence Model

OJF Open Jet Facility

PID Proportionate Integral Derivative

PIV Particle Image Velocimetry

PV Process Variable

SP Set Point

VFD Variable Frequency Drive

Subscripts

i Panel number

l Lower surface

u Upper surface

x X coordinate

y Y coordinate

1 Introduction

Windmills have been present for thousands of years, as a way of converting the energy present in the wind into mechanical energy. Horizontal-axis windmills, similar to the ones used nowadays, were introduced in Northern Europe around the 12th century, and were used for centuries to perform activities such as pumping water or grinding grain. However, with the advent of the Industrial Revolution in the 18th century, there was a drop in their use, since coal provided a more affordable way of obtaining energy, and it could be transported with more ease. For two centuries, the wind energy stayed on the background, while some advances were made by employing the newly invented electrical generators to directly introduce the wind energy into the electric grid. But by the end of the 20th century, a sudden increase in coal price, as well as the appearance of environmental concerns regarding the sustainability of the systems brought on by the Industrial Revolution, put the wind energy back into the main stage of energy generation. Wind turbines emerged as a possible solution for obtaining energy in a clean and environmentally friendly way.

The new challenges brought forward by the increasing demand of energy worldwide require of alternative ways of producing energy. The Paris Agreement was signed by 195 countries across the world in 2016, and plans to limit the effects of global warming by keeping the increase in global mean temperature under 2° above the pre-industrial levels. Traditional means of energy production are no longer valid, and alternative and renewable ways of producing energy must be the in the forefront of energy production. One of the most promising and rapidly growing ways of producing renewable energy is wind energy, which has experienced an incredible growth. As an example, the global installed capacity in Europe changed from 11.1 GW in the year 2000 to 153.7 GW in 2016 [23].

Wind energy taking a prominent role in the energy production is accompanied by research into more efficient ways of extracting the energy. Wind turbines are devices that convert the energy present in the wind into mechanical energy first, and ultimately into electrical energy. When the air passes through the blades it generates an aerodynamic loading that makes the rotor spin, and this rotation is transformed into electricity with a generator. For a given wind turbine, the power output can be defined as a function of the air velocity (V), the area swept by the rotor (A), the air density (ρ) and the power coefficient (C_p):

$$P_w = \frac{1}{2} C_P \rho A V^3 \tag{1.1}$$

The power coefficient (C_P) is a measure of the energy present in the wind that is actually transformed into mechanical power. The maximum achievable value for this coefficient is 0.593, given by the Betz limit [14], and real wind turbines only reach a fraction of this ideal value. Increases in wind energy production can be made by increasing the power coefficient through more efficient designs. However, it appears that in order to increase the power production of a wind turbine, the most logical solution is to increase its size. The power produced by a wind turbine scales with the square of the rotor diameter, so increasing its size is a very efficient way to increase the power output. As such, this has been the dominant trend established in the wind energy industry since its beginnings. Wind turbines have constantly been becoming larger and larger, and the power output has been increasing

accordingly, as it can be seen in figure 1.1.

The upscaling of wind turbines comes along with some challenges that need to be tackled. The loads and moments acting on the blades, as well as its weight [53] are increased. This increase in weight is specially important, since it results in a linear increase of the stress due to gravitational loads [53]. Lighter structures are needed if larger turbines are to be manufactured. However, wind turbines are the subject of unsteady inflow conditions, which generate unsteady loading on the turbine itself. Reducing the weight of the different components of the wind turbine might make them susceptible to fatigue damage. Examples of mechanisms responsible for the generation of unsteady loads on the blades are wind shear, turbulence or tower shadow. Reducing these unsteady loads would allow for the use of lighter materials in the construction of the blades, and for manufacturing larger wind turbines, which translates into an increase of the power extraction capabilities.

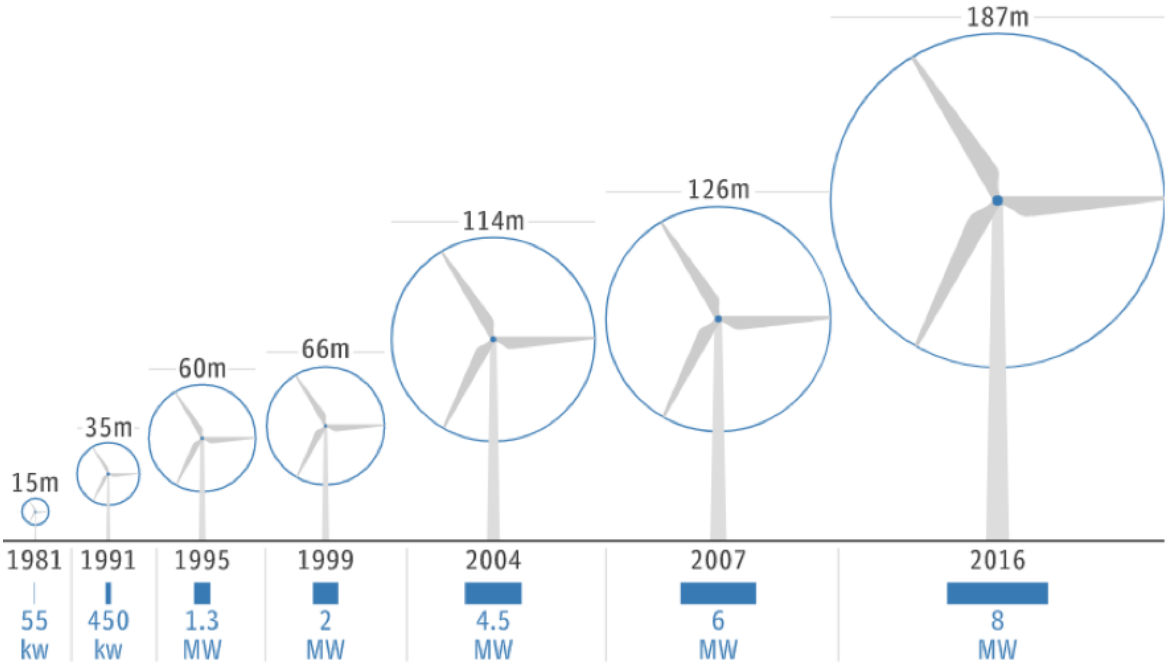

Figure 1.1: Evolution of wind turbine diameter size and power capacity from 1981 to 2016 (reproduced from https://northsearegion.eu/northsee/e-energy/future-energy-industry-trends/)

The Smart Rotor appears as a possible solution for the reduction of unsteady loads on a wind turbine. The idea behind the Smart Rotor concept is the active modification of the blade shape to reduce the unsteady loads acting on it. This is done by combining three elements: a sensing system, responsible of detecting the change in loads; a controller, which is in charge of reacting to these loads; and an actuation mechanism, that modifies the shape of the blade according to the output of the controller in order to achieve the desired load control. The benefits of this load reduction appear in the reduced fatigue experienced by the different components of the wind turbine, since the stress acting on them is reduced.

Several Smart Rotor concepts have been proposed, as it is laid out during chapter 2. However, most of these studies are focused on the optimal form of control, and some aspects, such as the performance of a Smart Rotor under dynamic stall conditions have not been studied yet. Dynamic stall is a highly unsteady flow phenomenon that can appear in wind turbines due to unsteady loading [52]. This phenomenon is responsible for large load oscillations during its development [41]. Although it only occurs in a small fraction of the cycles (estimated around 1-2% [52]), the magnitude of the unsteady loads is larger than compared to when this phenomenon does not occur. Therefore, these loads may be responsible for fatigue damage at a smaller number of cycles. If these loads are not tackled by the

Smart Rotor, the reduction in weight and increase in size could lead to unexpected fatigue damage.

This can be visualized in a SN curve, where the amplitude of an alternating stress is plotted against the number of cycles to failure at that given stress. During its life-span, a typical wind turbine may experience 10^8 to 10^9 cycles of periodic unsteady loads (appearing once per revolution), and this would correspond to around 10^6 to 10^7 cycles of dynamic stall based on [52]. The stress associated with these two different loadings is sketched in figure 1.2. Up until now, blades are thought to be over-dimensioned [45], which explains why damage due to fatigue loads is not common. If blades are made lighter, the stress experienced under the same loading is increased. A Smart Rotor tries to reduce these loads so that blades can be made lighter or larger while keeping the loads experienced by the blade below the failure curve. However, if dynamic stall loads are not reduced, the reduction in weight (or increase in size) may situate the dynamic stall loads on top of the failure curve.

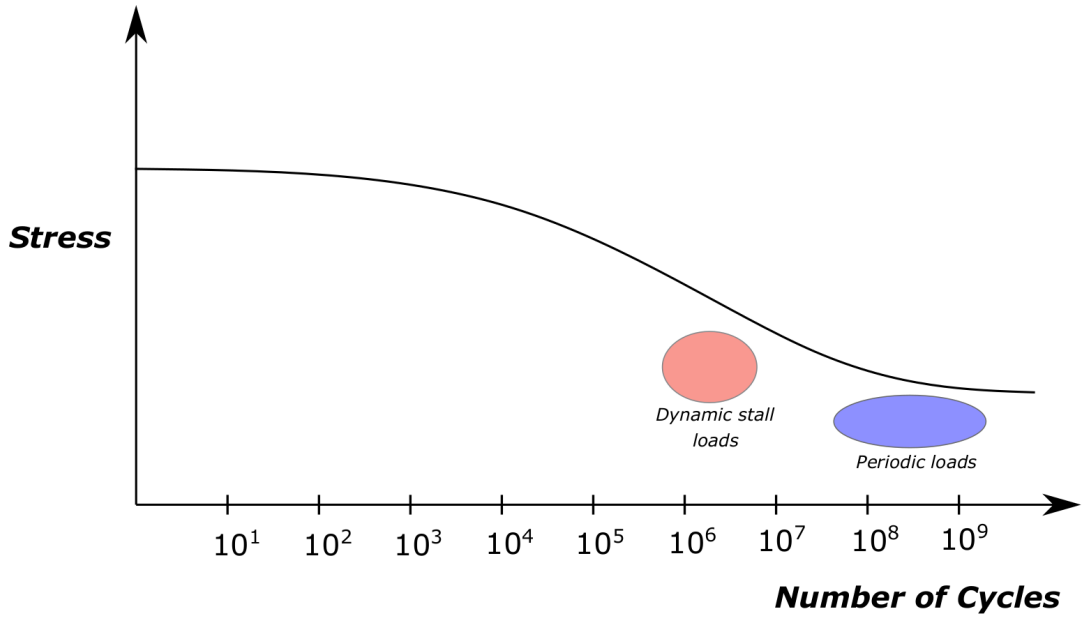

Figure 1.2: Sketch of a typical S-N curve, showing the approximated magnitude and number of cycles associated with dynamic stall and periodic loads

This motivates the present study, where the ability of a Smart Rotor to reduce the unsteady loads originated during dynamic stall wants to be studied. Since this is such a complex phenomenon, the present study tries to bridge this gap in knowledge by considering this phenomenon on a simplified rigid 2D-blade. The blade is subject to unsteady loading, representative of both a regime where small separation is expected (referred hereafter as attached flow), and a regime where dynamic stall occurs. A controller is designed to reduce the unsteady loads acting on the blade. The differences between the different regimes wants to be assessed, as well as the influence of parameters such as the time lag or the frequency of unsteadiness in the load reduction capabilities. The purpose of this thesis can thus be summarized in the research objective:

> *To assess the capabilities and limitations of an active controller in reducing the unsteady loads acting on a blade, by studying the load reduction achieved during attached flow and dynamic stall conditions, in terms of time lag, controller gains, and frequency of unsteadiness on a 2D experimental blade airfoil model.*

Chapter 2 is focused on the literature review of the present status of the Smart Rotor. This allows to identify the lack of studies done with this system under dynamic stall conditions, as well as the importance of parameters such as the time lag or frequency of unsteadiness in its load reduction capabilities. The necessary knowledge regarding unsteady aerodynamics is also presented here, since it is needed for the remainder of the thesis.

An experiment is performed in the Open Jet Facility (OJF) of the TU Delft in order to achieve the thesis objective, and described in chapter 3. A wing model obtained by extrusion of a 2D-airfoil is subject to a sinusoidal motion, at different frequencies. This is done by means of a pitching mechanism, which generates an unsteady loading on the blade, and by modifying the mean angle of oscillations conditions representative of both attached flow and dynamic stall can be achieved. Pressure sensors are installed in the model, which detect the unsteady loads, and feed it forward to a proportionate controller with variable gains. The controller generates an actuation signal that moves a trailing edge flap and reduces the unsteady loads.

The methodology employed in order to transform the raw data obtained during the experiment into a more meaningful form of data is presented in chapter 4. The output of the experiment is the instantaneous pressure data of the pressure transducers. This data is transformed into phase-averaged loads and moments acting on the blade, following this methodology. The procedures followed to analyse the data and determine the feasibility of the concept are also introduced here.

The baseline results, dealing with no active control of the loads are presented in chapter 5. These results serve as a point of comparison for the results with active load control, which are shown in chapter 6. During this chapter, the load reduction capabilities of the proposed controller are assessed, both during attached flow and dynamic stall conditions. The influence of the controller time lag and unsteadiness frequency is also studied, as they were found to be relevant in any mechanism dealing with active load control.

Finally, in chapter 7, conclusions and recommendations for future work are summarized based on the findings obtained in the previous chapters.

2

Background and Previous Work

The main purpose of this chapter is the identification of the relevant aspects in the Smart Rotor research, as well as the presence of any gaps in the knowledge that could be tackled with this thesis. A Smart Rotor deals with the reduction of the unsteady loads acting on a wind turbine, and as such, a discussion on unsteady aerodynamics is the focus of section 2.1. This discussion is focused specifically on the aspects to be studied during the experiment, namely the aerodynamics of a pitching airfoil. The phenomenon of dynamic stall is also described, which is the focus of the present study. During section 2.2, a review of the main studies done in the Smart Rotor research area is carried out. This allows to identify the lack of dynamic stall studies, which motivates the focus that was placed on this phenomenon during the first section. Along with this, the conclusions extracted from the previous review are presented in section 2.3. Based on these conclusions, several aspects are identified as important in any mechanism designed for load alleviation purposes and the research questions are formulated.

2.1. Unsteady Aerodynamics

Steady aerodynamics assumes that no temporal variations occur in the flow. This approach usually makes the study of flows much simpler, but it can be reasoned that this situation is impossible to find in real life. There is always going to be a certain degree of unsteadiness present in the flow. However, the unsteadiness of a flow, or its rate of change with time, can be so low that the assumption of steady aerodynamics may be valid for obtaining accurate results. A non-dimensional number, the reduced frequency, is typically used as the indicator of unsteadiness. For a pitching airfoil, oscillating at a frequency f, with chord c and freestream velocity V, the reduced frequency is defined as follows:

$$k = \frac{2\pi f c}{V} \tag{2.1}$$

For a pitching airfoil under attached flow conditions, the level of unsteadiness of the flow can be estimated based on the value of the reduced frequency. Flows with reduced frequencies larger than 0.05 are typically considered unsteady under these conditions. The time-dependent aspects of the flow play an important role in the resulting aerodynamics and cannot be ignored. Steady aerodynamics is therefore not valid anymore for the analysis of these kind of flows and new theories are needed.

2.1.1. Theodorsen Theory

Theodorsen [56] developed a theory that allows for the computation of the aerodynamic loads on an airfoil undergoing an oscillatory motion. This theory is based on the assumption of potential flow around a 2 dimensional flat plate, and divides the contribution to the aerodynamic forces into circulatory and non-circulatory terms. The starting point of the theory is a flat plate with three degrees of freedom: pitching motion of the whole plate (α), flapping motion of the flap (β), and heaving motion (h). A sketch of the flat plate and its degrees of freedom, as well as the parameters that define the plate is presented in figure 2.1. A solution based on the combination of several velocity potentials is obtained. First, the

velocity potentials due to the non-circulatory flow (due to the presence of the 3 DOF wing in the flow), are taken into account. After that, the circulatory velocity potentials (appearing as a result of the need to comply with the Kutta conditions) are considered, and a solution for the aerodynamic forces present in this 3 DOF flat plate is obtained. The lift and moment derived for a harmonic pitching motion have the following expressions:

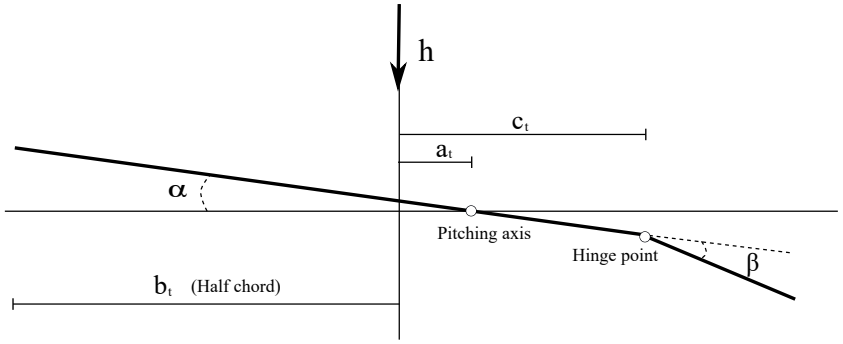

Figure 2.1: Sketch of the flat plate used for the derivation of Theodorsen Theory, adapated from [56]

$$L = \rho b_t^2 \left(V\pi\dot{\alpha} - \pi b_t a_t \ddot{\alpha}\right) + 2\pi\rho V b_t C(k)\left(V\alpha + b_t\left(\frac{1}{2} - a_t\right)\dot{\alpha}\right) \tag{2.2}$$

$$M = -\rho b_t^2\left(\pi\left(\frac{1}{2} - a_t\right)V b_t\dot{\alpha} + \pi b_t^2\left(\frac{1}{8} + a_t^2\right)\ddot{\alpha}\right) + 2\rho V b_t^2\pi\left(a_t + \frac{1}{2}\right)C(k)\left(V\alpha + b_t\left(\frac{1}{2} - a_t\right)\dot{\alpha}\right) \tag{2.3}$$

$C(k)$ is the Theodorsen function, and it consists of a real and an imaginary part. Theodorsen derived this term by the use of Bessel functions, and its value is dependent on the reduced frequency k.

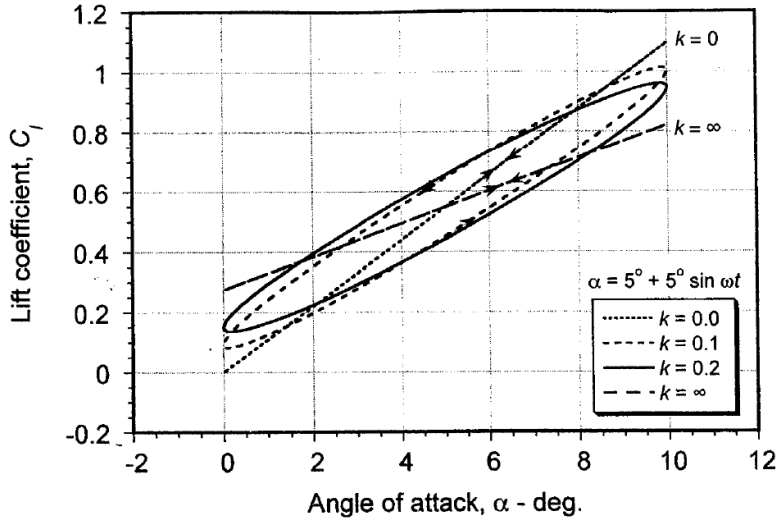

Figure 2.2: Lift coefficient as a function of the angle of attack obtained with Theodorsen Theory, for different reduced frequencies k [36]

Leishmann [36] derived this expression of the lift coefficient for a purely oscillating airfoil, as a function of the reduced frequency k, and can also be seen in figure 2.2. As the reduced frequency increases, the C_l is lower during the upstroke than during the downstroke for the same angle of attack. This effectively means a phase lag of the aerodynamic forces with respect to the oscillations. There also appears

a damping of the amplitude of the aerodynamic forces, that are reduced in half as k approaches infinity.

The correspondence of Theodorsen theory with experimental results is excellent for pitching motions, even for thick airfoils such as the NACA 0018, as it was shown by Stangfeld [54] for a Reynolds number of $Re = 3 \cdot 10^5$. However, oscillations around high angles of attack are not going to comply with the assumption of potential flow anymore, since separation is expected to occur, so Theodorsen's theory should not be used. These type of oscillations may induce more complex phenomena, such as dynamic stall.

2.1.2. Dynamic Stall

Dynamic stall is an important phenomena associated with unsteady aerodynamics. The flow around a steady airfoil separates completely from the surface at a certain angle of attack, known as the static stall angle. A stalled airfoil displays a decrease in lift, since the flow is not attached anymore to its surface, and a higher drag. Dynamic stall is the process by which an airfoil undergoing oscillatory motion reaches angles of attack larger than the static stall angle, generating a higher lift than its steady counterpart. This phenomena is associated with the appearance of a Leading Edge Vortex (LEV), which increases the circulation and delays the onset of the stall. Increasing the angle of attack beyond this point means that eventually the leading edge vortex will detach, generating a sudden drop in lift.

McCroskey [42] identified three different regimes of dynamic stall. The appearance of one of the different regimes depends on the maximum angle of attack reached during the oscillations: The first regime is called stall onset, for angles of attack sligthly larger than the static stall angle. A larger lift is obtained with respect to the steady counterpoint, but no remarkable penalties in terms of drag or pitching moment changes are observed, since the separation of the flow is limited. If the angle of attack is a bit larger, considerable separation is observed, in the order of the airfoil thickness. This regime is labeled as light stall. Deep stall is the last regime of dynamic stall defined, that occurs when the maximum angle of attack exceeds the static stall angle considerably. The separation is complete, and the drop in lift and change in pitching moment is much larger.

The typical evolution of a deep dynamic stall regime can be identified in Figure 2.3, as stated by [20]. Stage 1 occurs at angles of attack lower than the static stall angle. The behavior of the flow under these conditions is consistent with potential flow theory, and the flow stays attached to the surface. Stage 2 appears when the static stall angle is reached. Under normal conditions this would imply the separation of the flow, but if the airfoil is pitching, and therefore undergoing an unsteady motion, the flow remains attached. A leading edge vortex starts developing, typically after the suction peak [41], due to the propagation of the flow reversal originating at the trailing edge of the airfoil. Stage 3 reflects a sudden drop in moment coefficient, associated with the convection downstream of the leading edge vortex. As it can be seen in the lift coefficient curve, the lift coefficient keeps increasing during this stage, due to the influence of the leading edge vortex on the pressure distribution on the surface of the airfoil. When the vortex has fully convected downstream, a huge dropoff in lift is observed, marking stage 4. Under these conditions the flow is fully separated. Stage 5 is the reattachment of the flow to the surface of the airfoil. This phenomena begins near the static stall angle [1], but is not fully completed until a smaller angle of attack.

Although the general characteristics of dynamic stall have been described, it is still a highly complex flow phenomenon dependent on many variables. Leknys [38] studied the dynamic stall occurrence on a NACA 0012 and a NACA 0021 airfoil undergoing the same motion. PIV measurements were carried out in the airfoils rotating from 0 to 90 degrees at a constant rate (except for the first and last 5 degrees, which were the limits for the acceleration and deceleration of the system). It was found that the appearance of the leading edge vortex characteristic of the presence of dynamic stall occurred earlier for the thinner airfoil, while the growing rate of the bubble once it is formed is larger for the thicker one. Larger pitching up rates also were shown to delay the onset of dynamic stall, occurring at larger angles of attack. A similar conclusion was reached by Leishman [37]. Studying the dynamic stall formation on a NACA 23012 airfoil undergoing oscillatory motion, he found that increasing the reduced frequency of the oscillations (and therefore the pitching up motion) influenced the onset of dynamic stall. For an oscillation with an amplitude of 10 degrees around a mean angle of 10 degrees, it is shown that

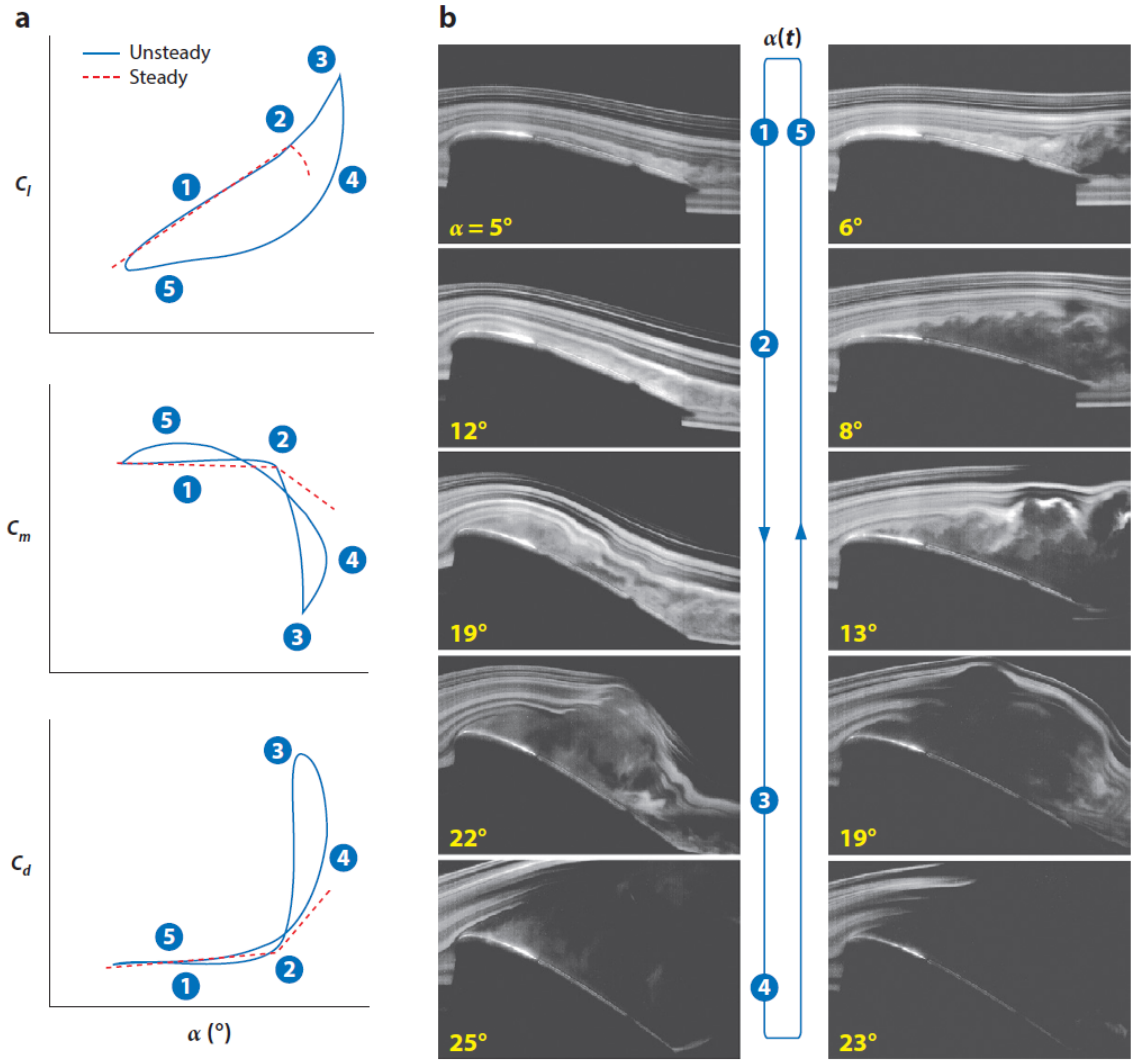

Figure 2.3: Evolution of the lift coefficient, moment coefficient and drag coefficient during a dynamic stall cycle (a), and flow visualization of the dynamic stall cycle, extracted from [20]

increasing the reduced frequency from 0.1 to 0.2 reduces greatly the hysteresis loop both in the lift and moment coefficient. This is due to the delayed onset of dynamic stall. A similar study for a pitching airfoil is done in [41], but the hysteresis loops are enlarged for larger reduced frequencies. It should be noted however that the mean angle of oscillations is larger, and this could be the reason for the enlarged hysteresis loops. The nose-down pitching moment associated with the appearance of the LEV is actually delayed for increased reduced frequency, which is consistent with the hypothesis that higher reduced frequencies delay the onset of dynamic stall.

Concerning the onset of dynamic stall, Sheng [50] developed a stall onset criterion for low-speed dynamic stall. Based on experimental data available regarding the appearance of dynamic stall for ramp-up motions for different airfoils, a linear relationship was found between the angle of appearance of the onset of dynamic stall and the velocity of the ramp-up motion, after the reduced pitch rate of the ramp-up motion ($r = \dot{\alpha}c/2V$) is larger than 0.1. The criterion for the onset of dynamic stall was developed based on this relationship, and successfully applied to ramp-up motions and oscillatory motions that result in deep stall [51]. Mulleners and Raffel [44] revisited this criterion, and found no linear relationship between the reduced pitch rate and the onset of dynamic stall for oscillatory motions of an airfoil. Instead, they found that the time elapsed from the point at which the static stall angle is surpassed and the onset of dynamic stall is reduced for increased unsteadiness. In this sense, stall

onset is actually promoted with increased unsteadiness. It should be noted that this does not necessarily contradict the conclusions reached in previous studies [37, 38, 41, 50, 51]. On those studies the delayed onset was described with respect to the angle of attack at which the detachment of the LEV detaches, not the time elapsed since surpassing the static stall angle.

For the most part, the appearance of dynamic stall is unwanted due to the high level of unsteadiness introduced in the loads and the associated fatigue that comes with it (although it is a mechanism used by insects in their flight patterns [21], and is even being introduced into micro-air vehicles to increase their lifting capabilities [22]). Many studies have been done regarding the use of aerodynamic control devices in order to either eliminate its appearance completely, or reduce the unwanted behaviours associated with it. Heine [28] studied the influence of passive disturbance generators present on the leading edge of an oscillating airfoil susceptible to dynamic stall. Even though they were not able to affect the formation of the leading edge vortex and hence the appearance of dynamic stall, an increase in lift and decrease in negative pitching moment were found during the downstroke of the airfoil, reducing thus the negative effects of the dynamic stall.

Gerontakos and Lee [35] employed trailing edge flaps for dynamic stall control. The flap was deflected downwards and upwards in a pulse motion, and different actuation times, and amplitudes were considered. Tests were performed in an oscillating NACA 0015 airfoil. It was found that only upward deflections of the flap are capable of reducing the nose-down moment associated with the appearance of dynamic stall. No mechanism was able to alter the formation of the LEV. This was to be expected, since dynamic stall is a leading edge phenomena, driven by the presence of the LEV, and therefore the use of trailing edge devices is not expected to impede its formation, but rather diminish the big excursions in lift and moment. This aspect has to be kept in mind, since, as it will be developed during the coming sections, the experimental study to be done will use trailing edge flaps as the actuation device.

Dynamic stall is thus a really complex phenomenon, with many non-linearities. Although it is sometimes beneficial in terms of its lift enhancing capabilities, most of the times it is an unwanted phenomenom and wants to be avoided. Besides the big excursions in lift and moment that have already been described in this section, the non-linearities of this flow may introduce aeroelastic instabilities. A description of these aeroelastic instabilities, as well as a tool to measure them will be given in the following section.

2.1.3. Aeroelastic Instabilities

Aeroelasticity is the study of interactions between the inertial, structural and aerodynamic forces appearing on an elastic body [61]. These interactions can lead to unwanted behaviour of the body, which may compromise its structural integrity. One of these unwanted behaviours, closely related to unsteady aerodynamics, is flutter.

Flutter [61] is a dynamic instability that occurs due to the transfer of energy from the flow to the structure during an oscillation, which will cause its oscillations to grow progressively until structure failure occurs. Classical flutter, dealing with attached flow, requires the interaction between two or more degrees of freedom. In this type of flutter, which typically occurs when the bending and torsion modes are coupled, the combination of the aerodynamic forces being generated by this motion and the motion of the structure cause it to extract energy from the flow during each cycle.

Classical flutter can only occur with two or more degrees of freedom of the structure. However, there are other types of flutter that may appear with a single degree of freedom. This is the case of stall flutter. Stall flutter is a type of aeroelastic instability generated by the non-linear aerodynamics characteristic of stalled flow. In this sense, the structure may be able to extract energy from the flow to excite the oscillations without the need of coupling of two degrees of freedom.

For a pitching airfoil, the susceptibility to stall flutter can be quantified by measuring the work done on it through an oscillation cycle. In this way, energy is going to be introduced on the structure if the moment and the motion are in phase. If the moment and motion are opposing in phase, then the flow

is absorbing energy from the structure, which will damp the oscillations and prevent instabilities.

$$W = \oint M d\alpha \tag{2.4}$$

As studied by [16], this work done on the airfoil over a cycle can be converted into an aerodynamic damping, which is going to be a measure of the susceptibility of the airfoil to stall flutter. The aerodynamic damping is expressed as:

$$\Xi_{cycle} = -\frac{1}{\pi \alpha_{amp}} \oint C_m d\alpha \tag{2.5}$$

The aerodynamic damping for an airfoil undergoing oscillatory motion under attached conditions was also derived by [16], based on the expression for the moment around the quarter chord of a flat plate given by Theodorsen [56], considering also that the pitching axis is present at the quarter-chord point. The phase lag induced by the unsteadiness of the flow helps introduce a damping in the system, as is seen in the proportionality between the damping coefficient and the reduced frequency k.

$$\Xi_{cycle} = \frac{\pi k}{2} \tag{2.6}$$

However, this expression is not valid for an airfoil undergoing an oscillatory motion at higher angles of attack, since it is susceptible to the appearance of dynamic stall. Corke and Thomas [20] studied the aerodynamic damping on both a light and a deep dynamic stall regime, and observed that light dynamic stall is more prone to the appearance of instabilities. This can be seen in figure 2.4, where the counterclockwise loops in the moment coefficient curve can be thought of as a positive contribution to the aerodynamic damping, while the clockwise loops have a negative effect.

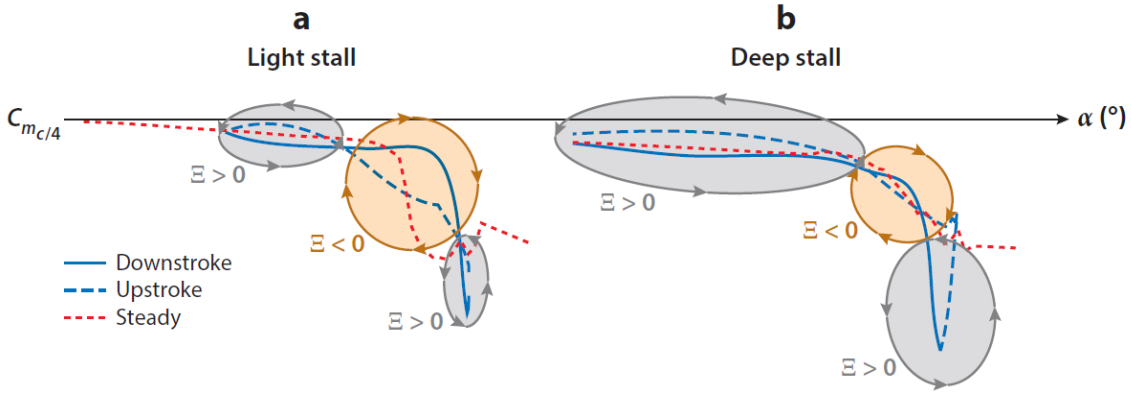

Figure 2.4: Evolution of the moment coefficient around an oscillating airfoil undergoing light (a) and deep (b) dynamic stall conditions, and its contribution to the aerodynamic damping, extracted from [20]. Clockwise loops in the moment contribute negatively to the damping, while positive contributions are found for counter-clockwise loops

In any of these cases, however, it is seen that the appearance of dynamic stall generates a clockwise loop in the moment coefficient curve, which is indicative of a part of the motion in which the structure is extracting energy from the flow. The experiment to be carried out during this thesis deals with an airfoil undergoing oscillatory motions both in the attached and stalled regime, and it is supposed to be representative of a Smart Rotor. During the oscillations where the flow is still attached, simple potential flow theory such as Theodorsen may be used in order to extract some conclusions regarding the unsteady behaviour of the system, and validate the results obtained. During dynamic stall conditions, this approach is no longer valid, and as such the aerodynamic damping will be used to assess susceptibility of the system to aeroelastic instabilities.

2.2. The Smart Rotor

The experiments to be performed during this thesis deal with a new concept in wind turbines research: the Smart Rotor. This concept was introduced in chapter 1, and deals with the reduction of the unsteady loads on a wind turbine blade by modifying the shape of the blade.

The Smart Rotor concept for wind turbines is an evolution of well established research done for rotorcrafts. Several studies have been carried out in this area, regarding the use of aerodynamic control surfaces to reduce vibrations on the rotor blades. Barlas and van Kuik [5] reviewed different actuation mechanisms used for this purpose. The main requirements for the actuation mechanisms are an appropriate bandwidth, capable of compensating the varying loads, and a good frequency response. These mechanisms must also add little weight to the whole system and be simple to implement and use.

Trailing edge flaps appear as the most promising concept. These mechanisms work by changing the effective camber of the airfoil, thereby altering the pressure distribution over it and the aerodynamic loads. Due to its relatively low inertia (not the whole airfoil has to be moved, but just the rear part), the frequency response is also appropriate. Within this concept, two different implementations arise: rigid trailing edge flaps and deformable trailing edges. Rigid trailing edge flaps are deployed around a fixed hinge point, introducing thus a discontinuity in the geometry of the airfoil. Deformable trailing edges modify the camber of the airfoil, but do so in a continuous way.

Other concepts, although promising, have some disadvantages that make them not as suitable for this kind of application. This is the case of microtabs, which are basically deployement tabs similar to a gurney flap, but placed along the chord of the airfoil. These tabs modify the pressure distribution of the airfoil by changing its effective camber. The lift altering capabilities are really promising [8, 19, 58], with values comparable to those of trailing edge flaps. Johnson et al [30] focused on microtabs in their review of the possible mechanisms available for active load control in wind turbines. The frequency response (higher than for trailing edge flaps) and lift altering capabilities are some of the inherent benefits of these devices. However, it has to be noted that the chosen active control device should be able to compensate for the whole range of loads up until its maximum load altering capabilities. More research is needed in this aspect, since the deployment of the tab implies a fixed change in load.

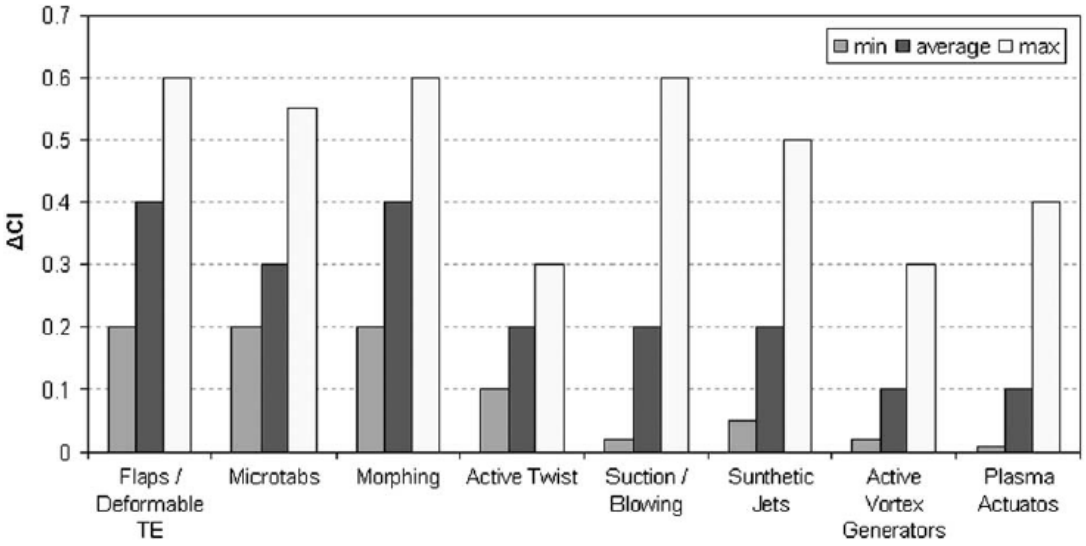

Figure 2.5: Lift control capacity of several aerodynamic control concepts, extracted from literature [5]

Trailing edge flaps and microtabs have been the main focus of research for active load control in wind turbines, although some other mechanisms have also been studied. Figure 2.5 shows the bandwidth of several mechanisms regarding their lift compensation capabilities, which highlights the benefits

of the trailing edge flap due to its increased bandwidth with respect to other aerodynamic devices. While other mechanisms have been used in the Smart Rotor research [8], the majority of research being done nowadays is focused on rigid or deformable trailing edge flaps. The following sections will deal purely with Smart Rotor research done with trailing edge flaps as the actuation device.

Three main components can be identified in a Smart Rotor: the actuator, the controller and the sensing system. While a consensus has been reached regarding the preferred actuation mechanism, the choice of controller and sensing system is more complex and several solutions have been proposed. The different options proposed in literature for the controller and the sensing system will be reviewed in sections 2.2.1 and 2.2.2 respectively. During this literature review two components of special interest in the Smart Rotor research have been identified: the time lag and the performance under dynamic stall conditions. These will be reviewed in sections 2.2.3 and 2.2.4. Since almost every study involves two or more of these aspects, some studies will be reviewed more than once, placing special focus on the section specific aspects. The general aspects of each study will be introduced in the controller section 2.2.1.

2.2.1. Control architecture and Load Reduction capabilities

In this section, a review of the control architecture applicable to a Smart Rotor is carried out. Since a PID controller is used in this thesis, a more detailed description of this type of controller will be given. After this, the different options present in Smart Rotor literature regarding the control architecture will be shown, as well as a general description of each study and the general conclusions drawn from each one of them. Finally, a brief discussion is conducted regarding the choice of control architecture.

A controller is a device used in any process in which a variable needs to be given a desired value. This is done by comparing the value of the Process Variable (PV) and the desired signal, known from now on as Set Point (SP). The difference between these two is the error signal, and is used by the control architecture to apply a correction to the process so that the PV reaches the SP. There are many ways of doing this, ranging from simple PID controllers to more complex devices.

A PID controller is one of the more widely used control architectures in industrial applications [32]. An error signal is generated, by determining the difference between the PV and the SP. The actuation signal generated by the controller is the sum of three different components acting on the error signal: Proportionate (P), Integral (I) and Derivative (D). A block diagram of a PID controller can be seen in figure 2.6. An error signal is generated ($e(t)$), and the three different components act on different variants of the error signal. The result is an actuation signal ($F(s)$), which is input in the process. If the system is well designed, this is going to bring the Process Variable ($X(s)$) closer to the Set Point (u).

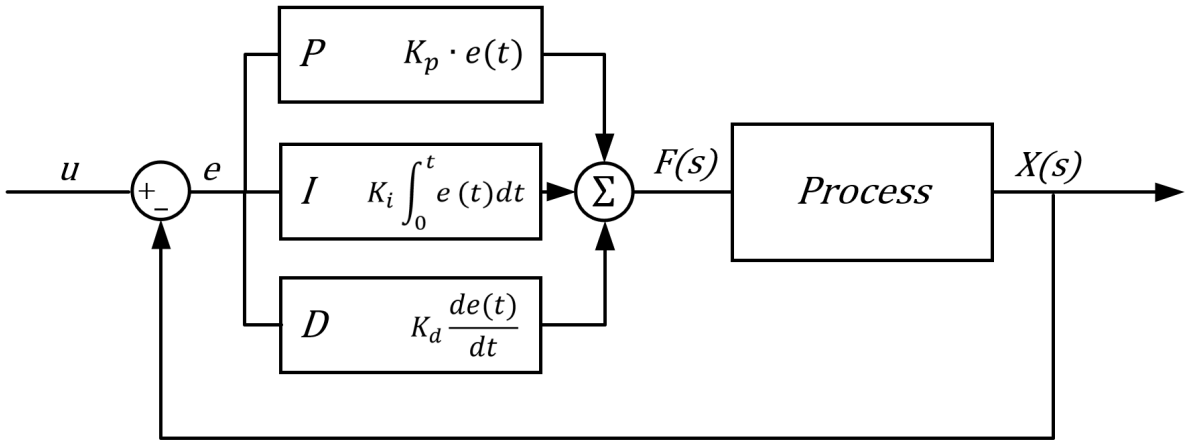

Figure 2.6: Block diagram representative of a typical PID controller

As it can be seen, each component of the PID controller acts on a different variant of the error signal:

- The proportionate component of the controller acts directly on the error signal: the larger the error signal, the larger the actuation signal is going to be, to try to compensate for this error. The proportional gain K_p, determines how fast the system reacts to the error. Large proportional gains can generate stability problems, since they introduce actuation signals that are too large for the error they are trying to compensate.

  Proportionate controllers are common in industry, but they are not catered for every application. These type of controllers are susceptible to steady-state errors: a point can be reached in which the actuation signal generated for a certain error does not have an effect anymore in reducing it. Under these circumstances, larger proportional gains can further reduce the steady state error, but never remove it completely.

- The integral components acts, as its name suggests, on the integral of the error signal. This component stems from the inability of a proportionate controller to eliminate steady state errors. Since the integral term is proportional to the integral of the error signal, a steady state error will start building up the integral term, thus not stopping until the error has been eliminated. The integral term contributes to the presence of oscillations in the system, and eventually to its instability.

- The derivative components acts on the derivative of the error signal with respect to time. In a sense, it acts as a predictor, trying to look into the future to damp the response of the system. If the error is being reduced, its derivative is going to be negative, and hence the derivative term is going to act against the proportionate and integral terms, trying to reduce the oscillations introduced by the previous two components.

PID controllers have been widely used in the field of Smart Rotors. Buhl [13] implemented a P controller based on the measured angle of attack, and a PD controller based on position, velocity and acceleration of an airfoil section in an aeroservoelastic code. No finite wing effects were considered. Two different test cases were considered: a step in the wind velocity from 10 to 12 m/s, and a representative turbulent field. A parametric study was carried out in order to obtain the optimal gains for the controller. Reductions of up to 95% in the standard deviation of the normal force were obtained for the first case, and up to 81% for the second one. Basualdo also studied a 2-dimensional airfoil in an aeroservoelastic code using potential theory to describe the aerodynamics and a spring and damper model to simulate the deformations. Three different turbulent flow simulations (2,20 and 100 seconds) were studied to determine the load reduction capabilities of a PD controller based on the vertical displacement, velocity and acceleration, and the controller gains were set using the Ziegler-Nichols rules for a first approximation, followed by manual tuning to obtained optimal performance . This performance was measured by the reduction in the standard deviation of the displacements. A reduction of 75% was obtained for the 2 seconds turbulent field, similar to the results obtained by Buhl. The standard deviation was increased however, for the 100 seconds case. This was attributed to the inadequacy of this parameter to ascertain load reduction capabilities, since it was observed that the displacement oscillations were smoothed out.

Both of these studies are done on a 2 dimensional airfoil, although the same control mechanism has also been used in models of a complete wind turbine. The control mechanism becomes more complex once the whole system is considered, since the rotation of the wind turbine makes it a LTV (Linear Time Variant) system. This can be somewhat fixed by applying a Multi-Blade coordinate transformation (MBC). The analysis of a wind turbine is difficult, since it includes rotating reference frames (the blades of the rotor), and a fixed reference frame (the tower-nacelle system). The idea behind a MBC is to transform every degree of freedom into a non-rotating reference frame. This was done by Bir [11] for a three-blade wind turbine with variable rotor speed. The end result is the removal of the periodic terms that are not integer multiples of the 3P (3 times per revolution) terms in the fixed reference frame. A modal analysis was also carried out by Bir, to obtain the modal dampings for the different displacement modes present in the wind turbine, after averaging the system dynamics matrix. This is done before and after performing the MBC, and different damping predictions are obtained, since all periodic terms that affect the system dynamics are averaged out when MBC is not performed. A similar modal analysis is performed by Stol et al [55], comparing the results to the ones obtained by using a Floquet modal analysis, that does not average out any time-variant contribution to the system dynamics. The

differences between the Floquet and the eigenvalue analysis after MBC for a normal and an extreme wind turbine operation regime are negligible. This suggests that simpler LTI control techniques such as PID controllers can be used for 3-dimensional wind turbines after applying a MBC.

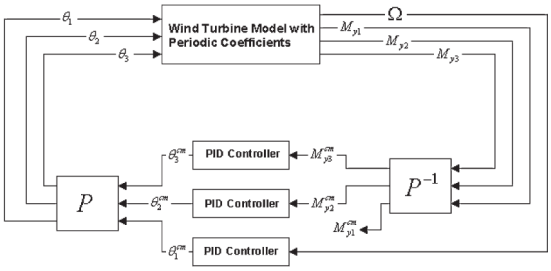

(a) Control Diagram of the Smart Rotor controller, using the Coleman transformation to actuate on the fixed-reference frame loading

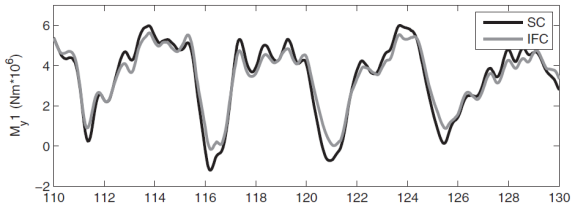

(b) Time extract of the load reduction capabilities of the Smart Rotor (IFC), compared to the Standard Case (SC)

Figure 2.7: Control diagram and load reduction of the Smart Rotor proposed by [33]

This is the approach taken by Lackner and van Kuik [33]. A PID controller is designed, with the intention of reducing the yaw and tilting moments, which are the degrees of freedom obtained after transforming the bending moment of each individual blade in its rotating reference frame to a non-rotating one. The outputs of the controller are thus the flap angles in the fixed reference frame, so the inverse operation is done to transform them into the blades reference frames. The block diagram of the controller is shown in figure 2.7a. The gains are manually tuned as to prevent saturation of the flaps while maintaining a substantial load reduction. The simulations are done in the NREL 5MW wind turbine, on the aeroelastic package GH Bladed. Rigid trailing edge flaps spanning 20% of the blade's length and with 10% chord are used, and their effectiveness measured in reduction of the damage equivalent flapwise bending moment. Two load cases are considered: a Normal Turbulence Model (NTM) and an Extreme Turbulence Model (ETM). These cases are supposed to be representative to the operation conditions experienced by wind turbines, as defined by the International Electrotechnical Commission (IEC). The reductions obtained range between 10-15% for the majority of cases considered, as shown in figure 2.7b. However, the authors note that a more aggresive control, as well as larger actuation surfaces will undoubtedly result in an improvement of the load reduction capabilities. In a later study, Lackner and van Kuik [34], study the performance of the same Smart Rotor for a global step change in wind velocity. The controller was found to be incapable of reducing the changing loads for this case. This can be explained since the global change is experienced by the whole rotor, so the yaw and tilting moments are not changed, but rather the average root bending moment of the three blades (the other degree of freedom in the fixed-reference frame, not used in the control loop). This method of control is thus proven not to be effective under all situations for the reduction of the loads oscillations.

A similar approach is taken by Bernhammer et al [10]. The yaw and tilt bending moments in the fixed reference frame are the inputs of the controller, after a MBC has been performed. A PI controller is used in this case, and the parameter tuning is done in order to keep the flap deflections under 5°, while trying to reduce the resonance around the first flapwise bending frequency. Both fatigue and extreme load cases are studied. The proposed Smart Rotor is found to be able to reduce the fatigue loads, as expressed in the reduction of the blade root bending moment, in 24%. This reduction drops to 8% for extreme cases. One of the main contributions of this study is the analysis of the influence of the Smart Rotor in the different parts of the wind turbine. It is found that most of the loads are reduced, except for the torsional moment of the blades, which is increased. This is attributed to the flap actuation, since it will modify the pressure field around the section and create a pitching moment.

Andersen [3] also studied the Smart Rotor concept in a 3-dimensional wind turbine. However, rather than reducing the moments on a fixed-reference frame, the choice is to reduce the oscillations on the root moment of each blade. Even though the reduction in the fixed-reference frame is not going to be

the same quantitatively, they are correlated and so a reduction in one implies a reduction in the other one. A PD controller is implemented based on the deformation of the section of the blade where the deformable trailing edge flap is installed. Simulations are carried out with an aeroelastic code on a 33 meter Vestas V66 wind turbine blade. The optimal gains are computed in an iterative way, by defining a loop until the equivalent flapwise blade root moment is minimized. A reduction of 60% is obtained for the largest flap studied, 11 meters. Besides the PD controller, a P controller is also tested, and the maximum reductions (for the same 11 meter flap) are of 27%. No other explanation apart from the simplicity of the controller is given as to why there is such a big discrepancy in these numbers.

In another study, Andersen [2] employed a P controller with a high-pass filter. The characteristics of this study are different from the previous one: A NREL 5 MW reference turbine is studied, with 63 meter long blades, and a flap of fixed length is used for actuation purposes. The length of this flap is 10% of the blade's length, or 6.3 meters. The flap deflection (β) is given by the following expression:

$$\beta = K_p \left[\epsilon(r_s) - z\right] \tag{2.7}$$

$$\tau \frac{\partial \epsilon'}{\partial t} + \epsilon' = \epsilon(r_s) \tag{2.8}$$

where ϵ is the blade root bending moment and τ is the time constant of the high-pass filter. A gradient based optimization is used in order to find the optimal values for the variables that reduce the equivalent blade root moment fatigue load. The variables to be optimized are the proportional gain (K_p), the time constant of the high-pass filter (τ), the radial position of the flap (r_f) and the radial position of the sensor (r_s). The optimization gives a maximum reduction of the loads of around 25%, as it can be seen in figure 2.8. This number has to be seen in the context of a small actuation surface (only 10% of the blade's length), and a purely proportionate controller, which as shown also by Andersen [3], results in a worse performance than a PD controller (under this type of implementation).

Setting the gains of the PID controller is not a straightforward task, as it can be seen by the variety of solutions proposed. A more complex approach is to perform system identification in the system to obtain its frequency response, and derive the optimal gains from it. This is done by Chen et al [18], in order to tune the gains for a PI controller based on the yaw and tilting moments obtained after a MBC is applied to the rotating-frame bending moments. The HAWC2 aeroelastic code is used to perform the simulations, and upscaled wind turbines obtained from the NREL 5 MW reference turbine are studied. As it was mentioned, system identification was performed on the wind turbine blade with a flap, and its results used to tune a PI controller based on the minimization of a cost function, in an optimization process given by [39]. The flap is actuated in order to reduce the 2P loads, while the whole blade is pitched to reduce the 1P loads. This may help to explain the small contribution to the load reduction capabilities of the system, with 17-20% reduction in the out-of-plane damage equivalent loads when only pitch control is used, improving to 20-22% when also the flaps are actuated.

Experimentally, a similar approach was taken by van Wingerden [60]. A proof of concept of the load reduction capabilities of a Smart Rotor blade was carried out. A high aspect-ratio wing (0.9 meter length and 0.12 meter chord) is tested in a low turbulence wind tunnel at Delft University of Technology. The wing is pitched as to represent the load oscillations. Subspace identification is performed by applying a white noise signal to the trailing edge flap, and a bode plot is derived from it. With this bode plot, loop shaping is used in order to determine the gains of a PD controller with notch filter. Several load cases are investigated: a periodic disturbance on the 3P frequency, a step disturbance, and a representative noise signal with peaks in the 1P and 3P frequency. A load reduction of around 90% is reached for the periodic disturbance on the 3P frequency. No quantitative analysis of the second case is done, although a clear reduction in the amplitude of the loads is observed. Lastly, the load reduction capabilities for the representative noise signal are of 37% for the 1P frequency and 55% for the 3P frequency. The actuation bandwidth of the trailing edge flap is able to compensate for pitch angle variations up to 2°. The disturbance signals are kept below this level, and this may explain the high values of the load reduction capabilities compared to other studies.

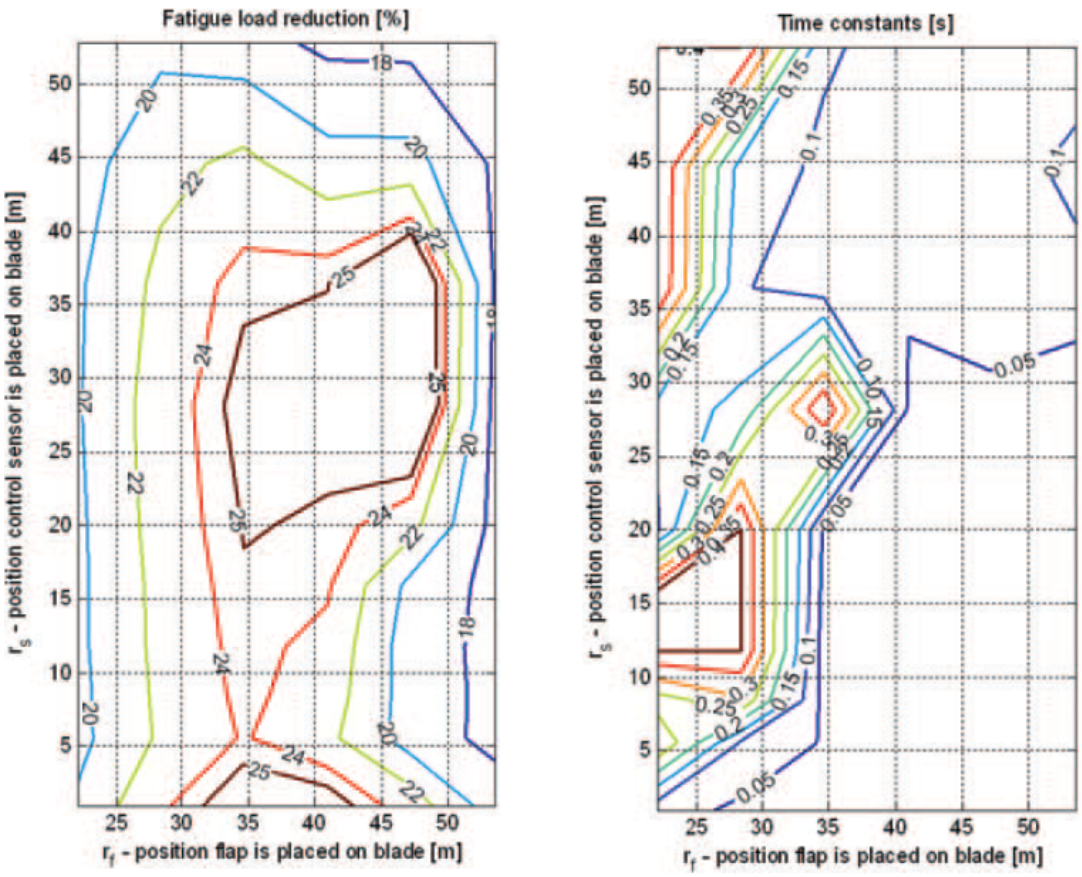

(a) Fatigue load reduction as a function of flap and sensor position on the blade

(b) Optimized time constant as a function of the flap and sensor position on the blade

Figure 2.8: Results of the gradient based optimization used in the Smart Rotor study performed by Andersen [2]

In a subsequent study, van Wingerden[59] introduced a new type of control for a Smart Rotor turbine. In this study, a scaled-down version of a two-bladed Smart Rotor, seen in figure 2.9a, is studied in the Open Jet Facility (OJF) of the Delft University of Technology, a closed circuit wind tunnel with a 2.85 x 2.85m test section. System identification is again done on this experimental setup, in order to identify the dynamics of the system. Special emphasis is placed in not including the periodic components appearing due to the rotation of the turbine in this system identification. With this, a Bode plot is derived, and this is taken as the basis for tuning the controller. Since some coupling between the two blades is found, a H_∞ controller is designed, which is a Multiple-Input Multiple-Output controller (MIMO). On top of this, a feed-forward controller is included into the control architecture, since some of the oscillating loads are expected to be deterministic and multiples of the 1P frequencies. This combination of controls is used for reducing the loads experienced due to stochastic perturbations in the wind (turbulence), in combination with periodic disturbances. A great reduction of around 90% is observed in the loads on both turbine blades, as it can be seen in figure 2.9a. This is again a much higher value than the one presented by other Smart Rotor concepts, and also larger than the one obtained when no feed-forward controller is employed.

A Model Predictive Control (MPC) is used by Castaigne [17]. This study is especially important since it is performed experimentally on a full-scale Vestas V27 wind turbine in the field. One of its three blades is equipped with a trailing edge flap spanning 70 cm, or around a 5% of the blade span. System identification is again performed for the tuning of the controller, which in this case is an MPC. This type of controller is a more advanced form of control, in which a prediction of the future response of the system is done, according to a dynamic model of it, and an optimization is carried out in order

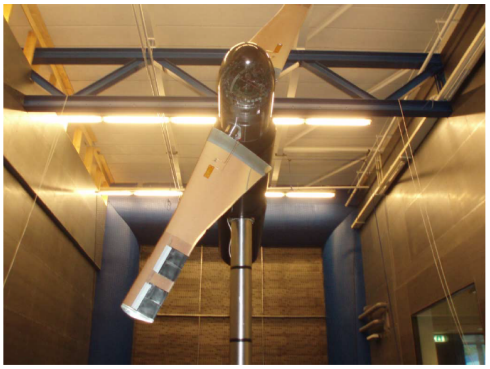

(a) Two-bladed wind turbine model used in the experiments by van Wingerden [59], with two trailing edge flaps to give it Smart Rotor capabilities

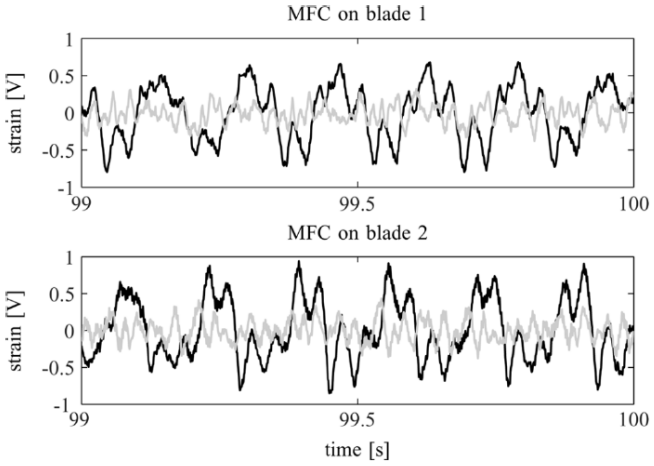

(b) Loads experienced by the two blades, without actuation of the trailing edge flap (black), and with feedforward+feedback control (grey)

Figure 2.9: Setup and load reduction capabilities of the study done by van Wingerden [59]

to reduce the error of a cost function over the prediction of the future response. Emphasis is placed in reducing the 1P and 2P frequencies, and limiting the actuation at higher frequencies (in order to reduce the wear of the actuators). This Smart Rotor is tested for 9 alternating sequences of active control followed by no control, of 2 minutes each, in order to assess its load reduction capabilities. This is done due to the stochastic nature of the wind, and the inability to study the same wind under two different sets of conditions. The results are evaluated according to the reduction in the equivalent loads due to the flapwise blade root bending moment. An average load reduction of 14 % is achieved, with a 20% reduction of the 1P loads. These values are promising, especially considering the small actuation surface of the trailing edge flaps, with higher values of reduction expected for larger actuation surfaces, as it has already been discussed.

Also an MPC controller had been used by [6], although numerically instead of experimentally. Three trailing edge flaps have been placed in each blade of NREL 5 MW turbine, spanning 11.6 meters (18% of the blade's length), and the simulations have been carried out in the aeroservoelastic code DU_SWAMP. As is standard, system identification is performed, and the results obtained with it are used to tune the different parameters of a MPC controller. The controller is tested under different load cases, according to the IEC turbulence intensity levels. Load reduction is expressed in the change in damage equivalent loads (DEL). These reductions range from 10.9% to 27.3%, with the higher reduction being obtained in the lower turbulence case. It should be noted that the high turublence intensity levels generate loads on the blades too large for the flaps to compensate. This places again the focus on the need of large enough actuation surfaces, capable of compensating the variable loads.

Other forms of control have also been used. A Linear Quadratic Regulator (LQR) was used by Bergami and Poulsen [9] in their numerical study of the NREL 5 MW turbine performed on HAWC2. Trailing edge flaps are placed on the 61.5 meter long blade, spanning a 20% of its total length. System identification is performed to obtain the frequency response of the system, placing special attention into not including the periodic disturbances into the identification process. The identified model is used to tune a LQR regulator, in which a cost function is minimized. This cost function is dependent on the variation of the blade root flapwise bending moment and the flap angle. In this way, the loads are reduced while also keeping the actuation signal within considerable limits. The controller capabilities are tested against a turbulent wind field following IEC standards for a class B turbine, and three configurations are tested: $d00$, acting purely as a feedback controller; $dSin - cos$, which introduces a Sine-Cosine signal as a way to anticipate periodic disturbances, and $dWsp$, where the periodic component is anticipated by means of a simplified model of the wind speed variations (including aspects such as the tower shadow). The results are expressed in percentage reduction of the DEL. A 10% reduction is achieved

by the $d00$, while for the $dSin-cos$ and $dWsp$ cases, reductions of 13.8% and 14.5% respectively are obtained. Similarly to the results obtained by van Wingerden [59], including the deterministic loads into the control scheme improves its performance.

The idea of including the deterministic loads into the control scheme has been explored further in many other studies. Lifted repetitive control techniques [29] or Iterative Learning Control laws (ILC) [46, 57] include these deterministic loads typically present during normal wind turbine operation, and focus on their reduction. These innovative schemes have been proven able to reduce the periodic components of the unsteady loads, although the application of these techniques in the Smart Rotor research area is still in its first steps, especially compared to other more standard control techniques.

Several aspects can be extracted from this part of the literature review. First of all, the comparison between different studies is not a trivial task. A Smart Rotor study can be approached in many different ways: different wind turbines are studied, subject to different wind fields, with different forms of control as well as different sensing systems.

One of these aspects is the actuation surface of the trailing edge flaps: it has been shown that the load reduction capabilities of a Smart Rotor are heavily influenced by this parameter, as can be deduced by the high values given by van Wingerden [59, 60], where the loads oscillations are kept within the limits of the actuation surfaces. It can also be concluded that including the deterministic loads into the control architecture may lead to improved performance in terms of the load reduction capabilities of the Smart Rotor.

However, due to these discrepancies between the different Smart Rotor studies, no controller can be deemed superior in terms of performance. In any case, the improvements arising from a more complex form of control are not expected to be that large, and so from practical considerations a simpler form of PID controller will be studied, since an optimal control is not the purpose of the present thesis. In particular a proportionate controller with the velocity of the flap as the output will be considered. Acting on the velocity rather than on the position of the flap is expected to help eliminate the susceptibility of this type of control to a steady-state error, since any error will result in a movement of the flap, and a change of circulation. This eliminates the need for an integral term, as it will only generate instabilities in the system.

2.2.2. Sensing System

For a Smart Rotor, the sensing system is in charge of detecting the parameter for which the system is trying to reduce the oscillations. The choice of sensing system is therefore evidently going to influence the performance of the Smart Rotor as a whole. A choice of sensing system has to be made according to a compromise, between complexity and performance of the sensing system. Some systems may have small time delays but give us a limited description of the flow, while others may be really intrusive and introduce unwanted time delays in the control loop. Several approaches can thus be used.

One of this approaches is to measure the bending moment on the whole blade. This can be done by the use of strain gauges, for example. A strain gauge is simply a sensor made of conductive material, that is placed on the surface to be measured, and as its name suggests, measures the strain placed on it. The strain placed on the object, and thus on the sensor, effectively shortens or lengthens the conductive material, reducing or increasing its resistance respectively. This change in resistance is measured, and converted into displacement. Since the presence of a bending moment on a blade would cause one of the sides to experience tension and the other compression, strain gauges can be placed so that the bending moment can be derived from their outputs. Experimentally, a type of strain sensor known as macro fiber composite patch was used by van Wingerden [59, 60] to measure the strain in the root and use this value as the parameter for which the oscillations need to be reduced in the feedback loop. A similar approach was used in the experiments performed by Castaigne [17]. Several more numerical studies have used the blade root moment [2, 9, 10, 18, 33, 34] in their Smart Rotor studies. However, it has to be noted that while the reduction of the blade root moment is of importance, it is a structural response to the change in the aerodynamic loads experienced by the different sections of the blade. As such, there is going to be a time delay between loads and deformation of the blade.

This has to be kept in mind, since time delays influence greatly the performance of a Smart Rotor, as it will be shown in the next section.

Also on the structural side, measurements of position, velocity and acceleration of a section of the wing have been proposed as the property of interest for a Smart Rotor control loop. Measuring the position is analogous to measuring the bending moment, since they are both related to the structural deformations of the blades, and it can also be done by using strain gauges. Measuring the acceleration is more favourable in terms of the aforementioned lag between the aerodynamic loads and the structural response. This approach is used in several 2D and 3D numerical studies [3, 6, 7, 13]. Effectively, the use of position, velocity and acceleration in a control loop is equivalent to the presence of a proportional term as shown in the description of the components of a PID controller (position), and two derivative terms (velocity and acceleration).

An alternative to measuring the structural response is to measure the angle of attack of a section of the blade. The benefits of measuring the angle of attack are obvious, since it gives a direct description of the flow, rather than an effect of it in the case of the bending moment. However, measuring the effective angle of attack on a blade section is a rather more complex task than placing a sensor on its surface. One of the ways of doing this is by placing for example a 5-hole pitot tube, capable of measuring the magnitude and direction of the flow. This has been proposed by Buhl et al [13] in a numerical study. This is, however, a more intrusive technique, as it involves placing a sensor in the flow itself. No experimental research has been done with such a setup.

The aerodynamic loads can also be estimated by using pressure taps distributed along a section of the blade. The values given by the pressure transducers can be integrated and the aerodynamic loads computed. This measurement technique is less intrusive and a direct description of the loads can be obtained. This is suggested by Nowicka [46] by using ILC techniques. However, the complexity of such a setup is higher than placing strain gauges at the root of the blade to measure the bending moment. Several pressure transducers have to be used in order to integrate the load instead of just one strain gauge, and they have to be placed either inside the model, making the setup more complex, or outside, which would generate large tubing lengths and associated time delays.

Based on the findings presented here, it appears that there is not an optimal sensing system that is intrinsically better than the rest. Each one presents its advantages and disadvantages. Strain sensors have been the most widely used sensing system, since they are easy to implement, and the ultimate goal of a Smart Rotor is to reduce the bending moment on a blade. However, as it has been already described, a Smart Rotor reduces the loads on a blade by modifying its aerodynamics. The time delay between the aerodynamic loads and the structural response is therefore always going to be present. In order to bypass this delay, measurements of the flow itself can be taken, such as measuring the angle of attack and the flow velocity by using multi-directional pitot tubes. This gives a more direct representation of the aerodynamic loads, although it is a much more intrusive technique and it may also be unrepresentative of more complex situations such as stalled flow. This is not a problem if the aerodynamic loads are integrated by placing pressure sensors along a section (or sections) of the blade although the complexity of the setup is increased. For this experiment, however, pressure taps are chosen as the sensing system due to their capability of giving a more detailed description of the flow. This will give more flexibility and insight when assessing the performance of the proposed controller, specially during dynamic stall conditions, and hence the increased complexity is assumed. Besides this, since the experiment is performed on a rigid wing, strain gauges are not considered since they rely on the elasticity of the model to be tested.

2.2.3. Time Lag

The purpose of the Smart Rotor is to actively reduce the fatigue on the blades of a wind turbine, by reducing loads oscillations. This active form of control means that there is going to be a delay between the time at which the inputs of the control loop are measured by the sensing system, and the time at which the control surfaces are actuated. A large delay, referred to from now on as time lag, may potentially result in the uncontrollability of the system, since the control action is being applied at a

time where the loads do not correspond anymore to the loads at which the control action was derived. Several sources of time lags can be identified: the sensing system introduces a time lag based on the time it takes to do the measurements. Besides,the choice of sensing system also plays a role, as discussed in the previous section. Measuring the structural response is going to introduce a further delay into the system that will not be there if the aerodynamic loads are measured directly. The controller itself introduces a time delay (although it is expected to be rather small, especially for simple control architectures). Lastly, the actuation mechanism is the origin of yet another time lag, since it takes a finite amount of time to actuate the control surface.

Many numerical studies have been done on the concept of Smart Rotors, but only a few of them have actively studied the effect that time lag has in the load reduction capabilities. Buhl et al [13] studied the effect of different time lags for the load reduction capabilities of a trailing edge flap on a 2 dimensional airfoil. This time lag is introduced as the time taken by the sensing system to perform the measurements. Two different control strategies are considered, one of them based on the angle of attack ($A\alpha$), and another one based on deformation and velocity of deformation of the airfoil ($Ay + By$). Note that Ay is a parameter acting on the position of the airfoil, and By is a parameter acting on the velocity of deformation of the airfoil. As expected, increase in time lag results in a decrease of the effectiveness of the controller, as measured by the reduction of the standard deviation of the normal force experienced by the airfoil when subject to a turbulent wind field. This is shown in figure 2.10a, and a stronger reduction is seen for the control based on the angle of attack, although the trend for both strategies is a decrease in performance with increased time lag. The effect of velocity of actuation has also been studied, and as expected, larger velocities of actuation result in larger reduction of the oscillating loads, see figure 2.10b. The effect of actuation velocity is also studied by Basualdo [7]. The setup is similar as the one done by Buhl et al [13], studying a 2D airfoil in a aeroservoelastic code, actuated via a traling edge flap. Two different actuation speeds are considered, a fast actuation speed corresponding to 40 degrees per second, and a slow actuation speed of 10 degrees per second. The results are significantly better for the fast actuation speed.

A similar study is also done by Lackner and van Kuik [33], by performing 3-dimensional simulations in the GH Bladed aeroelastic code of a NREL 5 MW reference turbine [31]. The results obtained in this study were decomposed into a high frequency and a low frequency spectrum, and different trailing edge flap actuation velocities studied, ranging from 10 to 90 degrees per second. The low frequency region presented almost no change in the performance for different actuation velocities. Meanwhile, an actuation velocity of 10 degrees per second experienced a reduction in the load reduction capabilities in the high-frequency spectrum.

Numerical 3-dimensional studies have also been performed where the effect of time lag has been considered. This was done for the first time by Andersen [3]. A PD controller is used to obtain the desired actuation signal for a deformable trailing edge flap. Several lengths of the flap have been considered, ranging from 1 to 11 meters on a 33 meter long blade. The largest flap is the most effective in reducing the oscillations as measured by the reduction of the single equivalent load (EQ_F), obtained by using a rainflow-counting algorithm to convert a time-series bending moment into a single value. With this largest flap length, the effect of a time lag in the system is studied, as well as studying the effect of the mass of the flap. Considering the mass of the flap implies considering the inertial forces, and as such an extra delay is introduced in the system, since not only the aerodynamic forces have to be compensated by the actuation mechanism. This is seen in figure 2.11. A similar trend as the one obtained in figure 2.10a is observed, with a decrease in performance for increased time lag. Increasing the inertia forces also results in a decrease in performance.

Andersen et al [2] performed the first study of the influence of signal lag and delay on a 3-dimensional model of a wind turbine, considering again the 5MW reference turbine [31]. A trailing edge flap of 10% span and 10% chord is placed on the blade for control purposes. This is done by means of a proportionate controller with a high-pass filter, so as to only actuate on the higher-frequency oscillations. The parameters of the controller are optimized (proportional gain, positioning of the flap, time constant of the high-pass filter) following a gradient based optimization. It has to be noted that the definition of time lag is different in the present work and in the work from Andersen. In his work, the time lag is

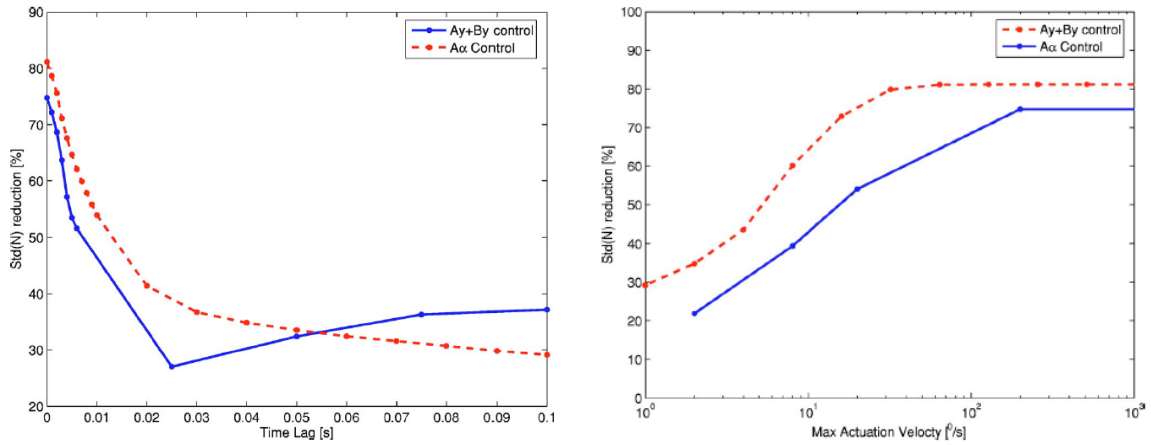

(a) Effect of time lag

(b) Effect of actuation velocity

Figure 2.10: Effect of time lag and actuation velocity in a Smart Rotor airfoil with two different control strategies, in terms of reduction of the standard deviation of the normal force acting on the airfoil, as extracted from [13]

simply a first-order filter:

$$\tau \frac{\partial \epsilon'}{\partial t} + \epsilon' = \epsilon(t) \tag{2.9}$$

where ϵ represents the strain on a position near the root of the blade, obtained by simple beam theory. ϵ' is the input to the controller. The use of this filter has the objective of introducing the lag between the aerodynamic loads and the structural response of the blade, and is controlled by the time constant τ. On the other hand, a time delay is also studied, which corresponds to the definition given in the present thesis for time lag, as the time taken in each loop between the measuring system and the output of the controller, as it follows:

$$\epsilon'(t) = \epsilon(t - \tau) \tag{2.10}$$

With this into account, the effects of time lag and time delay were studied, and their consequences on load reduction capabilities are shown in figure 2.12. Increasing the time delay results in a bigger loss of the effectiveness of the Smart Rotor than a time lag. For time delays larger than 200 ms the system becomes uncontrollable. This is not the case for a time lag, where a reduction is also seen, but it does not have such a negative effect. This stems from the fact that for this definition of time delay, the controller does not know at all what is happening in the flow, while for the time lag it gets a filtered version of what is happening.

Nowicka et al [46] studied also a time delay between the input signal to the actuation system and its actual response. An ILC controller is developed, to utilize the repetitive behavior of load oscillations. An inviscid flow model is used for the computations, including the wake shed by the airfoil. The time delay is implemented in a similar way as the time lag implemented by Andersen in equation 2.9. It was found that for the largest time lags, the oscillating loads are increased rather than reduced. Reducing the delay results in a better response, converging into almost negligible oscillations when no delay is included.

For numerical studies, a choice of including time lags or not can be made. However, during an experimental study, these time lags are inevitable, and therefore an optimal performance is never going to be obtained. Even though the time lag has proven to be a fundamental parameter in the feasibility of a Smart Rotor, there are no experimental studies where its effects are actively accounted for. The lack of these kind of experiments, as well as the influence that the time lag has been proven to have on any Smart Rotor concept, are the main reasons why the time lag will be purposefully studied in the current thesis in a wind tunnel environment. Besides the time lag present in the control system, the frequency of unsteadiness of the loads is also expected to play a role in the load reduction capabilities of such a

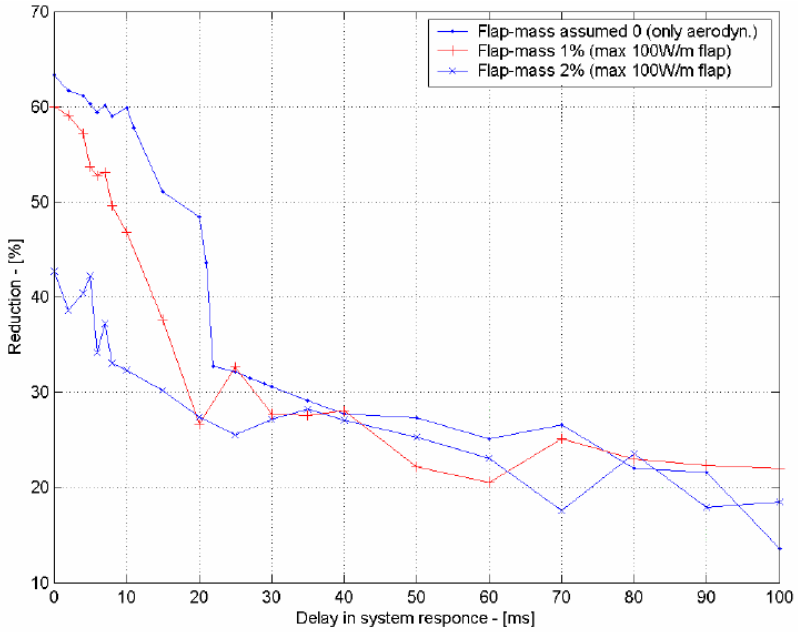

Figure 2.11: Influence of inertial forces and time delay in the load reduction capabilities of the Smart Rotor concept proposed by Andersen [3]

system. For the same time lag, larger frequencies result in faster changes of the loads, and therefore the effectiveness of the Smart Rotor is expected to decrease. Different unsteadiness frequencies will thus be tested in the experiment, and their influence assessed.

2.2.4. Dynamic Stall

As it was discussed in section 2.1.2, dynamic stall is a phenomena that can occur in oscillating airfoils at large angles of attack due to the detachment of the flow from the surface. The blades of a wind turbine are constantly experiencing changes in angles of attack, which lead to load oscillations. Some of these oscillations may occur at large angles of attack, and thus lead to the appearance of dynamic stall on the rotating blades. Shipley [52] studied the occurrence of dynamic stall on a horizontal axis wind turbine blade. The study is based on the experimental data recorded on the NREL's Combined Experiment [15]. Several different inflow conditions, as to be representative of the nominal operating environment of 10.1 meter 3-bladed turbine, are studied, and the data of pressure transducers present on one of the blades recorded. Assuming that dynamic stall occurs for values of the suction peak at least twice as large as the static counterpart, the number of cycles in which the blade is experiencing dynamic stall is obtained. Taking tower shadow into account, the inboard section (30% span) experienced the conditions above described as representative of dynamic stall over 14% of the cycles. The outer sections were less prone to the appearance of the phenomena. After removing the effect of the tower shadow, the number of cycles in which dynamic stall was present was reduced to around 2% for all sections, which may be more representative of upwind wind turbines. However, it has to be noted the conservative approach taken to establish the appearance of dynamic stall: suction peaks that are not as large as twice the static counterpart may very well be experiencing dynamic stall, so the number given here may be a very conservative estimate.

A horizontal-axis wind turbine is thus expected to be subject to dynamic stall conditions, and therefore the performance in this regime should be studied. Bak et al [4] studied the performance of a wind turbine airfoil equipped with an Adaptive Trailing Edge Geometry (ATEG) under attached and completely stalled conditions. For a frequency of actuation $f = 1.63Hz$, corresponding to a reduced frequency $k = 0.084$, it was found that the best decrease in loads oscillations could be obtained when the flap was actuated with a phase shift of 30° before the pitching action under attached conditions. Meanwhile, the optimal phase shift for load reduction became 90° when the airfoil was fully stalled.

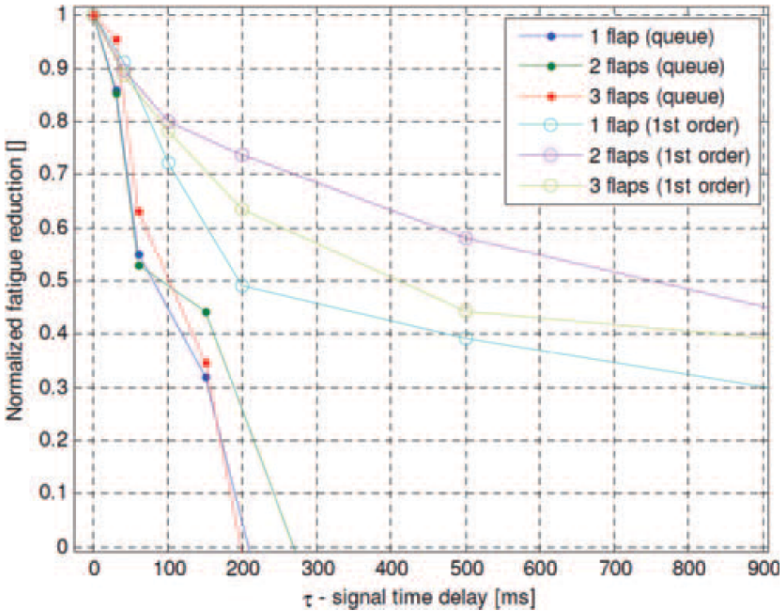

Figure 2.12: Influence of time lag and time delay in the normalized fatigue reduction, as extracted by [2]

In order to study the effects that dynamic stall has on the performance of a Smart Rotor blade, Raiola et al [49] studied a 2-dimensional NACA 0018 airfoil undergoing a prescribed heaving and pitching motion with an actuated trailing edge flap. The flap was actuated with the same frequency as the main wing, and different phase shifts between the motions were considered. Two different cases were studied: case A, where the airfoil was oscillating with a mean angle of 0 degrees; and case B, where the mean angle of oscillations was 9 degrees. The amplitude of oscillations for both cases was 10 degrees, with a reduced frequency $k = 0.1$. Case A was taken to be representative of a fully attached flow, while case B was supposed to experience dynamic stall. For both cases, it was found that when the flap was in-phase with the pitching motion (flapping upwards when the airfoil is pitching up), the load oscillations are reduced, and the moment coefficient curved is rotated with respect to when the flap is not actuated. This can be seen in figure 2.13.

PIV measurements were also done on the oscillating airfoil. An attempt to linearize the contribution of the flap to the lift and the moment coefficient was made, after observing the flow characteristics and noticing that the flap does not change the flow behaviour around the airfoil. This is done by decomposing the lift and the moment into the sum of a term with no flap actuation and another purely dependent on the flap angle. The flap-dependent term is linearized by assuming a linear rate of change of the loads with the flap angle, and obtaining its slope by performing a linear fit on the steady loads for different flap angles. This contribution is then substracted from the actual loads, and the assumption of linearity assessed: if the obtained curves are equal to the ones obtained with no flap actuation, it can be assumed that the hypothesis is valid and that the contribution of the flap can be linearized. This is true for attached conditions when the boundary layer has been tripped at a certain position (10% chord in the experiments). When no tripping of the boundary layer has been performed, or the airfoil is experiencing dynamic stall, the hypothesis is no longer valid. This is due to non-linearities present in these cases.

These experiments only deal with prescribed motions of the flap. There is no active control of the flap actuation, which is a vital part of any Smart Rotor concept. As it has been discussed, several Smart Rotor studies with an active control of the loads have been performed, both numerically and experimentally. However, no attempt has been done to assess the influence that dynamic stall has on the performance of a Smart Rotor. Some numerical studies employ aeroservoelastic codes which model dynamic stall, but there is no further comment on the performance under these conditions, or even if the wind field being investigated is susceptible to dynamic stall. Since dynamic stall has been

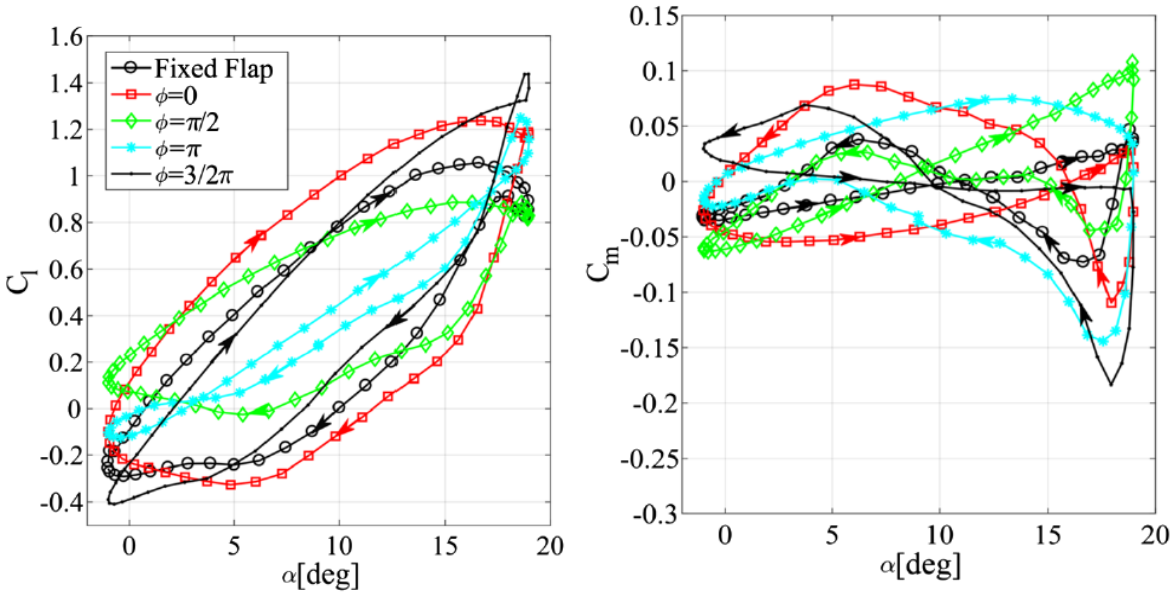

(a) Lift coefficient

(b) Moment coefficient

Figure 2.13: Comparison of the lift and moment coefficient on an oscillating NACA 0018 airfoil for different phase shifts of the flap actuation. α_m = 9° and α_{amp} = 10° . Extracted from [49]

found to occur on horizontal-axis wind turbines, there is some concern in how an active control of the loads such as a Smart Rotor deals with such a complex flow. This lack of knowledge is the gap that is trying to be covered with the present thesis, and this will be done by studying the performance of the proposed controller under both attached and stalled conditions, representative of dynamic stall. This performance will be quantified, and conclusions will be drawn regarding the effectiveness of the controller in terms of reduction of the unsteady loads experienced during dynamic stall conditions.

2.3. Research questions and Objective

The literature review presented in the previous section allowed for an identification of the main aspects present in a Smart Rotor concept, as well as some gaps in the knowledge that need to be studied further. Some conclusions can be drawn about the status of the Smart Rotor research:

- The comparison between different studies is not trivial, since a Smart Rotor concept involves many aspects which influence its final performance. The load reduction capabilities are thus going to be heavily influenced by these aspects and it is difficult to extract conclusions based on the comparison of different studies
- One of the most important aspects in a Smart Rotor is the load altering capabilities of the actuation surfaces. These should be able to compensate for the whole range of loads, if a real comparison between different studies wants to be performed, as it has been shown that the load reduction figures are increased when large actuation surfaces are employed
- Regarding the control architecture, it appears that including the deterministic loads into the control loop improves greatly the performance of the Smart Rotor. More complex forms of control are also expected to improve its performance, although its benefits are not easily seen due to the differences between studies
- Time lags have a big influence on the performance of any Smart Rotor concept. Large time lags make the system uncontrollable, and the main generators of time lags are the actuation velocities and the sensing system. Some sensing systems, the ones measuring the structure deformation, have an inherent time lag due to the delay between loads and deformations on the blade
- A horizontal-axis wind turbine may experience some dynamic stall cycles under certain inflow conditions. Any new concept regarding wind turbines should thus consider the performance under

dynamic stall conditions. This has not yet been done to the author's knowledge, and it may lead to fatigue damage if it is not accounted for

Several decisions have been made regarding the experiments to be performed during the realization of this thesis. As it has been noted, a Smart Rotor is a combination of multiple aspects. The majority of studies have been oriented towards the optimal form of control. This is not deemed necessary in this study, since the focus is not going to be the optimal form of control, but rather the influence that different parameters have on the performance of a Smart Rotor blade. In particular, a lack of studies regarding the performance of a Smart Rotor during dynamic stall was found, and this motivates placing the focus on this phenomenon for the present study. The complexity of dynamic stall is the reason why a simplified study on a 2D-wing model is carried out. Although dynamic stall also generates large oscillations in the moment due to the detachment of the LEV, the control architecture is focused on reducing the loads and not the moment. This is done to be consistent with the current state of the Smart Rotor research, that focuses on reducing the root bending moment on the wind turbines originated from the unsteady loads, but it should be kept in mind the effects that the load control have on the moment oscillations.

The unsteady loads generated during dynamic stall want to be reduced by means of a proportionate controller, acting on the velocity of the flap. This controller is chosen due to its simplicity, as it was stated that the optimal control is not the focus of the present study. In order to fully comprehend the behaviour of the controller to reduce unsteady loads due to dynamic stall conditions, a regime where little flow separation is expected to occur (referred during the thesis as attached flow conditions) will also be analysed, for two reasons: it can be verified that the proposed controller is effective and it will serve as a reference. Besides this, different time lags and frequencies will be studied, since they were found to be crucial for this type of active control during the literature review performed in the previous section. The study to be done can be summarized in the research questions, which guide the realization of the project.

- What are the unsteady load reduction capabilities of a proportionate controller acting on the flap velocity?
  - Is a proportionate controller that is acting on the velocity of actuation of the flap a feasible control mechanism in terms of load reduction capabilities during attached flow conditions?
    - ◊ What are the optimum controller parameters that lead to a higher unsteady load reduction in terms of reduction of standard deviation of the loads?
    - ◊ What is the influence of different frequencies of the unsteady loads on the control capabilities?
    - ◊ What are the limitations of this type of control?
    - ◊ What is the influence of different time lags on the control capabilities?
  - Is the controller capable of performing when dealing with a stalled flow, such as in the dynamic stall regime?
    - ◊ What are the differences between attached and stalled flow in terms of controller response?
    - ◊ What are the aerodynamic phenomena responsible for this response, and what is the influence of time lag and frequency of unsteadiness?
    - ◊ What effect does the control action have on the aerodynamic damping?
    - ◊ Does the actuation of the flap influence the development of dynamic stall?

Answering these questions will naturally orient the project towards the realization of its objective, which is presented again as:

To assess the capabilities and limitations of an active controller in reducing the unsteady loads acting on a blade, by studying the load reduction achieved during attached flow and dynamic stall conditions, in terms of time lag, controller gains, and frequency of unsteadiness on a 2D experimental blade airfoil model.

3

Experimental Setup

In order to answer the research questions presented in chapter 2, a wind tunnel experiment is conducted. During this experiment a 2D rigid blade equipped with a trailing edge flap is the subject of unsteady loading. The ability of a proportionate controller acting on the velocity of the flap to reduce these unsteady loads is tested for different conditions. These different conditions include different frequencies of unsteadiness, different time lags in the control system, and two operational regimes: attached flow and dynamic stall conditions. This chapter presents all the subsystems employed during the experiment to represent these conditions.

A description of the wind tunnel where the experiments are performed and a brief description of the experimental setup is done in section 3.1. The model to be tested is presented in section 3.2. This wing model is equipped with a trailing edge flap that serves as the actuation system, and is described in section 3.2.1, and pressure transducers that serve as the sensing system, presented in section 3.2.2. The pitching mechanism employed to generate the unsteady loads on the blade is described in section 3.3. Lastly, the Data Acquisitions System (DAQ) that gives the model its active load control capabilities is the focus of section 3.4.

3.1. Wind tunnel and General Setup

The experiments are performed in the Open Jet Facility (OJF) of the High-Speed Laboratory (HSL) of the TU Delft. This large scale wind tunnel is located in a room with a width of 13 meters and a height of 8 meters. The test-section of this closed-loop, open jet wind tunnel is $2.85x2.85m^2$, after a contraction ratio of 3:1. The fan driving the wind tunnel is powered by a 500 kW electrical motor, and allows for testing free-stream velocities of up to 35 m/s.

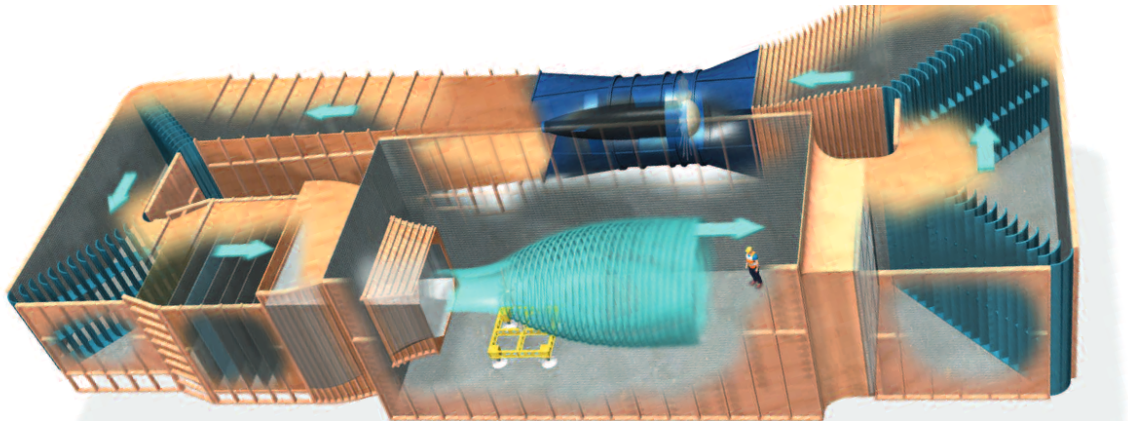

Figure 3.1: Schematic of the OJF of the Delft University of Technology (reproduced from www.tudelft.nl)

The turbulence level of the free-stream velocity one meter after the test section is reported to be lower than 0.5%, with this value increasing to less than 2% when moving 6 meters after the test section, as reported by Lignarolo et al. [40]. These values are obtained with a clean configuration, which is not representative of the experiments performed. During the experiments, large-scale PIV measurements were also carried out, so a seeding rake was introduced in the wind-tunnel, before the contraction section. Giaquinta [26] reported a turbulence level of 0.8% when the seeding rake is placed before the wind tunnel contraction, so it can be concluded that the increase in turbulence from placing the seeding rake is not significant.

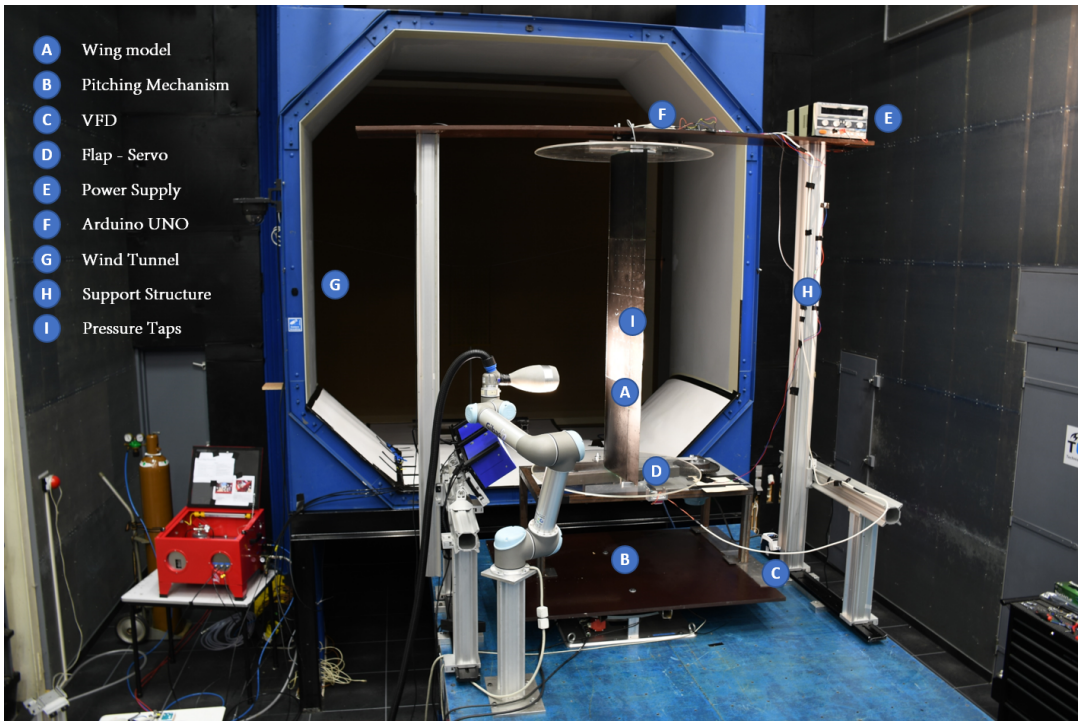

Figure 3.2: General setup employed of the experiment. The subsystems are labeled in the figure

Parameter	Symbol	Value
Free-stream velocity	V_∞	$5\ m/s$
Air viscosity	μ	1.81×10^{-5}
Air density	ρ	$1.206\ kg/m^3$
Chord	c	$0.4\ m$
Span	s	$1.45\ m$
Reynolds Number	Re	1.3×10^5
Mean angle of oscillations	α_0	0.25 (attached flow)° 15.75° (dynamic stall)
Amplitude of oscillations	α_{amp}	4°
Frequency of oscillations	f	$0.2\ Hz$ $0.4\ Hz$ $0.8\ Hz$
Reduced frequency of oscillations	k	0.05 0.1 0.2
Time lag	τ	$32\ ms$ $12\ ms$

Table 3.1: Parameters of the experiment

During the experiment, a wing model is actuated in a sinusoidal motion by means of a pitching mechanism while subject to a constant free-stream velocity of 5 m/s. The oscillations are performed at three different frequencies (corresponding to reduced frequencies of 0.05, 0.1 and 0.2), and for two different mean angles of oscillations. These two different mean angles of oscillations are chosen as

to represent attached flow (oscillations around zero angle of attack) and dynamic stall conditions (oscillations close to the static stall angle). For each of this possible combinations, the unsteady loads acting on the model are integrated using pressure taps present in the model. The proportionate controller reacts to the unsteady loads and sends an actuation signal to the flap in order to reduce the unsteadiness of the loads. Several values of K_p, the proportionate gain of the controller, are tested, as well as two different time lags present in the controller system. The parameters of the experiment are presented in table 3.1, and the experimental setup is shown in figure 3.2. The different combination of parameters is chosen so the research questions layed out during chapter 2 can be answered. The different subsystems involved in the experiment are described in detail in the following sections.

3.2. Wing Model

The experiments are performed on an rectangular wing, which is supposed to be a simplified representation of a wind turbine blade. The wing is obtained by extrusion of a NACA 0018 profile, with a chord of $c = 400\,mm$ and spans a total length of $s = 1455\,mm$, for an aspect ratio of $AR \approx 3.64$. It has been manufactured in parts, and then placed together for the time of the experiments. The middle part is hollow and manufactured in aluminium, and the other parts are manufactured in hard plastic.

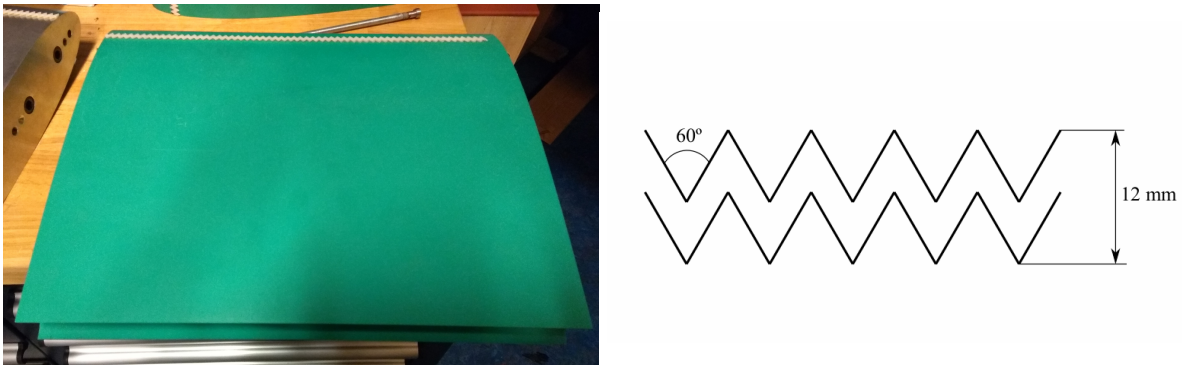

(a) Plastic part of the wing model (green), showing the zig-zag strip (white)

(b) Schematic drawing of the zig-zag strip

Figure 3.3: Picture of one of the parts of the wing model (a), and schematic of the zig-zag strip used to force transition to turbulent flow (b)

The wind tunnel is set to a free-stream velocity of 5 m/s. This corresponds to a Reynolds number of $Re = \frac{\rho V_\infty c}{\mu} = 1.3x10^5$. Due to the Small Reynolds number to be tested, the flow is expected to be laminar, unless the boundary layer is actively tripped. Experiments on the same setup were done by Raiola et al [48, 49], and the influence of tripping the boundary layer studied. It was found a correlation between not tripping the boundary layer and the appearance of a laminar bubble separation. Laminar flow was also responsible for larger oscillations of the pressure fluctuations, and a bigger drop-off in the loads when dynamic stall appears. Based on these findings, the boundary layer is tripped in order to force transition to turbulent flow. A zig-zag strip is placed at 10% chord, with a thickness of 2 mm, a width of 12 mm and an angle of 60°, which can be seen in figure 3.3.

In order to avoid 3D effects due to the development of vortices on the tips of the wing, circular side plates have been placed at each side of the wing. These side plates have a diameter of 0.8 m and impede the flow from going over the tip of the wing.

3.2.1. Actuation System

A trailing edge flap has been added to the wing, in order to give it its load altering capabilities. The trailing edge flap spans the whole wing and has a length of 25% chord. A JR DS8711HV High-Voltage Ultra Torque Servo is used in order to move the whole flap. This servo has an operating voltage of

6.0-7.4V, and a speed of 0.12 seconds/60°, and the range of the flap is limited to $\pm$10°. The servo is powered by a power supply.

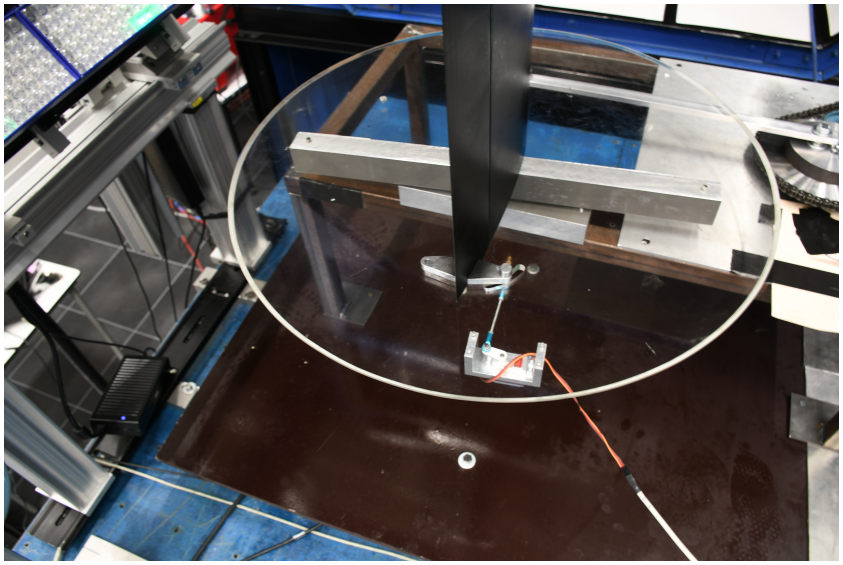

Figure 3.4: Trailing edge flap and servo. The linkage mechanism connecting both can be observed

The servo moves the flap by means of a linkage mechanism, which effectively means that the speed of actuation of the flap is different than the speed of the servo. For the flap to be at 10° the servo is actuated to 49°. When the flap is at -10° the angle of the servo is 104°. This implies that the mean maximum velocity of the flap across its range of motion is approximately 180°/second. This is much larger than the required velocities for attached flow, where at 0.8Hz the maximum expected velocity of the flap is 50°/second, although it may be a limiting factor when dealing with the sudden drop in lift in dynamic stall. Inertial forces are not included in this calculation, so they may also reduce the effective velocity of the flap.

3.2.2. Pressure Transducers

Pressure taps are present in the aluminium part of the wing model, to allow for the installation of pressure transducers, which will be placed inside the model. A total of 48 pressure taps have been placed, 24 on each side. The size of the orifices is 0.4 mm. These pressure taps are placed along a straight line, with an inclination of 15 degrees with respect to the chordline, as to avoid interferences between consecutive pressure taps. The position of the pressure taps can be seen in figure 3.5.

24 differential pressure transducers are used to obtain the instantaneous pressure at the location of the 24 pairs of pressure taps. A differential pressure transducer outputs the difference in pressure between two ports, these two ports being the taps present in the pressure and the suction side of the airfoil. Honeywell HSCSRRN1.6MDSA5 digital differential pressure transducers are used, with a 3 kHz maximum acquisition frequency and an accuracy of $\pm$ 0.004 mbar. They are mounted inside the model, to allow for an instantaneous measurement of the pressure. If they were to be installed outside of the model, the length of the tubing would generate a delay between the measured and the actual pressure, making them unsuitable for the active control of loads.

Pressure transducers are expected to drift from a zero value with time, so a calibration procedure must be done prior to the measurements. A calibration run is performed with no flow, and the average value for each pressure tap is taken as their drift from the true zero value. This calibration run is done with $N_c \approx 400$, so the random error associated with averaging the value of the pressure taps [43] is negligible compared to the systematic error of the pressure transducers itself. Since the calibration value involves subtracting the measured value with the drift obtained in the calibration procedure, the

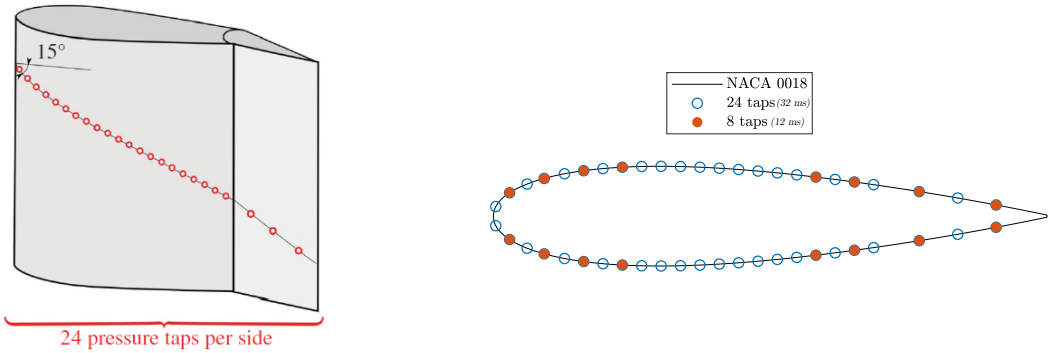

(a) Location of the pressure taps along the span, extracted from [49]

(b) Location of the pressure taps along the chord, showing all the pressure taps present in the model (24 taps), as well as the pressure taps used in the integration scheme with smaller time lag (8 taps)

Figure 3.5: Position of the pressure taps in the model

accuracy of the calibrated value is $\pm$ 0.006 mbar, following error propagation theory.

3.3. Pitching mechanism

A mechanism that introduces unsteady loads on the blade has to be used. This can be done in two ways: introducing unsteadiness in the incoming flow, or moving the model while keeping a constant velocity free-stream. In this experiment the latter is done, and the wing is subjected to a pitching motion as a way of introducing the unsteady loads. This is done by means of a pitching table, specially manufactured for this experiment, with the model installed on top and actuated in a sinusoidal motion. The pitching table is composed of different parts. A frame serves as support of the whole wing, and at the same time allows for the installation of the different components that conform the pitching mechanism.

The main idea behind the pitching mechanism is to transform the angular momentum of a rotating shaft into a sinusoidal motion by means of a linkage mechanism. A flywheel is installed on the rotating shaft, where one end of a linkage bar is fixed at a certain distance from the rotation axis. The other end of the linkage bar is attached to the lower side plate of the wing model. With this linkage mechanism, the rotation of a shaft is converted into a motion that resembles a purely sinusoidal motion. All the components of the pitching mechanism can be seen in figure 3.6.

In this case a rotating shaft is driven by a ABB 3GAA 3-phase AC motor. The power rating of the motor is 0.37 kW. The output angular velocity of the AC motor is constant, at a value of 1355 rpm, which translates to approximately a frequency of 22.6 Hz. The pitching mechanism is supposed to actuate the model at much lower frequencies than this, so as to be representative of the 1P frequencies in an actual rotor blade. In order to reduce the angular velocity of the AC motor, a device called Variable Frequency Drive (VFD) is employed. These type of devices allow for regulating the rotation speed of an AC motor by changing the frequency of the current being fed to the motor. Since the reduction in frequency is rather high, there is some concern in the ability to reach the desired frequencies with simply the VFD. That motivates reducing the angular velocity of the motor in two consecutive steps: After the VFD is used, the angular velocity is reduced again by means of a chain-drive mechanism, with a 4.5/1 ratio effectively reducing the angular velocity of the driven shaft by 4.5 times. For clarity purposes, the shaft driven by the AC motor will be referred to as AC shaft, while the driven shaft will be referred as the main shaft. The rotation of the main shaft will be transformed into the sinusoidal motion of the wing model by means of a linkage mechanism, as it will be described next.

The main shaft (A), where the larger sprocket has been installed, is also driving a flywheel. On this flywheel one end of a linkage bar is attached (B), while the other one is fixed in the side plate of the wing model (D). The rotation of the main shaft causes the side plate to move around the pitching axis (C). In

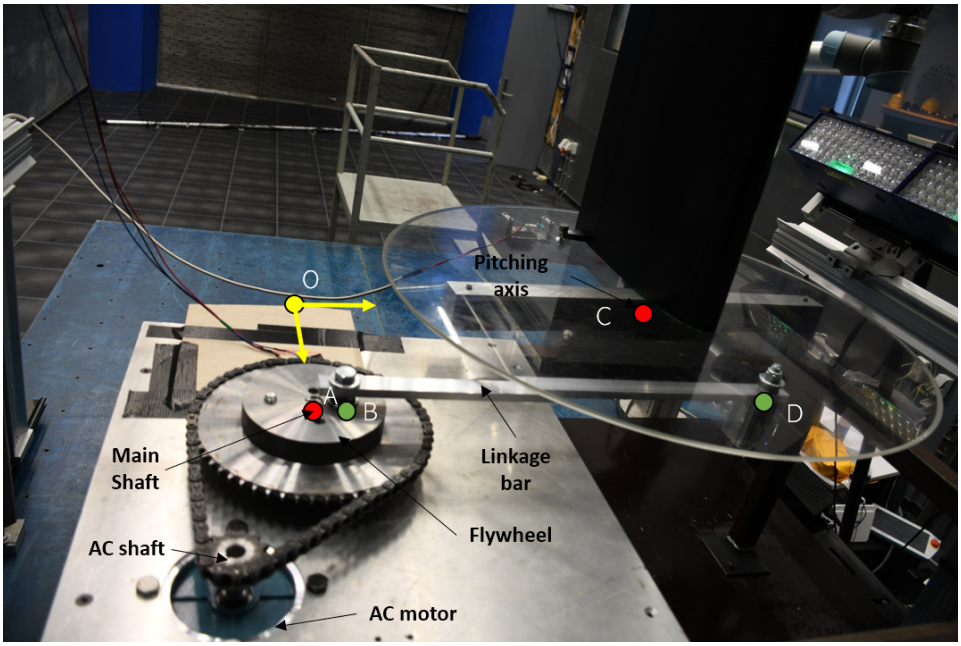

Figure 3.6: Pitching mechanism. The different components have been labeled, as well as the coordinates of the points involved in the kinematics of the system

order to generate a sinusoidal motion around the pitching axis, the points A and C have to be chosen such that an origin of coordinates can be found (O), in which A_y and C_x are zero, and the distance $\overline{OA}$ is equal to the distance $\overline{CD}$. Under these circumstances, and if the distance $\overline{BD}$ is considerably larger than the distance $\overline{AB}$, the rotation of the main shaft will generate a motion that closely resembles a sinusoidal motion around the pitching axis. The similarities with a sinusoidal motion will be larger the larger the ratio $\overline{BD}/\overline{AB}$ is. The kinematics of the system can be expressed as the following set of equations:

$$(D_x - C_x)^2 + (D_y - C_y)^2 = \overline{CD}^2 \tag{3.1}$$

$$(D_x - B_x)^2 + (D_y - B_y)^2 = \overline{BD}^2 \tag{3.2}$$

In these equations the only unknowns are the x and y coordinates of point D. The coordinates of the point C, as well as the distances $\overline{CD}$ and $\overline{BD}$ are fixed and chosen to be as large as possible within the limits of the support structure. The coordinates of the other end of the linkage bar (B) are variable with the rotation of the main axis and also dependent on the desired amplitude of oscillations. This system of equations can thus be solved for different phases of rotation of the main axis, and the y-coordinate of point D translated into an angle of the side plate with respect to the pitching axis. The motion resulting from solving this system of equations is shown in figure 3.7a, for the parameters shown in table 3.2.

	A	C	$\overline{CD}$	$\overline{BD}$	$\overline{AB}$
x [mm]	250	0	-	-	-
y [mm]	0	500	-	-	-
Length [mm]	-	-	250	500	17.4 (4°)

Table 3.2: Parameters of the manufactured pitching mechanism

As it can be seen in figures 3.7a and 3.7b, the differences of the generated motion with a purely sinusoidal motion are almost negligible. For an amplitude of oscillations of 4°, the maximum difference of the motions occur during the mid-upstroke and the mid-downstroke, and has a value of 0.07°, or less

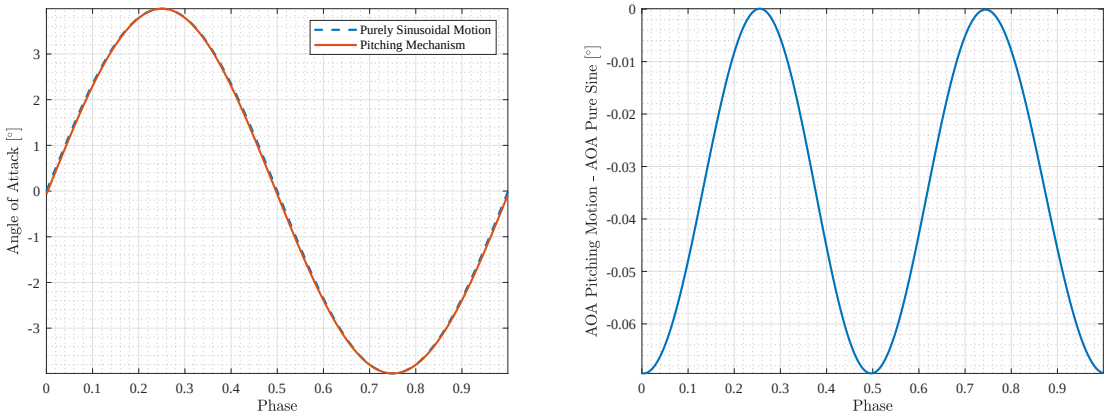

(a) Purely sinusoidal motion and pitching mechanism motion for one revolution, for the parameters in table 3.2

(b) Difference between the pitching mechanism motion and a purely sinusoidal motion, during one revolution

Figure 3.7: Motion of the pitching mechanism

than 2% difference. This is due to the high ratio $\overline{BD}/\overline{AB}$. The length $\overline{AB}$ is chosen as to represent different amplitudes of the oscillations, since it can be derived using basic trigonometry that $\alpha_{amp} \approx \overline{AR}/\overline{CD}$.

The pitching mechanism is responsible for producing the unsteady loads on the blade. In order to answer the research questions laid out in chapter 2 several frequencies of these unsteady loads have to be considered. Therefore, a way to control the frequency of oscillations is needed. The system works by mean of an AC motor, a VFD and a chain drive mechanism. The velocity of the AC motor is constant, as well as the reduction in angular velocity obtained by the chain drive mechanism. The only way to control the frequency of the system is the VFD. The frequency reduction can be specified in the control panel of the VFD, but in order to check which value has to be input in the control panel to obtain the desired frequencies, a way of measuring the angular velocity of the main shaft has to be found. This is done by means of a digital Hall effect sensor, which will be used as a tachometer.

Three magnets are installed in the flywheel of the pitching mechanism, and the sensor is placed in a table just below it. As the shaft rotates, the flywheel and the magnets also rotate. This generates a changing output of the Hall sensor, which can be used to compute the angular velocity of the shaft. A relation between the input on the VFD and the frequency of oscillations is obtained, and in this way several frequencies can be analyzed during the experiment.

Lastly, the pitching mechanism is supposed to generate unsteady loads characteristic of attached flow conditions and dynamic stall. The only way to control this is to control the mean angle of oscillations. For this, the pitching table will be mounted on top of a rotating table present in the OJF of the TU Delft. This table can be rotated and positioned at a desired angle of attack with respect to the incoming flow, and gives the experiment the capabilities to test different flowfields: the attached flow conditions will be tested by positioning the pitching mechanism at a mean angle of around 0°, while dynamic stall conditions will be reproduced by positioning the pitching mechanism at a mean angle close to the static stall angle.

3.4. DAQ

The loads acting on the wing model want to be actively reduced, by means of a proportionate controller. This is implemented within a Data Acquisition System (DAQ). With this DAQ, the loads acting on the airfoil can be detected, and an appropriate actuation signal of the trailing edge flap generated by the controller, in order to reduce the unsteadiness of the loads. The DAQ is in charge of the following tasks:

- Read the signal of the pressure transducers

- Integrate the loads acting on the airfoil using the signal of the pressure transducers
- Generate a signal that moves the actuation system based on the loads acting on the blade, done by the proportionate controller
- Feed this actuation signal in an appropriate manner to the trailing edge flap
- Produce a real-time visualization of the results, as well as the possibility to alter the parameters of the controller
- Generate a file which contains the data obtained during the experiment for further analysis

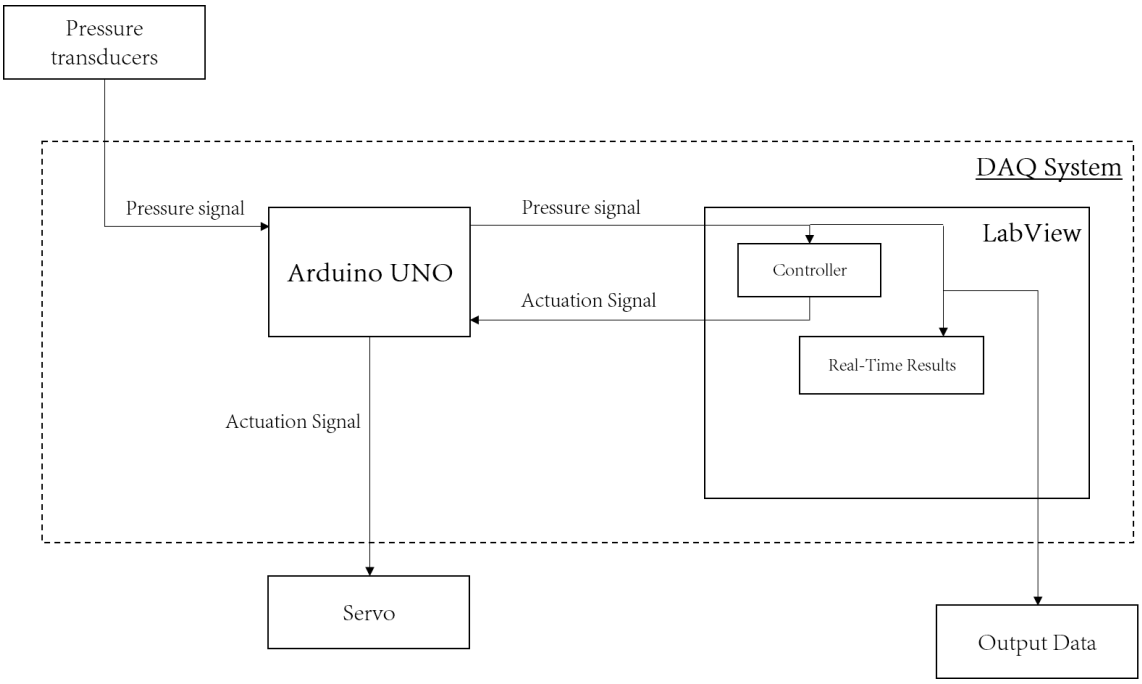

Figure 3.8: Sketch of the DAQ System

The signal being generated by the pressure transducers is fed into an acquisition board, in this case an Arduino UNO, by means of three multiplexers located inside the model. These multiplexers transmit the data of each pressure transducer serially. The data is then sent forward to a project developed in LabView. In this project the loads are integrated following an integration procedure which will be described in section 3.4.1. A proportionate controller is implemented within the project, that uses this signal to generate an actuation signal on the velocity of the trailing edge flap. The actuation of the controller is described by equation 3.3.

$$\dot{\beta} = K_p(C_l - SP) \tag{3.3}$$

where K_p is the value of the proportionate gain, C_l is the lift coefficient acting on the blade, and SP is the Set Point of the controller, which is manually chosen. Based on this value, a signal of the velocity of the flap $\dot{\beta}$ is generated. This actuation signal is transformed into an appropriate input for the position of the servo, and send back to the Arduino UNO board. The Arduino UNO is connected to the servo and transmits the signal. A schematic of the control loop is visualized in a diagram in figure 3.8. In this diagram it can be seen that the LabView project is in charge of producing a real-time visualization of the results that allows to verify the correct behaviour of the controller, and is also in charge of generating the output data that will be analysed in the following chapters.

3.4.1. Load Integration

The loads acting on the airfoil are detected with pressure transducers installed in the wing model. Pressure transducers provide a more detailed description of the flow, as it was discussed in the literature review in chapter 2, which is especially important for testing dynamic stall conditions. The values of these pressure transducers are integrated to obtain the loads acting on the blade.

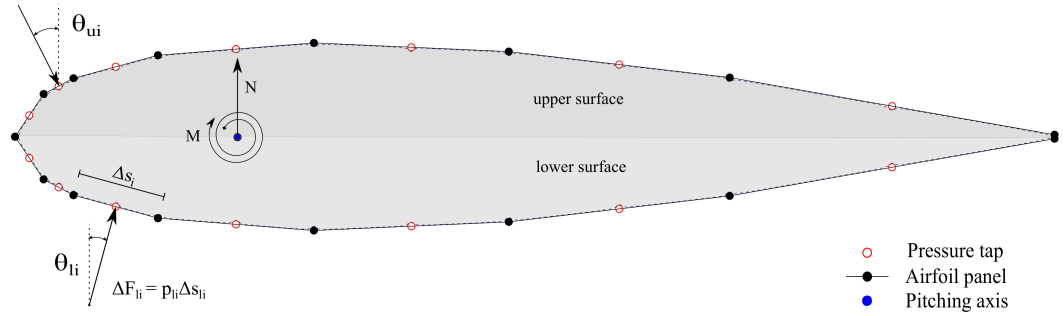

Figure 3.9: Position of the pressure taps in thee wing model, as extracted from [49]

The differential pressure given by the pressure transducers is used to obtain the loads experienced by the airfoil. The airfoil is divided into several panels, as it can be seen in the figure 3.9. In the middle of each panel a pressure tap is present, so the load acting on the panel can be obtained by multiplying the value of the pressure (p_{li}) with the length of the panel (Δs_{li}). In the diagram the subscript l denotes a panel present in the lower side of the airfoil, while u denotes a panel in the upper part. The total load acting on the airfoil per unit span can be obtained by summing the individual loads acting on each panel:

$$n \approx \sum_{i=1}^{N_p} \Delta f_{li} cos(\theta_{li}) - \sum_{i=1}^{N_p} \Delta f_{ui} cos(\theta_{ui}) = \sum_{i=1}^{N_p} p_{li} \Delta s_{li} cos(\theta_{li}) - \sum_{i=1}^{N_p} p_{ui} \Delta s_{ui} cos(\theta_{ui}) = \sum_{i=1}^{N_p} p_{li} \Delta x_{li} - \sum_{i=1}^{N_p} p_{ui} \Delta x_{ui} \tag{3.4}$$

Note that the definition of the panel angle θ is different for the upper and lower surfaces. These angles are defined in this way so that they are the same in the upper and lower surface for a symmetric airfoil. In our case we are dealing with a symmetrical airfoil and the position of the pressure taps is the same in the upper and the lower surface, so the previous expression can be simplified and expressed as the pressure differential for each pair of taps, which is the value obtained by the differential pressure transducers:

$$n \approx \sum_{i=1}^{N_p} \Delta p_i \Delta x_i \tag{3.5}$$

The pressure distribution on the airfoil is also going to generate a moment around its pitching axis. The same procedure can be used in order to obtain the moment around the pitching axis, (x_m,y_m):

$$m \approx \sum_{i=1}^{N_p} \Delta f_{li} cos(\theta_{li})(x_m - x_{p_{li}}) + \sum_{i=1}^{N_p} \Delta F_{li} sin(\theta_{li})(y_m - y_{li}) - \sum_{i=1}^{N_p} \Delta f_{ui} cos(\theta_{ui})(x_m - x_{p_{ui}}) + \sum_{i=1}^{N_p} \Delta F_{ui} sin(\theta_{ui})(y_m - y_{ui}) \tag{3.6}$$

As it was done with the normal loads, the expression for the moment on the airfoil can be simplified. It has to be noted that for a symmetric airfoil $x_{li} = x_{ui}$ and $y_{li} = -y_{ui}$. If besides $y_m = 0$, which is a

reasonable choice of pitching axis, the expression for the moment can be expressed as a function of the pressure difference in each pair of pressure taps:

$$m \approx \sum_{i=1}^{N_p} \Delta p_i \Delta x_i (x_m - x_{p_i}) - \sum_{i=1}^{N_p} \Delta p_i \Delta y_i y_{p_i} \tag{3.7}$$

Considering infinitely small panels, the summations shown in the previous equations can be expressed as integrals, in the following form:

$$n = \int_{LE}^{TE} \Delta p dx \tag{3.8}$$

$$m = \int_{LE}^{TE} \Delta p (x_m - x) dx - \int_{LE}^{TE} \Delta p y dy \tag{3.9}$$

This integration procedure is dependent on the number of pressure taps used. Using the signal of the 24 pressure transducers present in the model gives a more accurate value of the integrated loads, but increases the time lag present in the system, and hence is expected to worsen the performance of the controller. The time lag introduced during the control loop for the integration scheme using 24 pressure taps is 32 ms. This time delay is inherent to the sensing system. Since the effect of time delays on controller capabilities wants to be studied, an alternative integration scheme that reduces the time lags is proposed. This new scheme uses only 8 pressure taps for the load integration, which reduces the time lag present in the control loop to 12 ms. The location of these taps is also shown in figure 3.5b. Further explanation on the choice of these pressure taps will be carried out during the Methodology chapter.

The normal force and the moment can be non-dimensionalized with the following expressions, and the lift coefficient obtained by multiplying the normal force coefficient with the angle of attack of the model chord with respect to the free-stream velocity, α. The pressure coefficient is also introduced, as it will be used in the following chapter for computing the uncertainty associated with the results. Note that C_p actually indicates the difference in pressure coefficient between the upper and lower surface of the airfoil:

$$C_p = \frac{\Delta p}{1/2 \rho V_\infty^2} \tag{3.10}$$

$$C_n = \frac{n}{1/2 \rho V_\infty^2 c} \tag{3.11}$$

$$C_m = \frac{m}{1/2 \rho V_\infty^2 c^2} \tag{3.12}$$

$$C_l = C_n cos(\alpha) \tag{3.13}$$

The normal force and moment coefficient can also be obtained directly using equations 3.8 and 3.9 if the pressure is non-dimensionalized with expression 3.10 and the distances are non-dimensionalized with the chord (non-dimensional distances will have the superscript *).

Summarizing, the pitching mechanism reproduces unsteady loads under attached flow and dynamic stall conditions, at different frequencies, on the 2D wing model described in section 3.2. These unsteady loads are detected by integrating the signal of the pressure transducers installed inside the wing model, and reduced by deflecting the trailing edge flap, based on the signal given by the controller using equation 3.3. Two different integration schemes are used, employing all 24 and just 8 pressure taps, which corresponding to a time lag in the controller system of 32 and 12 ms respectively. This allows to test the effect of the time lag in the load reduction capabilities of the controller. The data from the pressure transducers is stored, and analysed during the following chapters.

4

Methodology

Instantaneous pressure data is stored during the experiment described in chapter 3. This data is integrated and the unsteady loads acting on the 2D wing model obtained. The controller ability to reduce the unsteady loads is assessed based on these results. The methodology applied to the data to obtain the results and extract conclusions from it is described in this chapter. The pressure data is integrated with two different integration schemes, and the loads acting on the blade are obtained. A study into the discretization errors arising from this procedure is carried out in section 4.1. The instantaneous loads acting on the blade are obtained, and wind-tunnel corrections applied following the methodology in section 4.2. The instantaneous loads are phase-averaged, as described during section 4.3, and the uncertainty of these phase-averaged loads is derived in section 4.4. The aforementioned procedures are performed to obtain the loads and moments acting on the blade and to increase the confidence in the results. The last section of this chapter, section 4.5, deals with the data analysis. Several methodologies are proposed so that the performance of the controller can be assessed.

4.1. Discretization Errors

As it was discussed during section 3.2.2, the loads acting on the blade are integrated based on the signal of the pressure transducers. The maximum acquisition frequency of each individual differential pressure transducers is 3 kHz. However, due to sizing constraints, the signals of the 24 pressure transducers are taken out of the model by means of 3 multiplexers also present inside the hollow aluminium section. The output signal of the multiplexers is fed into the DAQ board, in this case an Arduino UNO, which reads the signal of the multiplexer by means of a I2C serial bus communication. This effectively means that each pressure sensor is read one after the other, and the maximum effective acquisition frequency is reduced.

This is the motivation for using a reduced number of pressure taps in the loads integration scheme. An alternative integration scheme is thus proposed, employing 8 pressure taps. This effectively reduces the time lag of the controller system from 32ms when all 24 pressure taps are used, to 12ms using just 8 pressure taps. The effect of the time lag can then be tested.

The choice of the pressure transducers to be used with this new integration scheme is not trivial, since the integrated loads are supposed to be representative of the real loads acting on the airfoil. 4 of the pressure transducers chosen are in the fore section of the airfoil, and in that way the suction peak is still represented, which is one of the main contributors to the loads acting on the airfoil. The remaining 4 are situated within the aft section of the airfoil, two of them situated on the trailing edge flap: this location is motivated by the fact that the trailing edge is going to be actuated, and thus the loads are going to be heavily influenced by the pressure distribution around it. The location of the 24 pressure taps is represented in figure 3.5, as well as the pressure taps employed when only 8 transducers are used. In both cases, two extra points have been added for integration purposes, at the leading and trailing edge, since the pressure differences at those locations are known to be zero.

The reduction of pressure taps to be read raises concern about possible discretization errors introduced during the integration of the loads. In order to quantify the effects that the discretization has on the integrated loads, both when using 24 and 8 pressure taps, a preliminary study is done with pressure data obtained for the NACA 0018 at different angles of attack with XFOIL. A viscous analysis with a Reynolds number of $1.3x10^5$ and tripping of the boundary layer at $0.1c$ is performed, to be more representative of the present study. The airfoil is divided into a variable number of panels, and the normal force and the moment acting on it integrated, according to equations 3.8 and 3.9 respectively, following the trapezoidal rule for numerical integration. The results shown here are obtained for a single angle of attack of 6°, as no significant differences were found for different angles of attack.

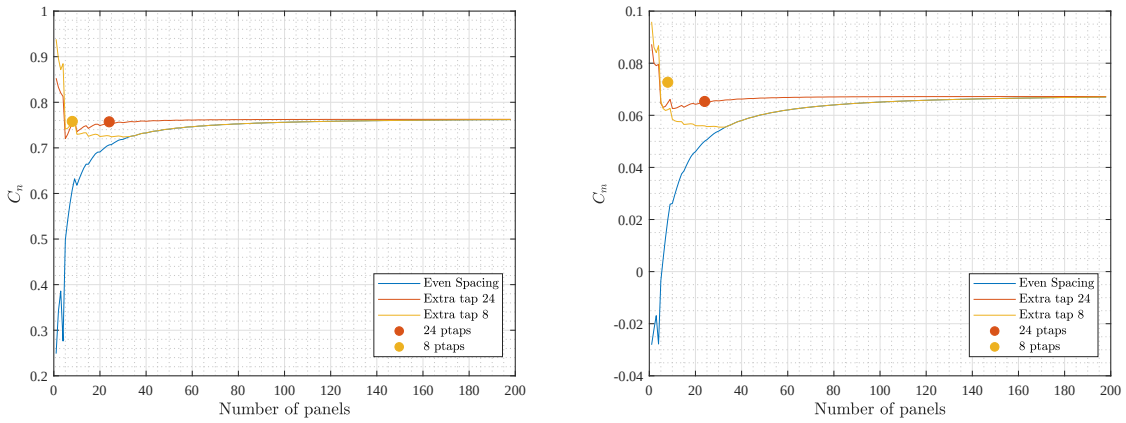

(a) Normal force coefficient

(b) Moment coefficient

Figure 4.1: Convergence of the normal and moment coefficient on a NACA 0018 for a variable number of panels with different discretization techniques, obtained with XFOIL at $\alpha = 6°$, and comparison with the results obtained for the two integration schemes proposed in the experiment (24 ptaps and 8 ptaps)

Three different discretizations of the airfoil are performed. First, the airfoil is divided into a variable number of panels with even spacing. This discretization will be referred as *Even Spacing*. However, this is not fully representative of the actual position of the pressure taps in the experimental model. The pressure taps are placed so as to have a finer discretization near the leading edge. In particular, the location of the first pressure tap is expected to be crucial in the integration scheme, so two more discretizations are tested: in one of them a pressure tap is added at 0.0044c, the location of the first pressure tap used in the integration scheme for 24 pressure taps. This will be referred as *Extra tap 24*. In the other one, the added pressure tap is present at 0.0294c, which is where the first pressure tap of the 8 pressure tap integration scheme is situated, and it will be referred as *Extra tap 8*. The convergence of the integrated normal force and moment coefficient is shown in figure 4.1, and quantified in table 4.1. For a certain confidence interval, this is defined as the number of panels needed for each method to reach that level of convergence, expressed as percentage of the value obtained for the finest discretization studied, which is taken as the true value $C_{n,true}$ or $C_{m,true}$.

As it can be seen, the convergence for the evenly spaced panels with no extra pressure taps is slow. However, adding a pressure tap near the leading edge improves significantly the accuracy of the integration for a small number of panels. This highlights the importance of capturing the suction peak in the integration of the loads.

The results obtained for the 24 and 8 pressure taps integration schemes are also shown in figure 4.1. For the normal force, both integration schemes match pretty well with their respective models *Extra tap 24* and *Extra tap 8*. This is not the case for the moment integration, where the 24 pressure taps integration scheme matches its respective model, but the integration scheme for 8 taps does not. This is ascribed to the uneven distribution of pressure taps, with a lack of pressure taps in the middle of the model. The trapezoidal integration that is being performed is first order accurate. This

		Convergence			
		80%	**90%**	**95%**	**99%**
C_n	*Even spacing*	8	18	33	88
	Extra tap 24	2	2	6	27
	Extra tap 8	2	5	6	88
C_m	*Even spacing*	31	51	78	147
	Extra tap 24	2	7	18	46
	Extra tap 8	2	51	78	147

Table 4.1: Convergence of C_n and C_m, expressed as the number of panels required to achieve convergence to a certain percentage of the true value $C_{n,true}$ and $C_{m,true}$ (obtained with the finest discretization), for different confidence levels

implies that for the normal coefficient, the variation of the pressure distribution along the midchord is effectively considered as linear. While not completely true, the errors arising from this assumption can be considered small. However, the contribution to the moment (arising from equation 3.9) is going to be one order higher than the pressure distribution, and therefore errors are going to be present even if the pressure distribution varies linearly. To remedy this, extra points are added in the midchord, interpolated from the 4th and the 5th pressure taps in the 8 pressure tap integration scheme. This does not affect the integration of the normal force but is expected to reduce the error of the moment integration. Results are shown in figure 4.2, and show that the errors are reduced, specially for small number of panels, and that the moment integrated with the 8 pressure taps scheme matches well with the discretization *Extra tap 8*.

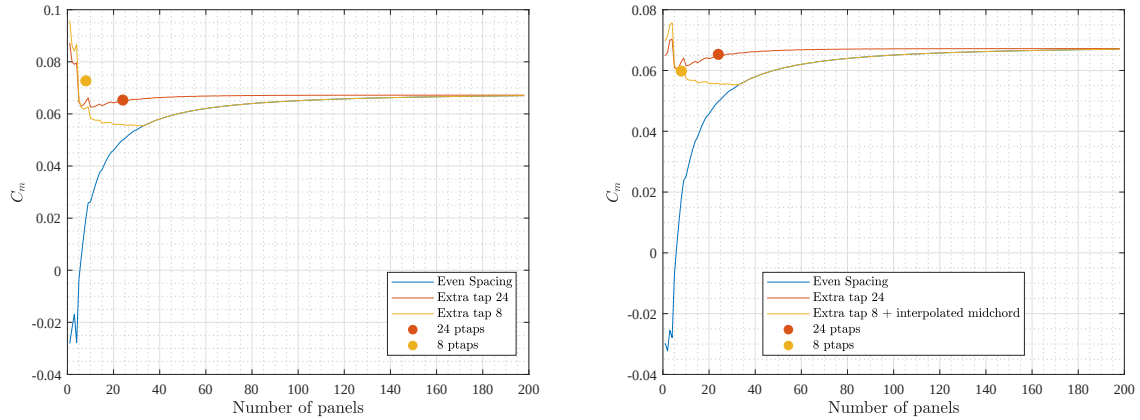

(a) Without mid-chord interpolation

(b) With mid-chord interpolation

Figure 4.2: Comparison of the convergence of the moment coefficient on a NACA 0018 for a variable number of panels and different discretization techniques, obtained with XFOIL at $\alpha = 6°$, when no points are interpolated in the mid-chord (a), and when mid-chord interpolation is used (b)

Based on this discretization study, both integration schemes are able to accurately capture the normal force acting on the airfoil, with confidence levels higher than 95%, and close to 99% for the scheme that uses all 24 pressure taps. The convergence of the moment is also higher than 95% for the 24 pressure tap integration scheme, albeit smaller for the integration with only uses 8 pressure taps, which is expected to converge to at least 80% of the true value. To further assess the validity of the integration scheme with reduced time lag, a comparison of the values obtained during a experimental run with flap actuation are shown next. The run corresponds to oscillations of 4 degrees amplitude around 0°.

The results are shown in figure 4.3. The cross-correlation coefficient at zero-lag is computed, with values of 0.9948 for the normal coefficient and 0.9976 and 0.9983 for the moment coefficient without and with mid-chord interpolation. For the scheme to be accurate in the integration of the loads, not only high values of the cross-correlation are needed, but also a good agreement between the amplitude of

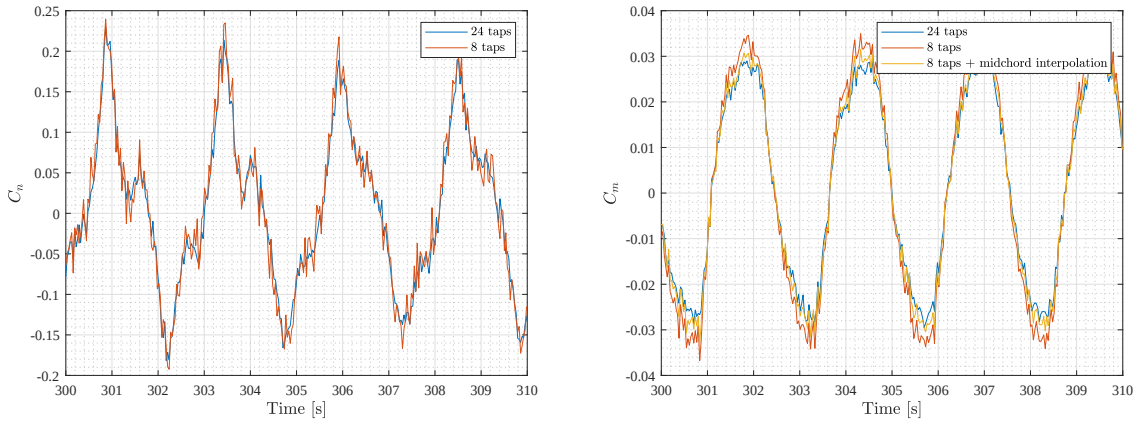

(a) Normal force coefficient

(b) Moment coefficient

Figure 4.3: 10 seconds extracts of the normal force (a) and moment (b) coefficients obtained with the different discretization schemes proposed. Experimental run corresponds to attached flow conditions at 0.4 Hz and 4° amplitude.

the signals. For the normal loads it can be seen in figure 4.3a that both signals match significantly. For the moment, if no midchord interpolation is done a overestimation of the moment coefficient is obtained, while the agreement is much better when the midchord interpolation is performed. This can be quantified by looking at the Root Mean Square of the Error (RMSE) of the signals. This value is presented as a percentage with respect to the maximum amplitude of the force and moments. A value of 3% error for the normal coefficient between the two integration schemes is found, while for the moment coefficient the error is around 10% for the scheme without mid-chord interpolation, and 4% with. This is in agreement with the results shown in the correlation study, and therefore this type of interpolation will be the one employed in the results section.

4.2. Wind Tunnel Corrections

As in any experimental study done on a wind-tunnel, the data obtained is not fully representative of real-world conditions. Once the loads have been obtained, some corrections have to be done in order to account for these discrepancies, and these corrections change depending on if we are dealing with an open or closed section wind tunnel. A summary of wind-tunnel corrections is presented in [24]. The corrections for an open wind-tunnel, although typically smaller in magnitude that their closed section counterpart, are difficult to quantify due to the lack of defined boundary conditions at the test section. The main corrections for this type of wind tunnel are lift interference, solid blockage and wake blockage. Wake blockage is difficult to quantify in an open wind tunnel and can be considered negligible for most cases [24]. The corrections due to solid blockage are also expected to be small. The procedures in [24] are followed for the calculation of this blockage. Considering the area of the test section to be 2.85x2.85 m^2, the maximum model blockage, which is obtained for a maximum angle of attack $\alpha_{max} \approx 20°$, corresponding to a frontal area of 0.22 m^2, is less than 1% velocity variation. Based on this value, the corrections due to solid blockage are neglected.

The only correction that will be applied is thus the lift interference, that occurs because the lift being generated by the wing changes the streamline of the flow and modifies the effective angle of attack. The procedure described by Brooks [12] is followed, derived by using an airfoil and image system based on lifting surface theory. The correction for the effective angle of attack has the following expression:

$$\alpha = \alpha_t - \frac{\sqrt{3\sigma}}{\pi} C_{Lt} - \frac{2\sigma}{\pi} C_{Lt} - \frac{\sigma}{\pi} 4 C_{Mt} \tag{4.1}$$

where

$$\sigma = \frac{\pi^2}{48}\left(\frac{c}{h_t}\right)^2 \tag{4.2}$$

h_t is the height of the tunnel and the subscript t represents the measured values of the lift and moment coefficients. This correction effectively implies a reduction of the effective angle of attack. The correction procedure is similar to the one performed in [25], where the effective angle of attack was 2° smaller than the geometrical angle of attack for a $C_l = 1$, $c = 0.45m$ and $h_t = 3.4m$. Both experimental setups share some similarities, employing large-scale open-jet wind tunnels for surface pressure measurements of a 2D-airfoil. The wind tunnel corrections will be shown during the results chapter, and similar values are found as in the experiment by Fulgslang et al [25].

4.3. Phase-averaging

The loads acting on the blade correspond to one of the 12 runs performed during the experiment, summarized in table 4.2. Each run of the experiment is defined as a unique combination of frequency, time lag, and type of regime: attached flow or dynamic stall.

	Regime	Frequency [Hz]	Time Lag [ms]
Run 1	Attached Flow	0.2	32
Run 2	Attached Flow	0.2	12
Run 3	Attached Flow	0.4	32
Run 4	Attached Flow	0.4	12
Run 5	Attached Flow	0.8	32
Run 6	Attached Flow	0.8	12
Run 7	Dynamic Stall	0.2	32
Run 8	Dynamic Stall	0.2	12
Run 9	Dynamic Stall	0.4	32
Run 10	Dynamic Stall	0.4	12
Run 11	Dynamic Stall	0.8	32
Run 12	Dynamic Stall	0.8	12

Table 4.2: Runs performed during the experiment

During each run the gain K_p of the controller is varied, and for each value of K_p tested, pressure data from each individual transducer is recorded for a total of 120 seconds. For the three different frequencies, 0.2Hz, 0.4Hz and 0.8Hz, this means that around 24, 48 and 96 cycles of representative data are going to be stored. The time of each cycle is non-dimensionalized into a phase value, expressed as $\phi = t/T = tf$, where T is the period of oscillations, or the inverse of the frequency.

A phase-averaging procedure is followed, to condense the multiple cycles into a phase-averaged value. The hall sensor, which was introduced during section 3.3, produces an output based on the detection of the magnetic-field induced by a magnet. One of the magnets was placed in such a position that the hall sensor changed output when crossing the mean angle of oscillations during the upstroke. This signal was stored, and used in order to set the zero-phase for every cycle. Once each case is divided into its multiple cycles, it can be averaged to give us the phase-averaged data. This phase-averaged value is more statistically significant, since the standard deviation of the mean value is reduced for an increasing number of cycles used [43].

4.3.1. Cycle filtering

The phase-averaging procedure described above is pretty straightforward when applied to the attached flow cases. However, during the dynamic stall runs it was found that not all the cycles were fully representative of dynamic stall conditions. Some of the cycles did not recover from stall, and therefore can not be considered as experiencing a dynamic stall cycle for analysis purposes. This is ascribed to the small amplitude of the oscillations and the stochastic nature of flow reattachment.

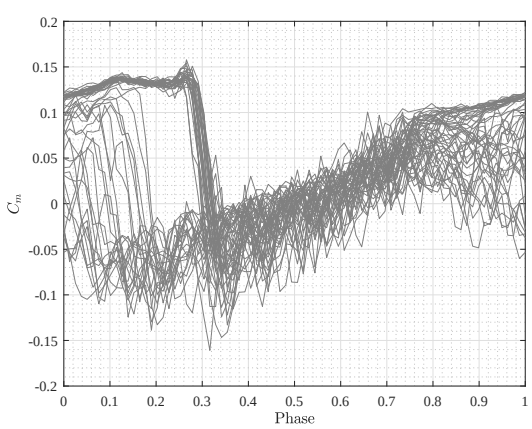

(a) Moment coefficient cycles before cycle filtering

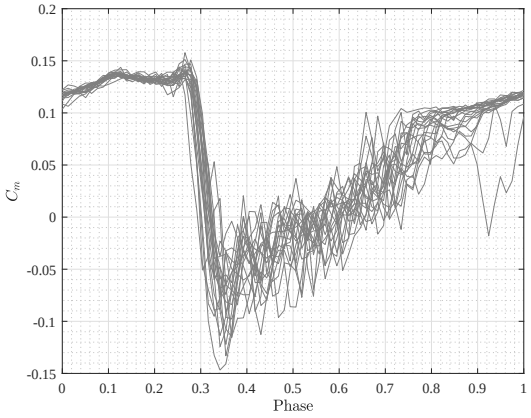

(b) Moment coefficient cycles after cycle filtering, removing the outliers

Figure 4.4: Moment Coefficient Cycles before and after removing outlier with cycle filtering, for 0.4Hz, 24 pressure taps and no active load control

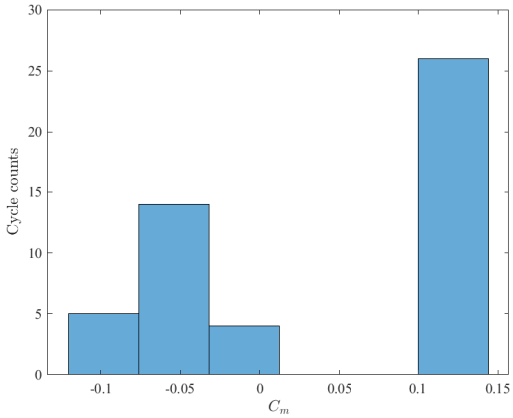

(a) Histogram of the moment coefficient at phase = 0.25

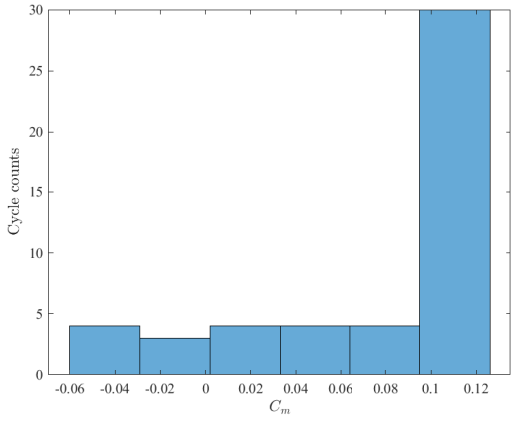

(b) Histogram of the moment coefficient at phase = 1

Figure 4.5: Histograms of the moment coefficient (before cycle filtering), before the dettachment of the LEV (Phase = 0.25) and at the end of the cycle (Phase = 1), for 0.4Hz, 24 pressure taps and no active load control

Only the cycles that are representative of dynamic stall should be included in the phase-averaging procedure. A methodology that filters out the unrepresentative cycles is thus developed. As it was mentioned before, some cycles do not recover from the stalled conditions. This has an effect on the lift and moment generated on the blade. By looking at the integrated moment, two main differences between attached and stalled conditions can be observed:

- The standard deviation of the moment between cycles is much larger when the flow is stalled than when it is attached
- The moment acting on the blade when the flow is attached is larger in magnitude than when the flow is stalled

For each case of the dynamic stall runs, a histogram of the moment at two specific phases of each cycle is taken: before the separation of the LEV (identified by the drop in moment), and at the end of the cycle. Based on the observations pointed before, the cycle experiencing dynamic stall, which should be attached at both of these points, should be concentrated (due to the smaller standard deviation) around the highest value (due to the moment being larger). As an example, the filtering done for Run 9 when the value of K_p is zero is shown in figures 4.4 and 4.5. It can be seen that the outliers, which

can be identified in figure 4.4a, have been eliminated after the cycle filtering has been applied, in figure 4.4b. The histograms are taken at two different phases of each cycle, 0.25 and 1, and are shown in figure 4.5. Only the cycles that fall into the last binding for both phases, figures 4.5a and 4.5b, are kept after the cycle filtering.

This procedure is applied to every case of the dynamic stall runs. The histograms are divided into 6 different bins, as this was found out to be the best compromise between removal of the unrepresentative cycles while keeping a large number of cycles that were actually representative of dynamic stall. Since the detachment of the LEV is frequency dependent, the position of the first histogram is variable: for 0.2Hz it is done at phase 0.15, for 0.4Hz at 0.25 and for 0.8Hz at 0.37. The second histogram is always taken at the end of each cycle.

4.4. Uncertainty of the Results

As it was described in section 4.3, a phase-averaging procedure is performed to produce statistically significant results. This is done to reduce the high variability of data between cycles, and phase-averaged values of the pressure transducers for each case are obtained. According to Moffat [43], the uncertainties in an experimental result can be divided into bias and random errors. The bias errors are fixed, and in this experiment can be thought of as the accuracy of the measurement instruments. The random errors arise from the measurements itself, and represent the level of noise of the experiment.

$$U_{\overline{x},0.95} = \sqrt{B_x^2 + tS_{\overline{x}}^2} \tag{4.3}$$

where $U_{\overline{x},0.95}$ represents the uncertainty of the measurement x at 95% confidence interval, B_x are the bias errors and $S_{\overline{x}}$ is the precision index, which is a measure of the random error. t is the Student's t distribution [43]. The uncertainty on both the lift and moment coefficient needs to be computed. The bias errors can be calculated based on error propagation theory as follows, since it can be assumed that there is no correlation between the different instruments accuracies:

$$B_{C_l} \approx \sqrt{\sum_{i=1}^{N} \left(B_{C_{pi}} \Delta x_i *\right)^2} \tag{4.4}$$

$$B_{C_m} \approx \sqrt{\sum_{i=1}^{N} (B_{C_{pi}} \Delta x_i * (x_m * - x_{p_i} *))^2 + \sum_{i=1}^{N} (B_{C_{pi}} \Delta y_i * y_{p_i} *)^2} \tag{4.5}$$

which both depend on the uncertainty of the pressure coefficient computed with each value of the pressure transducers, and can be expressed as:

$$B_{C_p} = \sqrt{\left(\frac{2}{\rho V^2} B_{\Delta p}\right)^2 + \left(\frac{2\Delta p}{\rho^2 V^2} B_\rho\right)^2 + \left(\frac{4\Delta p}{\rho V^3} B_V\right)^2} \tag{4.6}$$

For this calculation it is assumed that the bias error of the normal coefficient is equal to the bias error of the lift coefficient, which corresponds to a low uncertainty of the angle of attack. It can be seen that the bias error associated with the lift and the moment coefficient are dependent on the bias error of each pressure coefficient, and these values are dependent on the bias errors of the measurements, namely the pressure transducers, the density and the velocity. The bias error of each pressure transducer is 0.006 mbar, as it was shown in section 3.4.1. The bias error of the velocity and the density is taken as the last significant digit of the measurement instruments. It is found that the driving force of the bias error in the result are the pressure transducers. Neglecting the errors for velocity and density, a consistent value for the bias errors is found, dependent on the integration scheme employed:

	B_{C_l}	B_{C_m}
24 pressure tap	0.0086	0.0037
8 pressure tap	0.0107	0.0045

Meanwhile, the precision indexes $S_{\overline{C_l}}$ and $S_{\overline{C_m}}$ cannot be calculated with the previous formula. This is due to the heavy correlation between some of the measurements, such as the velocity and the value of the pressure transducers, and specially between the different pressure transducers. As such, it is estimated directly from the results, and taken as the standard deviation of the C_l and C_m divided by the square root of the number of samples:

$$S_{\overline{x}} = \frac{\sqrt{\frac{\sum_{i=1}^{N} (\overline{x} - x_i)^2}{N-1}}}{\sqrt{N}} \tag{4.7}$$

Once the random error is known, the uncertainty of the measurement can be computed by using the values computed before and an appropriate value of t representative of a confidence interval of 95%. The values of uncertainty are going to be case and phase dependent, and will be reported during the results chapter.

4.5. Data Analysis

Until now, the methodology employed to convert the instantaneous values of the pressure transducers into phase-averaged values of lift and moment coefficient has been described. Once these loads and moments are obtained, they have to be analysed so that the research questions can be answered. Several techniques are used to assess the performance of the controller, and are described next:

4.5.1. Standard Deviation Reduction

The purpose of the controller is to reduce the fatigue introduced by the unsteady loads acting on the blade. The reduction of the unsteadiness on the loads is computed by looking at the standard deviation of the signals, and the reduction that is observed when the flap is actuated with different values of K_p. The standard deviation of the lift and moment coefficient can be defined as:

$$Std(x) = \sqrt{\frac{\sum_{i=1}^{N} (\overline{x} - x_i)^2}{N-1}} \tag{4.8}$$

The lower the standard deviation of the lift is, the smaller the fatigue damage is expected to be. As such, the performance of the controller is assessed based on the value of this parameter for the difference cases. Note that from now on the standard deviation of any parameter x will be expressed as $Std(x)$

4.5.2. Aerodynamic Damping Influence

As it was discussed during chapter 2, another important aspect in an airfoil undergoing unsteady motion is the aerodynamic damping. This is a measure of the energy extracted from the wind by the airfoil. For an airfoil undergoing an oscillatory motion, the aerodynamic damping can be expressed as:

$$\Xi_{cycle} = -\frac{1}{\pi \alpha_{amp}} \oint C_m d\alpha \tag{4.9}$$

where the moment coefficient is evaluated with respect to the pitching axis. For this experiment, the unsteady loads generate a response in form of flap actuation, that modifies the moment coefficient around the pitching axis. In this sense, the effect of the controller in the aerodynamic damping can be

thought of as the sum of two contributions: the pitching moment coefficient of the baseline case, with no flap actuation, and the extra moment coefficient induced by the flap motion:

$$\Xi_{cycle} = -\frac{1}{\pi\alpha_{amp}} \oint \left(C_{m,0} + C_{m,f}\right) d\alpha = \Xi_{cycle_0} + \Xi_{cycle_f} \tag{4.10}$$

The actuation of the flap contributes positively or negatively to the aerodynamic damping with the factor Ξ_{cycle_f}. The effect that the active control of loads has on the susceptibilities to aerodynamic instabilities of the blade is determined by looking at this parameter.

4.5.3. Spectral Analysis

The controller is designed to reduce the unsteady loads generated on the blade, which in this experiment correspond to 0.2Hz, 0.4Hz or 0.8Hz, depending on the run. These are supposed to be representative of the 1P frequencies of a real wind turbine blade. However, the actuation of the trailing edge flap may introduce some unwanted components in other frequencies. A spectral analysis is performed, to understand the effect of the controller in the whole frequency spectrum.

This is done by means of the Fourier transform [47], which transforms a continuous time-signal into its equivalent continuous spectrum, and can be expressed as:

$$X(jw) = \int_{-\infty}^{\infty} x(t) e^{-jwt} dt \tag{4.11}$$

The Discrete Fourier Transform (DFT), can also be thought of the discrete equivalent of the Fourier transform for discrete time-signals. It can be expressed as a summation:

$$X(jw) = \sum_{k=0}^{N-1} x(k) e^{-jwkT} dt \tag{4.12}$$

where T is the sampling time and N is the number of samples of the signal. This signal will be computed in Matlab by performing the Fast Fourier Transform (FFT). This algorithm drastically reduces the computational time taken to perform the DFT on a discrete signal.

The spectral analysis allows to identify the susceptibility of the system to control instabilities, as only the 1P frequencies should be reduced, with no effect on the remaining spectrum.

4.5.4. Dynamic Stall Onset

For the dynamic stall runs, a LEV is expected to form and then detach at some point during the cycle. The detection of this point accurately is far from the capabilities of the current measurement setup. However, some techniques based on pressure readings on an airfoil undergoing dynamic stall have already been proposed, and summarized in [50]. These techniques are based on the effect that the LEV has in the loads and pressure distributions when it detaches, and are presented in figure 4.6.

Not all the techniques presented in figure 4.6 are valid for detecting the onset of dynamic stall in the current experimental setup. The values of C_d and C_c are not measured with the current setup, and therefore techinques (c) and (d) cannot be employed. The data for the remaining techniques is available, but Sheng [50] defined this techniques for a ramp-up motion. The present experiment considers oscillating motions, and the LEV detaches both during the upstroke and downstroke, as it will be presented in the Results chapter. For the largest frequency, the loads are already decreasing before the detachment of the LEV, and the detection of the onset with techniques (a) and (f) becomes unfeasible. Technique (e) is chosen, based on the pressure data at $c/4$. The effect of the LEV detachment on the pressure at this point is the most noticeable, with a peak occurring as the LEV passes on top of it. Technique (b), based on the C_m, is not used for the lack of a precise definition of the threshold to detect

dynamic stall onset.

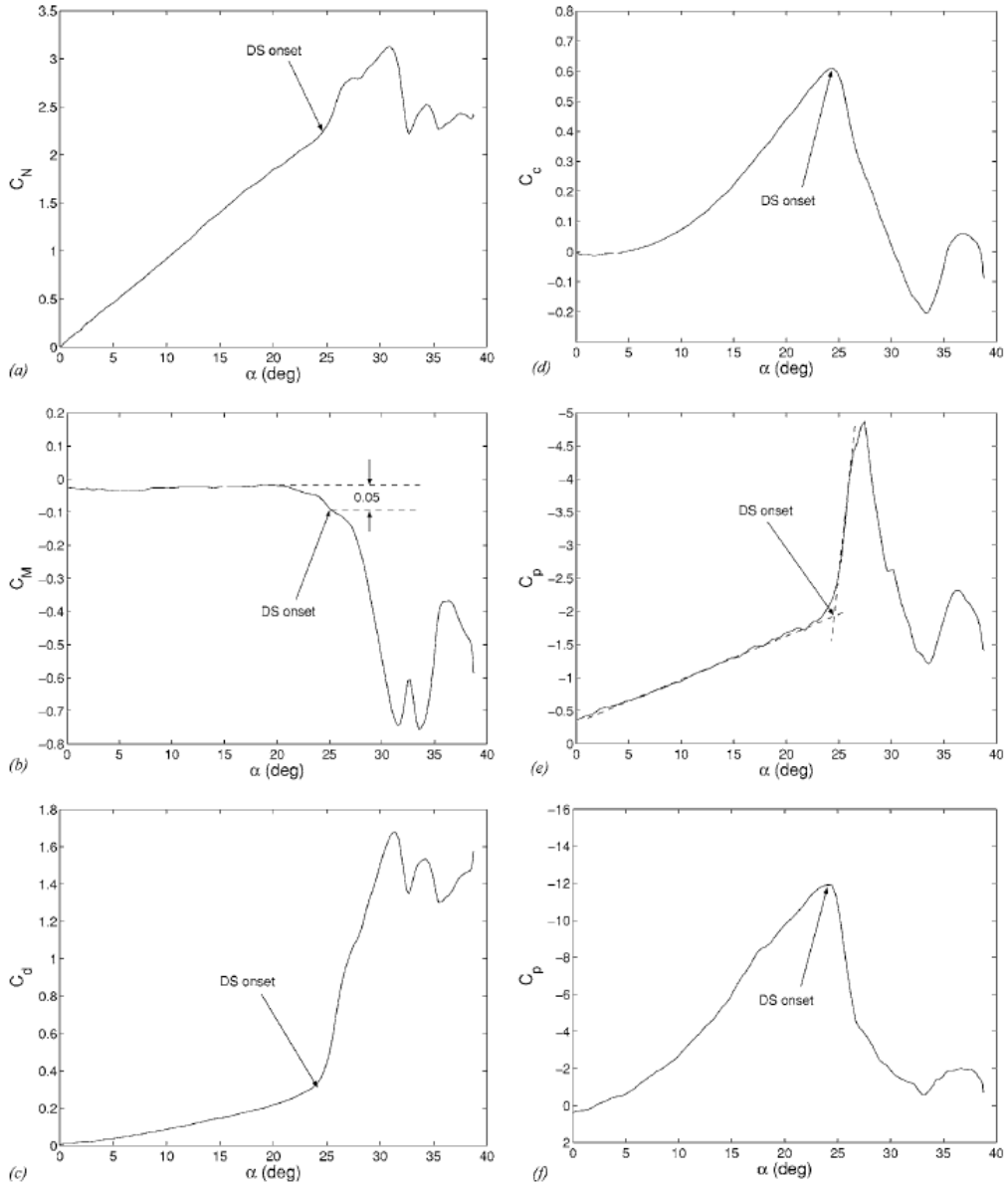

Figure 4.6: Detection of dynamic stall onset (DS Onset) based on pressure data. (a) Deviation of the C_N, (b) C_M break, defined as a drop of 0.05 (c) Deviation of the C_d (d) Maximum of C_c (e) C_p deviation at $c/4$ (f) Collapse of the C_p at the Leading Edge. Extracted from [50]

5

Baseline Results

The purpose of the present thesis is to assess the performance of the proposed controller for different conditions in terms of its load reduction capabilities. This is done by comparing the results obtained when the trailing edge flap is actively controlled with the results obtained for no flap actuation. The results corresponding to no flap actuation are presented during this chapter. A static characterization of the wing model is performed in section 5.1. In section 5.2, the dynamic results are presented. These results will serve as a baseline for quantifying the performance of the controlled cases. The most important flow features are described, both for the attached flow conditions in section 5.2.1, and for dynamic stall in section 5.2.2.

5.1. Static Characterization

The static loads and moments acting on the blade are studied for validation purposes. The turning table, which was introduced during chapter 3 is used to position the model at different angles of attack, from -22° to 22°. For the angles of attack where stall is expected to play an important role, two recordings are done: one before and one after stall has happened, in order to capture the hysteresis loop present in the loads due to the different points of separation and reattachment of the flow. For each angle of attack, the pressure data from the 24 transducers is stored for between 10-15 seconds. This results in around 400 measurements for each AOA. The data of every pressure transducer is averaged and integrated following the procedure described in 3.4.1 to obtain the lift and moment coefficients acting on the model.

The lift and moment coefficients are shown in figures 5.1 and 5.2 with respect to the angle of attack. The results for thin airfoil theory and for a viscous analysis performed with XFOIL (as described during section 4.1) are also shown. It should also be noted that there is a discrepancy between the position of the turning table and the actual angle of attack experienced by the airfoil. Since we are dealing with a fully symmetric airfoil, the lift generated when the wing is placed at 0° should be zero. This fact is used in order to correct for the discrepancy between the turning table and the actual angle of attack, and a shift of -0.22° is found. This shift is already accounted for in the results shown.

After the wind tunnel correction described in section 4.2 is applied, the agreement for the lift coefficient between the experimental results and the viscous analysis done with XFOIL is fairly good. Both results show a lift coefficient slope smaller than 2π, of around 1.8π. This was to be expected since we are dealing with a highly viscous flow, while thin airfoil theory assumes inviscid flow. Stall happens at a smaller angle of attack for the experimental results, showing an abrupt type of stall while XFOIL predicts a smoother stall. The experimental results show a hysteresis loop, which is obviously not predicted by XFOIL due to the intrinsic static nature of the code. The geometric static stall angle (when no wind tunnel corrections are applied) is $\alpha_{ss} \approx 17.5°$.

For the moment coefficient the agreement with thin airfoil theory is even smaller, since the thickness of the airfoil plays an important role here. Thin airfoil theory assumes a zero-thickness airfoil, and hence predicts zero pitching moment around the quarter-chord point throughout the range of angles

of attack. However, there are also discrepancies between the XFOIL analysis and the experimental results that are worth pointing out. A higher slope is found at small angles of attack in the experimental results, when the flow is still attached. This can be ascribed to the increased effective thickness of the airfoil due to the presence of the zig-zag strip.

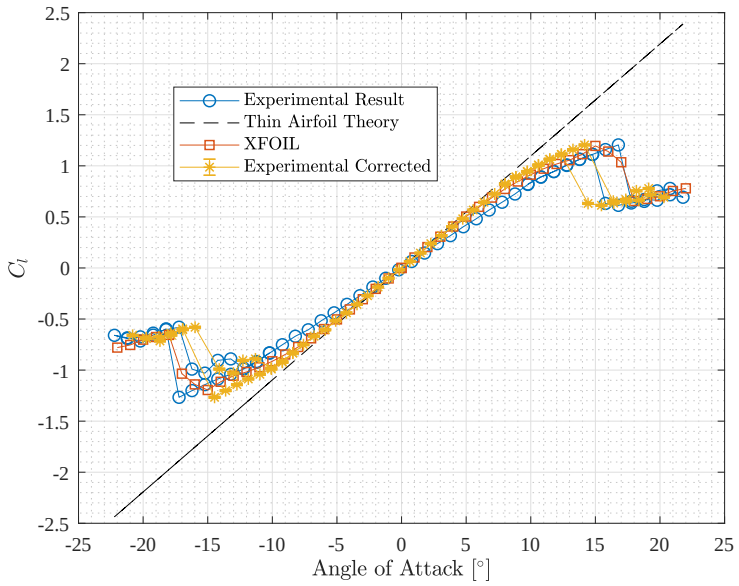

Figure 5.1: Lift coefficient of the NACA 0018. Comparison between Thin Airfoil Theory, XFOIL, and experimental results (with and without wind tunnel corrections)

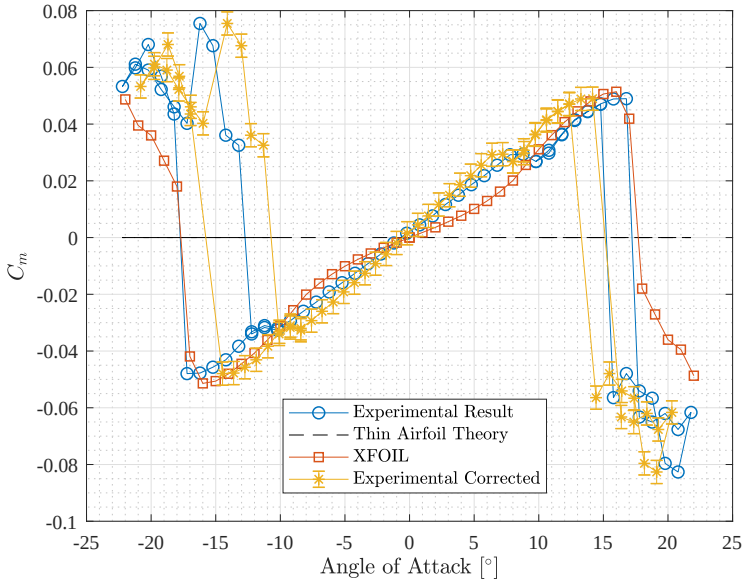

Figure 5.2: Pitching moment coefficient of the NACA 0018. Comparison between Thin Airfoil Theory, XFOIL, and experimental results (with and without wind tunnel corrections)

Regarding the uncertainty of the results, it is dominated by the bias errors, as described by equations 4.3 and 4.7. As such, $U_{\overline{C_l}} = 0.0086$ and $U_{\overline{C_m}} = 0.0037$ for every angle of attack.

5.2. Dynamic Characterization

The runs performed during the experiment (summarized in table 4.2), start with a case where the value of K_p of the controller is zero, and thus correspond to the baseline results. The results for the 8 pressure taps integration scheme are not shown here in detail, since reducing the number of pressure taps is done to reduce the time lag, and therefore is only expected to heavily influence the performance during the active load control cases, not the uncontrolled results.

As such the results shown here correspond to the two regimes analysed (attached flow and dynamic stall), for each of the three frequencies considered. The parameters of the cases are shown in table 5.1. For attached flow the mean angle of oscillations is $0.25°$, since an offset was found when analysing the loads, and a correction made for it. For dynamic stall conditions, $\alpha_0 = 15.75°$. This angle was chosen because it was found to be the optimal for a maximum number of dynamic stall cycles. However, from the small α_{amp}, not every cycle is representative of dynamic stall and therefore the procedure for cycle filtering shown in section 4.3.1 is followed.

	Attached flow	**Dynamic Stall**
α_0	0.25°	15.75°
α_{amp}	4°	4°
Frequency (k)	0.2 Hz (0.05)	0.2 Hz (0.05)
	0.4 Hz (0.1)	0.4 Hz (0.1)
	0.8 Hz (0.2)	0.8 Hz (0.2)
Time/case	120 sec	120 sec

Table 5.1: Parameters of the baseline cases (no active load control)

5.2.1. Attached flow

The baseline results for the attached flow conditions are shown here. The data for every pressure transducer is phase averaged, and then integrated into lift and moment coefficients. The moment coefficient is computed with respect to the pitching axis of the pitching table, which is located at 0.3125c. From now on the moment coefficient will always be computed with respect to this position.

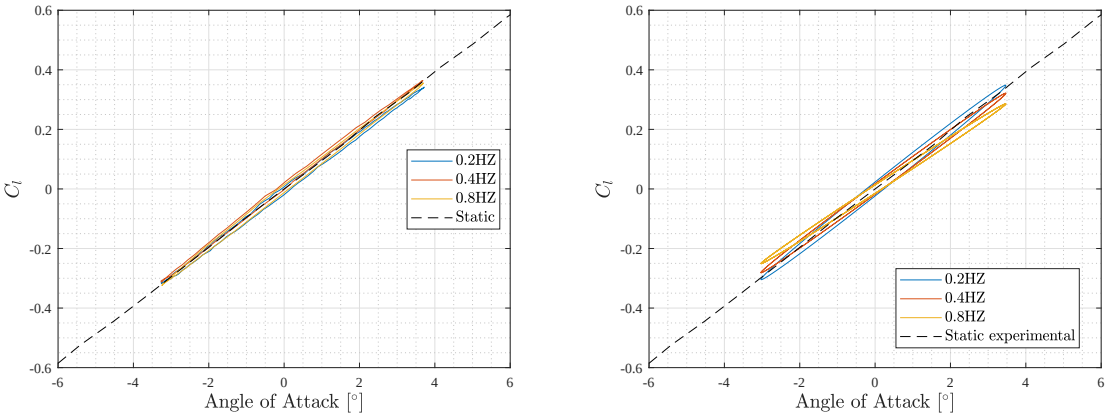

(a) Lift coefficient versus angle of attack obtained in the experiment

(b) Lift coefficient versus angle of attack as predicted by Theodorsen

Figure 5.3: Lift Coefficient experienced by the airfoil when subject to oscillations in the attached flow regime. Experimental results shown in 5.3a and Theodorsen in 5.3b, and compared to the static experimental results.

The results shown in the characterization of the static loads included the comparison with thin airfoil theory. For this case, Theodorsen theory can be used to predict the loads in an oscillating airfoil, as it

was discussed in section 2.1.1. This theory is implemented in Matlab and the results compared to the ones obtained in the experimental results, so they can be validated.

Figure 5.3a shows the lift coefficient obtained during the experimental runs at different frequencies, while figure 5.3b shows the lift coefficient predicted by using Theodorsen theory on an oscillating airfoil. Both results are compared to the experimental static lift coefficient obtained during the previous section.

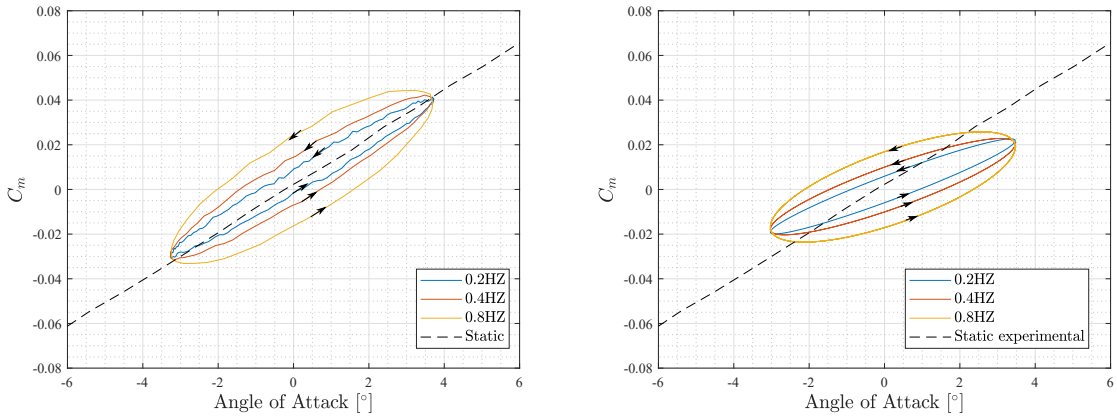

(a) Pitching moment coefficient versus angle of attack obtained in the experiment

(b) Pitching moment Coefficient versus Angle of attack as predicted by Theodorsen

Figure 5.4: Pitching moment coefficient experienced by the airfoil when subject to oscillations in the attached flow regime. Experimental results shown in 5.4a and Theodorsen in 5.4b, and compared to the static experimental results.

Several things have to be pointed out. First of all, the hysteresis is rather small for both the experimental results and Theodorsen theory, although in the experimental results all the loops are in counter-clockwise direction and for Theodorsen the lift loop at the largest reduced frequency is in the clockwise direction. Theodorsen predicts a reduction in the amplitude of the loads, as it can be seen in figure 5.3b, and This reduction increases for increased frequency, with the results for the smallest frequency (0.2Hz, corresponding to a reduced frequency $k = 0.05$) matching the static results. This reduction in amplitude of the lift is not seen in the experimental results, with the airfoil generating the same loading on the airfoil independently of the reduced frequency. It was observed that the presence of the zig-zag strip generates a second suction peak in the pressure coefficient distribution, and it is thought that the presence of the strip is the cause of this effect, although further investigation would be required to accurately determine this.

The pitching moment coefficient around the pitching axis, situated at 0.3125c, is shown in figure 5.4. Unlike in the lift coefficient results, large hysteresis loops can be appreciated for both the experimental data and Theodorsen, becoming larger for increased reduced frequency. The slope of these curves is larger in the experimental results, in accordance to the increased pitching moment with respect to the theoretical case observed in the static results. A way of quantifying the similarity between the results is looking into the aerodynamic damping coefficient, which is computed using the effective angle of attack, obtained after the wind tunnel corrections have been applied. The agreement between the theoretical aerodynamic damping coefficient and the one obtained in the experimental results is noticeable, seen in figure 5.5

It can be seen that there are considerable similarities between frequencies, with the main differences coming only from the value of the aerodynamic damping coefficient. The purpose of this baseline study is to generate a point of comparison for assessing the performance of the controller. This point of comparison will be the standard deviation of the lift being generated on the airfoil, which would translate into bending moments for a 3D wind turbine. The values of standard deviation of the lift coefficient for the different frequencies are presented in table 5.2. The values obtained for the 8 pressure tap integration scheme are also presented.

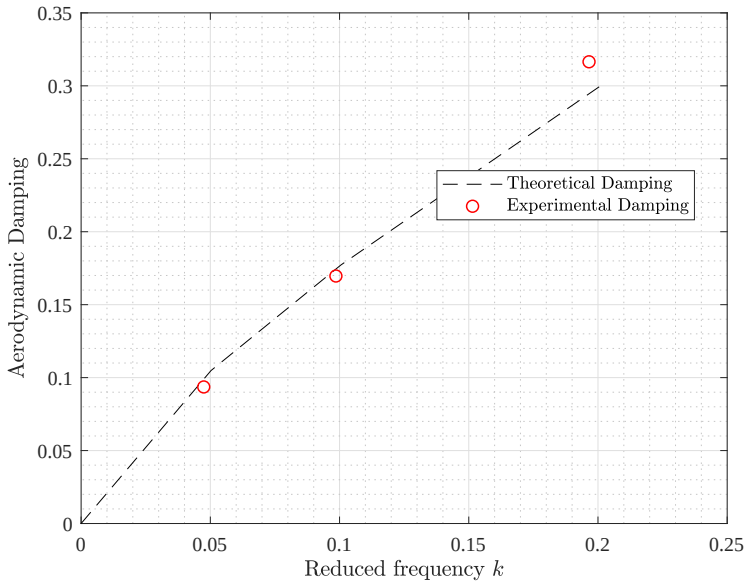

Figure 5.5: Aerodynamic damping coefficient obtained for the experimental results, and compared to the results predicted by Theodorsen theory

		0.2 Hz	0.4Hz	0.8Hz
$Std(C_l)$	24 taps	0.24	0.24	0.24
	8 taps	0.25	0.25	0.25

Table 5.2: Standard deviation of the C_l for the baseline results of the attached flow condition, for different frequencies and integration schemes

The uncertainties for the baseline results under attached flow conditions are still low, so their value is the same as the uncertainties in the static loads case, stemming from the bias errors.

5.2.2. Dynamic Stall

The baseline results for the dynamic stall runs are obtained following the same procedure described in the previous section, and employing the cycle filtering methodology for removal of unrepresentative cycles. However, unlike the previous results, where the difference between frequencies was small, each frequency experiences different types of dynamic stall. The phase-averaged lift coefficient for every frequency is shown in figure 5.6. As it can be seen, the differences between frequencies are considerable. The uncertainty of the results is shown with a shaded region around the phase-averaged value. It can be seen that the uncertainty of the results is reduced for increased frequency. This stems from the fact that the number of cycles employed for the phase-averaging procedure is increased. No wind tunnel corrections are applied to the dynamic stall cases.

The first thing that needs to be pointed out is the magnitude of the loads acting on the airfoil. The maximum C_l obtained during the static characterization in section 5.1 is 1.2. This value of lift coefficient is largely exceeded for the three cases, due to the development of the LEV that causes the flow to be attached at angles of attack larger than the static stall angle. The values of the maximum C_l for each of the baseline cases can be consulted in table 5.3.

The second noteworthy aspect is the position of this peak. For the frequencies of 0.2Hz and 0.4Hz it coincides with the detachment of the LEV, that increases the suction on the upper side of the airfoil

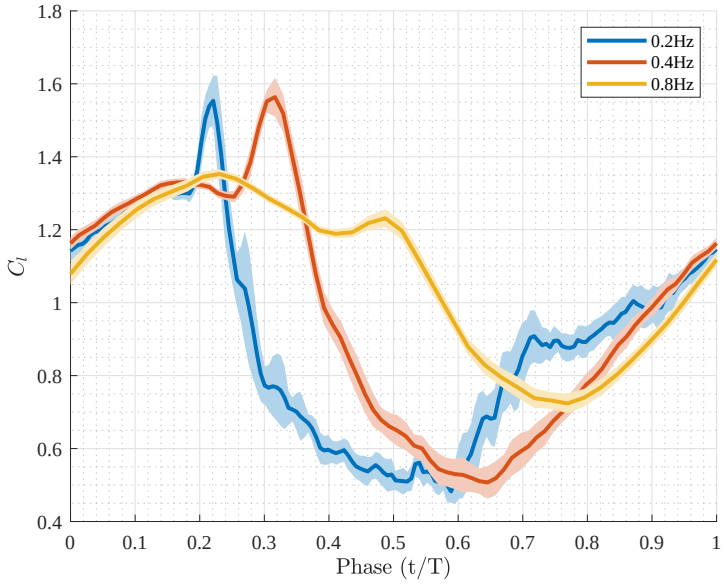

Figure 5.6: Phase-averaged lift Coefficient for the dynamic stall baseline cases for every frequency. Uncertainty of the results shown by the shaded region

as it convects downstream. However, the maximum peak observed at 0.8Hz does not appear due to the detachment of the LEV. The LEV is still attached to the leading edge of the airfoil. This generates that the wing reaches the maximum angles of attack without considerable flow separation, and this mechanism is responsible for the maximum C_l obtained at this frequency. A second C_l peak is observed at a later phase. This peak is the one originated by the detachment of the LEV. The methodology described in section 4.5.4 is followed to detect the dynamic stall onset (DS_{onset}), and shown in table 5.3. The dynamic stall cycle experienced at 0.8Hz is not representative of a typical dynamic stall cycle, if compared to literature (since detachment usually occurs before the downstroke and the flow is not fully detached after the LEV is convected downstream, observed in the smaller drop in loads and moments). Therefore, during the following chapter more emphasis will be placed on the regimes at 0.2Hz and 0.4Hz.

The development of dynamic stall results in an increase of unsteadiness of the loads experienced by the airfoil. This can be seen in the higher standard deviation of the results, as well as in the increased range of C_l experienced during the cycle (table 5.3). This is going to influence the performance of the controller, as it will be described in the next chapter, since the loads are too large for the load compensation capabilities of the trailing edge flap. The drop in loads is mainly attributed to the detachment of the LEV of the surface. The convective velocity of the dynamic stall vortex is supposed to be independent of the frequency of unsteadiness [27], and hence the load reduction capabilities are expected to be similar for 0.2Hz and 0.4Hz.

The phase-averaged moment coefficient is also shown in figure 5.7. The C_m has been plotted with respect to the geometric angle of attack of the model, to better understand the effect on the aerodynamic damping. Unlike in the attached flow regime, where the aerodynamic damping was always kept positive, the aerodynamic damping is negative for each case. This means that during the dynamic stall cycle the wing extracts energy from the flow. This can be observed from the fact that the moment loops in figure 5.7 are clockwise. The differences with the typical hysteresis loop found during dynamic stall, which can be seen in figure 2.4, have to be pointed out. Only the loop contributing to the negative aerodynamic damping is found in this experiment, and this is ascribed to the small amplitude of oscillations.

The onset of dynamic stall has been detected following the methodology described in section 4.5. It can be seen that for increased unsteadiness the detachment of the LEV occurs at a later phase of

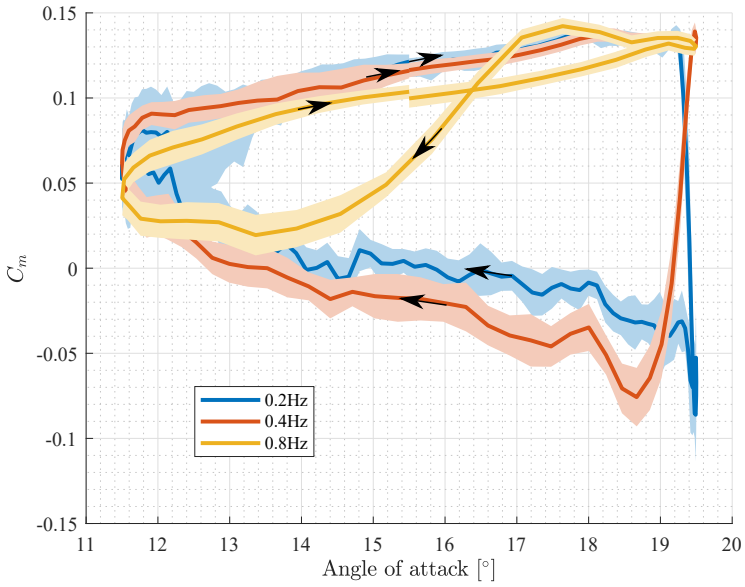

Figure 5.7: Phase-averaged moment Coefficient for the dynamic stall baseline cases for every frequency. Uncertainty of the results shown by the shaded region

	0.2Hz	**0.4 Hz**	**0.8Hz**
N_{cycles}	9	20	38
$C_{l,max}$	1.55	1.56	1.35
$C_{l,min}$	0.48	0.51	0.72
$C_{l,max} - C_{l,min}$	1.07	1.05	0.63
$Std(C_l)$	0.27	0.31	0.31
Ξ_{cycle}	-0.97	-1.16	-0.22
DS_{Onset}	0.18	0.26	0.39
Δt_{DS}	0.59s	0.47s	0.4s

Table 5.3: Characterization of the baseline case during dynamic stall conditions, for the frequencies tested

the oscillations cycle. However, the time elapsed since the static stall angle is surpassed until the LEV detaches (Δt_{DS}) is reduced with increased unsteadiness, and these results are in accordance with the findings of Mulleners and Raffel [44].

6

Controlled Results

After the baseline results, presented in chapter 5, and which correspond to no flap actuation, the results corresponding to active load control are shown in this chapter. The trailing edge flap is actuated by means of the controller, described in section 3.4, for different values of the proportionate gain. The ability of the controller to reduce the unsteady loads acting on the blade is evaluated. Different oscillation frequencies and control time lags are considered. The first results correspond to attached flow conditions, and are shown in section 6.1. After that, the results under dynamic stall conditions are presented in section 6.2.

6.1. Attached Flow

This section deals with the active load control results under attached flow conditions. The performance of the controller must be assessed so that the dynamic stall conditions can be tested. Emphasis will be placed on the role played by the frequency of unsteadiness and the time lags present in the control system. As it has been already described, the former will be done by actuating the pitching mechanism at frequencies of 0.2Hz, 0.4Hz and 0.8Hz (corresponding to a reduced frequency k of 0.05, 0.1 and 0.2). The latter will be done by employing two different integration schemes, with all 24 and just 8 pressure taps, that correspond to a time lag in the control loop of 32 ms and 12 ms respectively.

The controller is given a Set Point (SP) of zero, so the C_l wants to be kept at that value. Different proportional gains are tested for each run, and the performance of the controller for different values of K_p assessed. As it was observed during section 5.2.1, the loads experienced by the airfoil at different frequencies are really similar. Based on this, the frequency of 0.4Hz is taken as the point of reference, and an in-depth analysis is done for it. After that, a comparison between the results for the different frequencies is carried out.

6.1.1. Load Reduction Capabilities

During this subsection the performance of the controller is analysed for the frequency of 0.4Hz. This is done by following the methodology described in section 4.5. The results for both integration schemes are shown, which confirms the importance that the time lag has in the performance of any controller in charge of load alleviation.

The phase-averaged lift and moment coefficients for the 24 pressure tap integration scheme are shown in figures 6.1 and 6.2 respectively. This corresponds to Run 3 of the experiment, (refer to table 4.2). The baseline case, as presented in section 5.2 is shown, as well as the response of the system for different values of the proportionate gains.

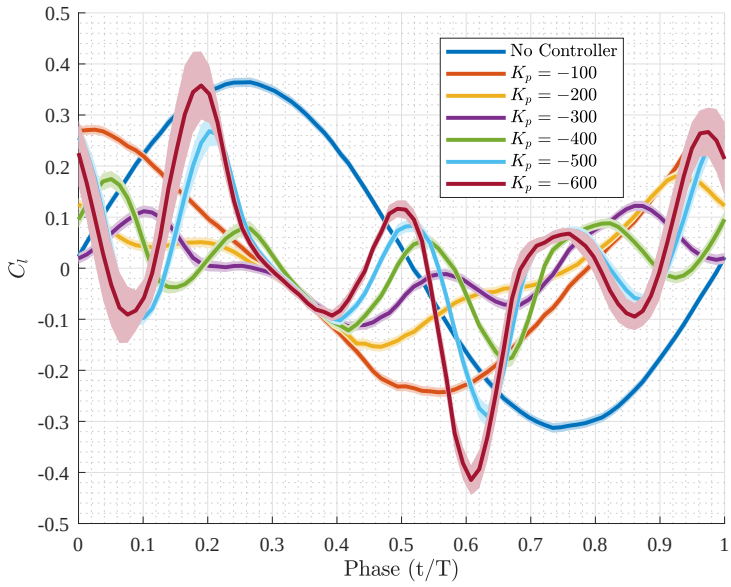

Figure 6.1: Phase-averaged lift coefficient under attached flow conditions for different values of K_p. 24 pressure tap integration scheme and f=0.4Hz. Shaded regions represent the uncertainty of the results at 95% confidence interval

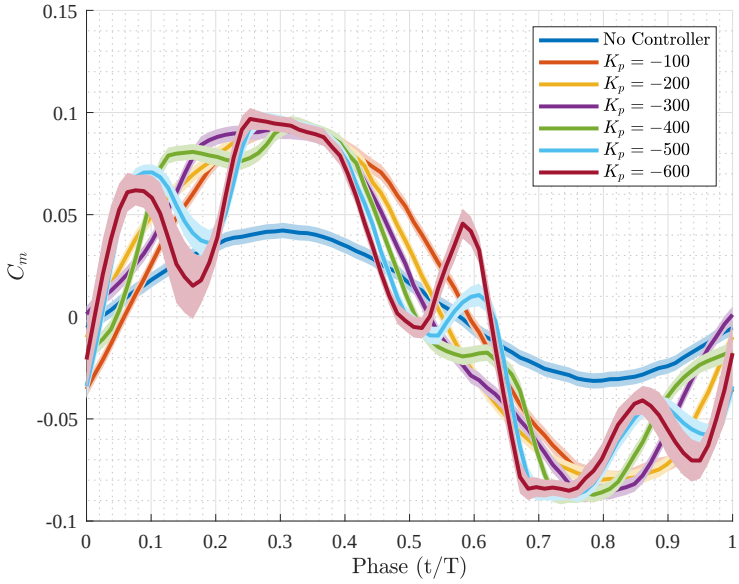

Figure 6.2: Phase-averaged moment coefficient under attached flow conditions for different values of K_p. 24 pressure tap integration scheme and f=0.4Hz. Shaded regions represent the uncertainty of the results at 95% confidence interval

The first aspect that needs to be pointed out is that the active load control results in an increase of the moment coefficient acting on the blade, as it is shown in figure 6.2. This would result in an increase of the torsional moment on a real wind turbine blade, and can be seen as one of the drawbacks of the Smart Rotor concept in general, as it was already reported in [10]. This can be attributed to the position of the aerodynamic center of the airfoil with respect to the elastic center, or pitching axis. For a standard configuration with the elastic center located behind the aerodynamic center, an increase of loads results in an increase of moment. Any control based on trailing edge flap actuation reacts to this by deflecting the flap upwards. This generates a further increase of moment by decreasing the loading on the rear part of the airfoil. An extra DOF, such as leading edge actuators would have to be

introduced, so that loads and moments can be tackled at the same time, although this would result in higher complexity.

Regarding the lift coefficient, the loads revolve closer around zero, which indicates that the controller is reducing their unsteadiness. The value of K_p heavily influences the performance though. The smaller gain tested, $K_p = -100$, reduces the loads only slightly, and does not cause oscillations, it just introduces a phase shift. Larger gains improve the performance in terms of reduction of the standard deviation of the results but introduce unwanted oscillations in the system. These higher-frequency oscillations grow in magnitude for increasing K_p, and also affect the performance of the system. An optimum proportional gain can thus be found, as the one that results in the smallest standard deviation of the lift coefficient. The standard deviation of the lift coefficient is presented in table 6.1, along with the values of the standard deviation of the moment coefficient.

	K_p						
	0	-100	-200	-300	-400	-500	-600
$Std(C_l)$	0.24	0.17	0.09	0.07	0.09	0.14	0.18
$Std(C_m)$	0.03	0.06	0.06	0.06	0.06	0.06	0.06

Table 6.1: Standard deviation of the C_l and C_m for different values of K_p using the 24 pressure tap integration scheme, under attached flow conditions

The optimal gain in terms of higher reduction of the standard deviation of the lift coefficient is found to be $K_p = -300$. Larger gains introduce higher frequency oscillations in the system and worsen the performance. In order to get some insight into the reduction capabilities of the proposed controller, a spectral analysis is carried out as described in section 4.5. Two cases are shown: the baseline case, and the case corresponding to $K_p = -500$, where load oscillations are found.

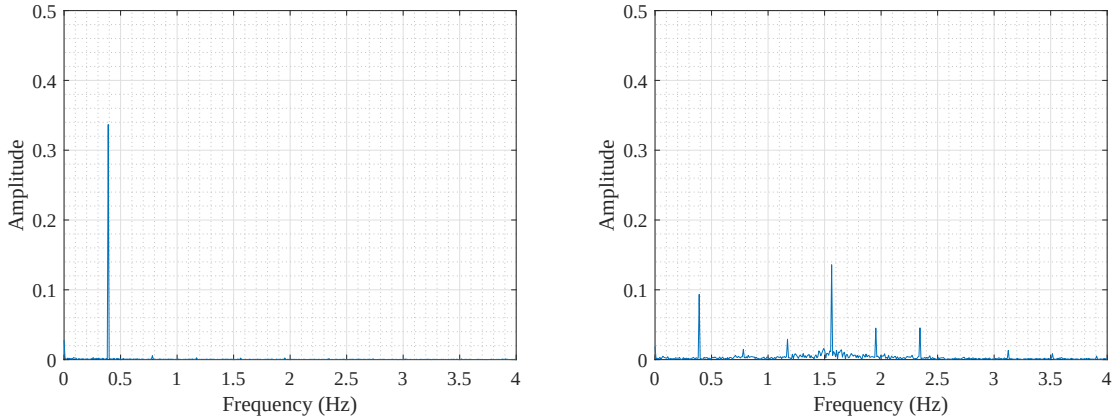

(a) Fast Fourier transform of the lift coefficient for the baseline case under attached flow conditions. f = 0.4Hz and 24 pressure taps integration scheme

(b) Fast Fourier transform of the lift coefficient for the case with $K_p = -500$ under attached flow conditions. f = 0.4Hz and 24 pressure taps integration scheme

Figure 6.3: Spectral analysis of the lift coefficient for the baseline Case (6.3a) and the active load control case with $K_p = -500$ 6.3b under attached flow conditions. f = 0.4Hz and 24 pressure taps integration scheme

The first peak, corresponding to the 1P frequency at 0.4Hz, is reduced for the controlled case (figure 6.3b) with respect to the baseline case (figure 6.3a). However, oscillations at higher frequencies are found. In particular, the 4P frequency, corresponding to 1.6Hz is largely excited. This excitation of higher-frequency harmonics is the reason of the worsened performance at large values of K_p.

In order to see the effect of the controller time lag, the results for Run 4, corresponding to a frequency of 0.4Hz and 8 pressure taps integration scheme, are shown. The phase-averaged lift coefficient is plot-

ted in figure 6.4 and the phase-averaged moment coefficient in figure 6.5. The performance is clearly improved, with larger reductions of the standard deviation of the lift coefficient for every value of K_p, as it is quantified in table 6.2. The effect on the moment coefficient is the same as for the 24 pressure tap integration scheme, with a constant increase for every value of K_p.

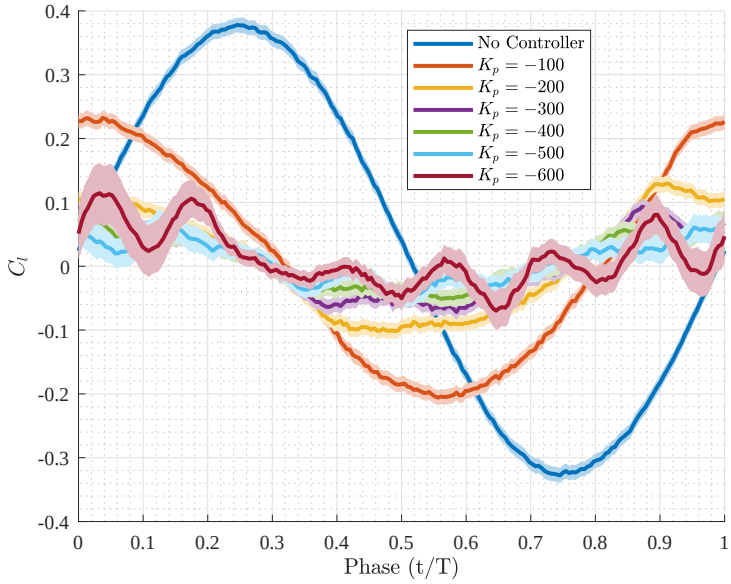

Figure 6.4: Phase-averaged lift coefficient under attached flow conditions for different values of K_p. 8 pressure tap integration scheme and f=0.4Hz. Shaded regions represent the uncertainty of the results at 95% confidence interval

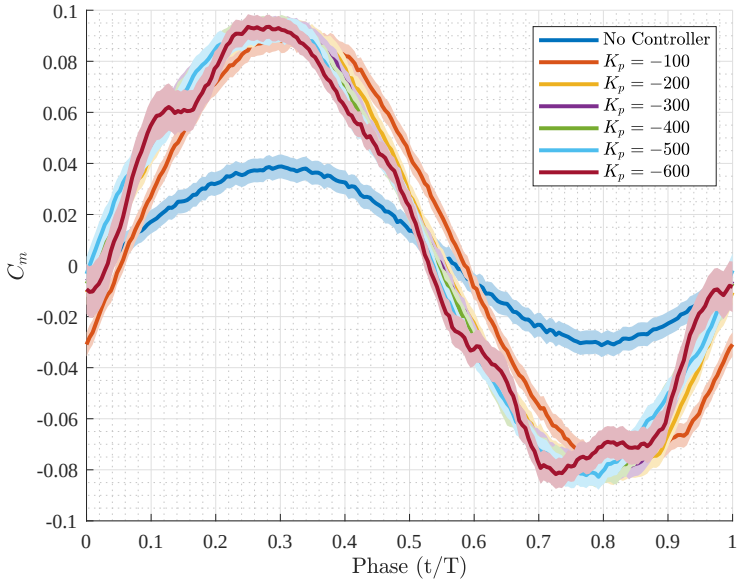

Figure 6.5: Phase-averaged moment coefficient under attached flow conditions for different values of K_p. 8 pressure tap integration scheme and f=0.4Hz. Shaded regions represent the uncertainty of the results at 95% confidence interval

An spectral analysis is also carried out for the same proportionate gain as it was done for the 24 pressure tap integration scheme, $K_p = -500$, and shown in figure 6.6, comparing the frequency spectrum of both integration schemes. Besides the larger reduction in the 1P frequency, reducing the time

	K_p						
	0	-100	-200	-300	-400	-500	-600
$Std(C_l)$	0.25	0.15	0.08	0.06	0.05	0.06	0.09
$Std(C_m)$	0.03	0.07	0.07	0.07	0.07	0.07	0.07

Table 6.2: Standard deviation of the C_l and C_m for different values of K_p using the 8 pressure tap integration scheme, under attached flow conditions

lag has an influence in the excitation of the harmonics. The large peak at the 4P frequency is not seen, and instead a small excitation is observed at around the 6P frequency. This leads to an improved performance and a smoother actuation of the flap.

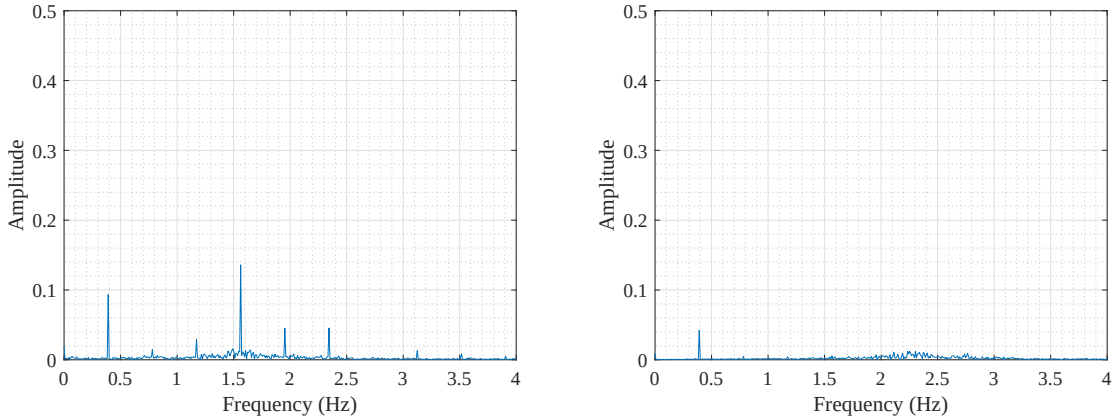

(a) Fast Fourier transform of the lift coefficient for $K_p = -500$. f = 0.4Hz and 24 pressure taps integration scheme. Attached flow conditions

(b) Fast Fourier transform of the lift coefficient for $K_p = -500$. f = 0.4Hz and 8 pressure taps integration scheme. Attached flow conditions

Figure 6.6: Spectral analysis of the lift coefficient for $K_p = -500$, employing the 24 pressure taps integration scheme (6.6a), and the 8 pressure taps one (6.6b). f=0.4Hz and attached flow conditions

6.1.2. Effect on Aerodynamic Damping

The effect that the active load control has on the aerodynamic damping experienced by the airfoil wants to be studied. Introducing another DOF may lead to instabilities even during attached flow conditions. This is quantified by the aerodynamic damping coefficient, and shown in figure 6.7 for different values of K_p.

The baseline case is positively damped, since a pitching motion under attached flow conditions cannot experience flutter, as described in section 2.1.3, and validated with the Theodorsen theory in section 5.2.1. Actuating the flap has a positive effect on the aerodynamic damping throughout the range of K_p tested. The airfoil is heavily damped for the smallest K_p, and increasing the value of the gain reduces the aerodynamic damping towards the baseline value. This stems from the fact that the smaller gains result in slow responses of the actuation system, and thus the flapping motion is lagging behind the pitching motion. The contribution of the flap deflection to the moment coefficient is thus also lagging, and this results in an increase of the aerodynamic damping, as it was explained when the aerodynamic damping was introduced in chapter 2. Larger values of K_p generate flap motions that get closer to being in-phase with the pitching motion, and therefore the contribution of the flap to the aerodynamic damping is much smaller, explaining the converging behaviour towards the baseline value observed for the 8 pressure tap integration scheme, since the flapping motion is not lagging any more. For the 24 pressure tap integration scheme, larger gains result in oscillations, which generate another increase in the aerodynamic damping.

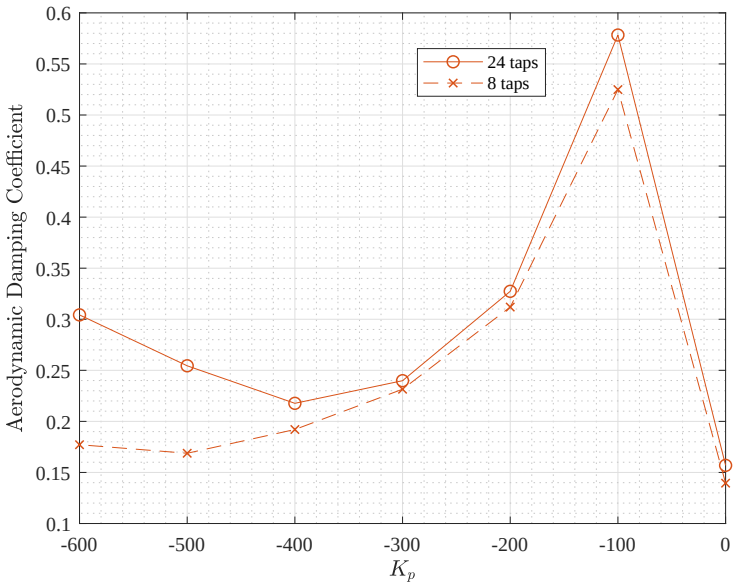

Figure 6.7: Phase-averaged moment coefficient for oscillations at 0.4Hz, employing the 8 pressure tap integration scheme, for different values of K_p. Shaded regions represent the uncertainty of the results

6.1.3. Frequency and Time Lag Comparison

In the previous section an in-depth analysis for a frequency of oscillations of 0.4Hz was carried out. The controller was found to be effective in reducing the loads on the airfoil, and an optimal K_p led to the highest reduction, while the moments acting on the blade were increased. Reducing the time lag also greatly improved the performance, with higher reductions and smaller excitation of higher harmonics. The effect on the aerodynamic damping was found to be either positive or negligible, depending on the gain of the controller.

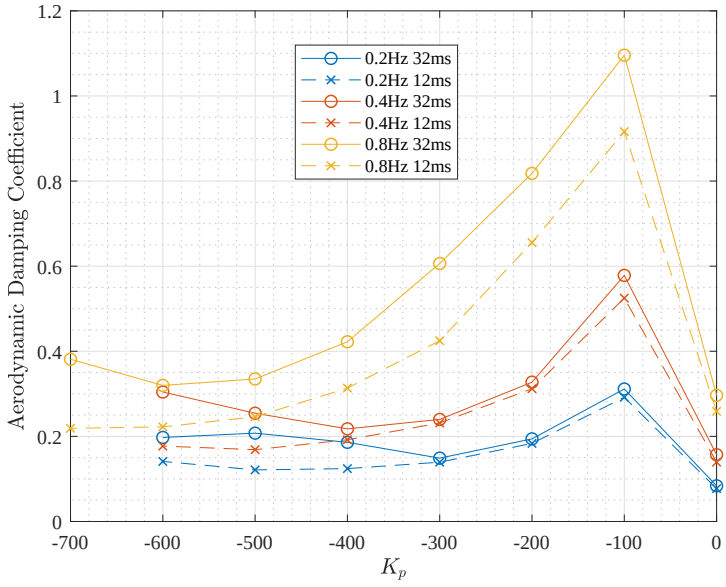

Figure 6.8: Aerodynamic damping coefficient Ξ_{cycle} for different values of K_p, frequencies and integration schemes, under attached flow conditions

A comparison of the aerodynamic damping obtained for different frequencies and values of K_p is

shown in figure 6.8. The behaviour is similar for every frequency: small proportional gains lead to an increased aerodynamic damping, due to the slow response of the flap. Increasing the K_p generates a faster response, and the trend is to converge to a value of aerodynamic damping close to the baseline one.

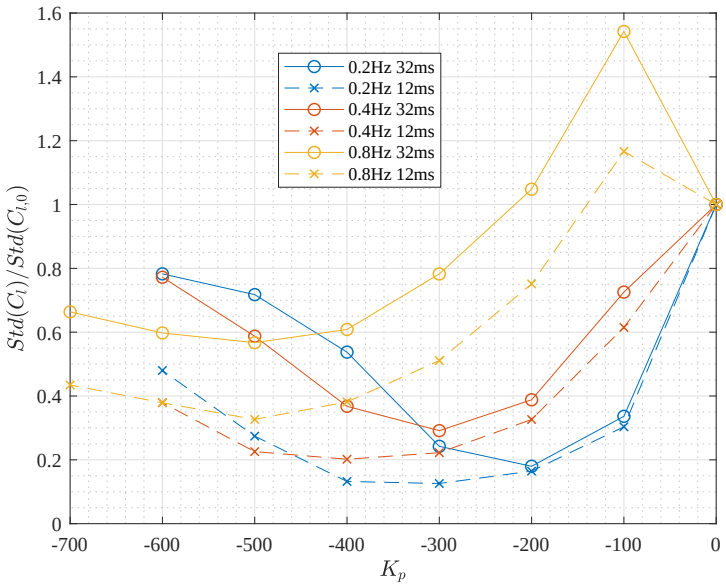

Figure 6.9: Standard deviation of the C_l with respect to the baseline case, for different values of K_p, frequencies and integration schemes, under attached flow conditions

The ability to reduce the loads acting on the airfoil is again measured with the standard deviation of the C_l with respect to the baseline case, and is shown in figure 6.9. Two trends can be extracted from this graph: reducing the time lag improves the performance for every frequency at every value of K_p. This puts forward the importance of reducing the time lags to a minimum in a Smart Rotor concept. Second, the maximum reduction of unsteady loads is decreased as the frequency increases for the same time lag. A maximum reduction of 87.5% is observed for the frequency of 0.2Hz, decreasing to 80% for 0.4Hz and 67.5% for 0.8Hz. Both the time scale of the oscillating loads and the time lag present in the system are paramount for its performance. The ratio of time lag to time scale should thus be kept to a minimum.

Regarding the spectral analysis carried out for the different frequencies, it is found that the harmonic frequency that is overly excited is only dependent on the time lag, and not on the frequency. For the 24 pressure tap integration scheme, this corresponds to a frequency of 1.6Hz, while for the 8 pressure tap integration scheme the excited frequency has a higher value of 2.4Hz. Therefore, reducing the time lag helps increase the value of this apparent resonance frequency of the system, and make the system less prone to control instabilities.

It should be pointed out is that the optimal value of the proportional gain increases with frequency. This was expected, since faster changes in loads require of faster actuation signals, and this is dictated by the value of the proportional gain. However, this value does not scale linearly with frequency. For the time lag of 12 ms, the optimal value of K_p is -300 for 0.2Hz, -400 for 0.4Hz and -500 for 0.8Hz. The optimal value of K_p is also dependent on the time lag present in the system, with smaller values for the time lag of 32 ms. One of the reasons for this behaviour is the susceptibility to instabilities as the value of K_p is increased, but further studies would have to be done in order to accurately quantify the relationship between the time lag, frequency, K_p and performance of the system. This is out of the scope of the present study, since the optimal controller is not the focus.

Summarizing, the proposed controller has been proven effective in reducing the loads appearing on a blade due to oscillations at reduced frequencies k of 0.05, 0.1 and 0.2 when small flow separation is expected. The time lag is paramount in the load reduction achieved, improving the load reduction capabilities and making the system more stable. The smallest time lag and frequency reach quite high reductions in the standard deviation of the C_l with respect to no flap actuation, 87.5%, which are in line with the values by Van Wingerden et al [60] of 90% load reduction (refer to the chapter 2 for more details on this study) . The drawback of the proposed controller is that it needs manual tuning to obtain the optimal gain value, K_p. However, since the load reduction capabilities are considerable and in accordance to available results, it is deemed an appropriate mechanism for active load reduction for the current setup, and the effect of a more complex flow such as dynamic stall on the control capabilities can be looked at. This is the focus of the next section, and builds up to answering the research questions layed out during chapter 2.

6.2. Dynamic Stall

This section deals with the runs performed under dynamic stall conditions. Similarly to the attached flow conditions, the ability of the controller to reduce the unsteady loads is assessed, as well as the influence of controller time lag and frequency of unsteadiness. The performance of such a controller in this regime has not been yet studied, and hence the novelty of the present study. The results for 0.4Hz are shown first, and the performance of the controller for different time lags assessed based on these results. After that, a comparison between the different frequencies tested is carried out. For every case, the SP of the controller is set to a C_l of 1.1, as the average of the mean value of the C_l for the baseline cases at the three different frequencies.

6.2.1. Load Altering Capabilities

The results for the phase-averaged C_l and C_m of the Run at 0.4Hz are shown here. The uncertainty of the results for a 95% confidence interval is shown in the figures as a shaded region.

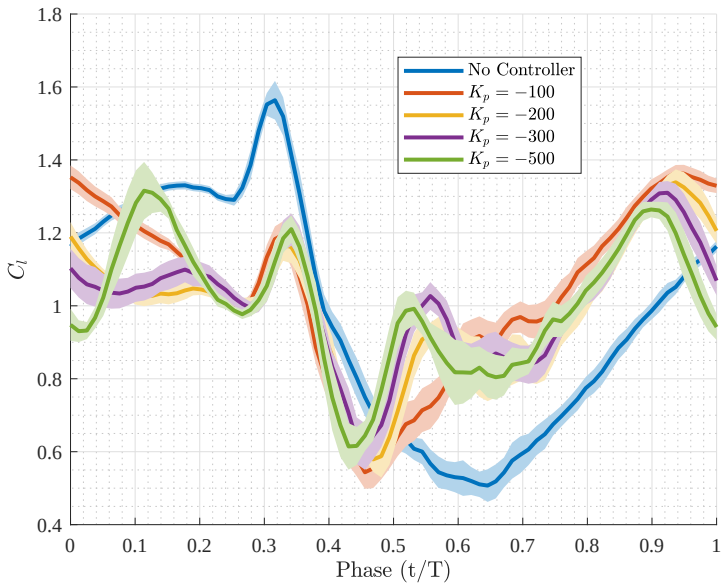

Figure 6.10: Phase-averaged lift coefficient under dynamic stall conditions for different values of K_p. 24 pressure tap integration scheme and f=0.4Hz. Shaded regions represent the uncertainty of the results at 95% confidence interval

The effectiveness of the controller in reducing the unsteady loads acting on the airfoil is seen in figure 6.10. Even though the unsteadiness in the C_l is still high, its value revolves closer around the SP of $C_l = 1.1$. The simple design of the controller is the reason for this: if the load is higher than the SP, the controller deflects the flap upwards, and vice versa. The flapping down motion always generate an

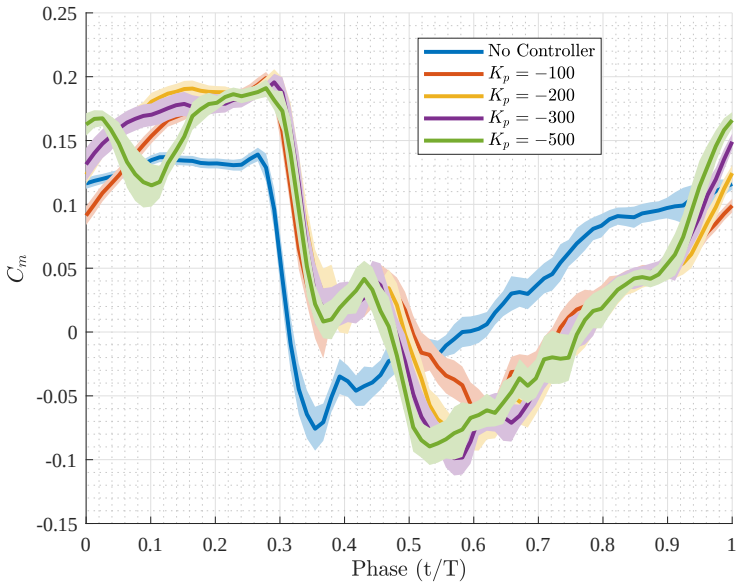

Figure 6.11: Phase-averaged moment coefficient under dynamic stall conditions for different values of K_p. 24 pressure tap integration scheme and f=0.4Hz. Shaded regions represent the uncertainty of the results at 95% confidence interval

increase of the loads acting on the airfoil, even if the flow is stalled.

The reduction in the standard deviation of the C_l is affected by the range of loads experienced during dynamic stall, which is considerably larger than during attached flow conditions and stems from the detachment of the LEV. This saturates the flap at $\pm$ 10°, and loads can not longer be reduced. This can be observed in figure 6.10 at a couple of points during the cycle: the flap is saturated before the detachment of the LEV, at $\phi \approx 0.3$, and the reduction of the peak C_l is thus limited. The second point where the flap is saturated is when the flow is completely stalled and the C_l of the baseline case reaches a minimum. This limits the maximum reduction in $Std(C_l)$ to around 40%, compared to a 70% reduction for attached flow conditions with the same frequency and time lag. However, the reduction is still noticeable and the controller works even when dealing with a complex flow such as dynamic stall.

	K_p				
	0	-100	-200	-300	-500
$Std(C_l)$	0.31	0.25	0.20	0.19	0.22
$Std(C_m)$	0.07	0.08	0.09	0.09	0.09
$C_{l,max}$	1.56	1.2	1.17	1.21	1.21
$C_{l,min}$	0.51	0.54	0.58	0.61	0.61
$C_{l,max} - C_{l,min}$	1.05	0.66	0.59	0.60	0.6

Table 6.3: Load reduction parameters for different values of K_p under dynamic stall conditions. 24 pressure tap integration scheme and f=0.4Hz

One of the other aspects that need to be pointed out is the peak-to-peak reduction of the loads. This reduction is also important when dealing with fatigue loads, as they are dependant on the amplitude of the oscillating loads. The reduction of the peak-to-peak change in lift is affected by the maximum velocity of actuation of the flap. For values of the K_p larger than -200, the actual velocity of the flap is not the imposed actuation signal, but rather the maximum velocity of the servo-flap linkage mechanism. This explains the similar range of loads for larger values of the K_p, as quantified in table 6.3. Faster actuators are expected to increase the optimal reduction of the loads, although the system may become susceptible to instabilities during the detachment of the LEV, since the actuation signal may

be too big. It can thus be concluded that the actuation system adopts an even bigger role when dealing with dynamic stall, stemming from the sudden drop in loads and increased range, so faster and larger actuators are needed to improve the load reduction capabilities under this regime.

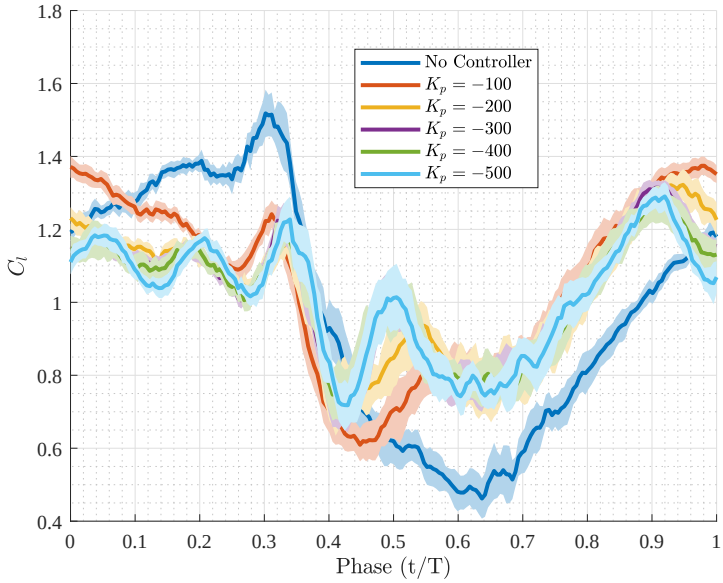

Figure 6.12: Phase-averaged lift coefficient under dynamic stall conditions for different values of K_p. 8 pressure tap integration scheme and f=0.4Hz. Shaded regions represent the uncertainty of the results at 95% confidence interval

The effect of the time lag is quantified by looking at the results for the 8 pressure tap integration scheme, which are shown in figure 6.12, and quantified in table 6.4. The behaviour is really similar to the 24 pressure tap integration scheme in terms of the reduction in the $Std(C_l)$. This is attributed to the increased range of loads, which cause the flap to be saturated at several points during the cycle. However, if the focus is shifted to the peak-to-peak loads, the effect of the reduced time lag is clearly seen. A higher value of the minimum C_l is obtained right after the detachment of the LEV is found. The values of the $C_{l,min}$ are shown in table 6.4, and are consistently higher than the ones obtained for the 24 pressure tap integration scheme, thereby reducing the peak-to-peak loads, and the susceptibility to fatigue. Even though the velocity of the flap is still saturated, the drop in lift is captured before due to the reduced time lag, and the flap deflection occurs earlier. This shows the importance of reducing the time lag for dynamic stall conditions, even though the reduction in the standard deviation of the C_l is similar for both cases. The peak-to-peak loads are reduced a maximum 44% for the 24 pressure tap integration scheme, and 57% for the integration scheme using just 8 pressure taps, for a frequency of 0.4Hz.

	K_p					
	0	-100	-200	-300	-400	-500
$Std(C_l)$	0.31	0.26	0.21	0.20	0.19	0.20
$Std(C_m)$	0.06	0.08	0.08	0.09	0.09	0.09
$C_{l,max}$	1.52	1.24	1.19	1.22	1.20	1.22
$C_{l,min}$	0.46	0.61	0.71	0.70	0.74	0.72
$C_{l,max} - C_{l,min}$	1.06	0.63	0.48	0.52	0.46	0.50

Table 6.4: Load reduction parameters for different values of K_p under dynamic stall conditions. 8 pressure tap integration scheme and f=0.4Hz

Besides the improved peak-to-peak reduction of the loads, the reduced time lag has an effect of the

susceptibility to control instabilities. An spectral analysis was carried out, and the same results were found as for attached flow conditions: the 24 pressure integration scheme excites the harmonic close to 1.6Hz, while the 8 pressure tap integration scheme excites the harmonics close to 2.4Hz. This is thought to appear during parts of the dynamic stall cycle where the flow is still attached, and the behaviour of the controller during these parts of the cycle is the same as for the attached flow conditions studied in the previous section. Since no real differences with the attached flow conditions were found, a more detailed study of the spectrum of the loads under dynamic stall conditions is not carried out.

Lastly, the effect of the active load control on the moment around the blade is also studied. This is shown in figure 6.11, and quantified in tables 6.3 and 6.4. The moment is constantly increased when the loads are actively controlled, as it occurred during attached flow conditions. This was already described as an unwanted consequence of this type of control, and more degrees of freedom would have to be introduced in the system if both loads and moments want to be controlled simultaneously.

6.2.2. Frequency and Time Lag Comparison

The performance of the controller in terms of load reduction capabilities for different frequencies is shown in figure 6.13, as the reduction of $Std(C_l)$ with respect to the baseline case. As it was pointed out in the previous section, the reduction values are lower than with attached flow conditions, although the controller is proven to reduce the unsteadiness of the loads throughout the range of frequencies tested. An interest aspect is that unlike for attached flow conditions, where the reduction of the standard deviation of the C_l was diminished for increased frequency, the best results for dynamic stall conditions are found for 0.8Hz. The reason behind this is the smaller range of loads experienced by the wing model: the difference between the maximum and minimum C_l is 0.63, while for the cases of 0.2Hz and 0.4Hz is higher than 1, as it was quantified in table 5.3. Besides, the drop in lift due to the detachment of the LEV is less abrupt due to this cycle being representative of a lighter type of dynamic stall. This generates a lift evolution that resembles more the purely sinusoidal motion of the attached flow regime, and thus explains the higher values of reductions.

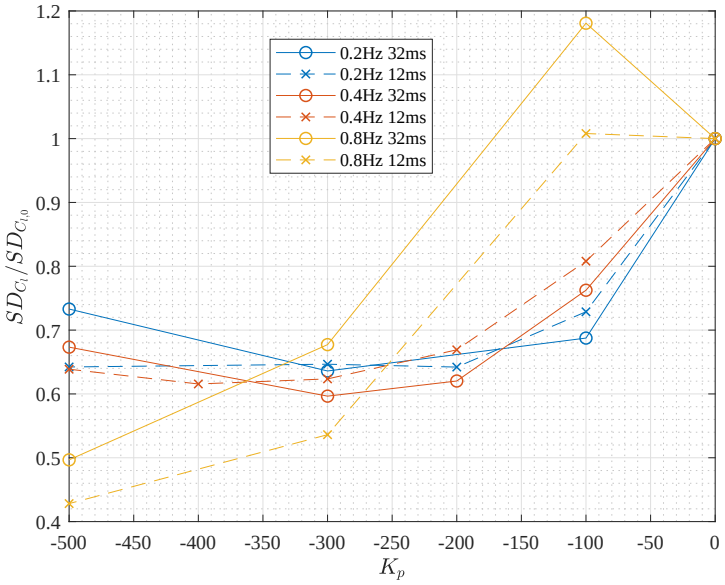

Figure 6.13: Standard deviation of the C_l with respect to the baseline Case, for different values of K_p, frequencies and integration schemes under dynamic stall conditions

The effects of the detachment of the LEV appear to be the driving force behind the load reduction capabilities of the controller under dynamic stall. Few differences can be observed between the frequencies of 0.2Hz and 0.4Hz, in terms of the reduction of the standard deviation of the C_l. This is ascribed again to the saturation of the flap, due to the increased range of loads, which is similar for

both cases. However, as it was seen in the previous section, the peak-to-peak loads may be a better indicative of the load reduction capabilities under dynamic stall, and especially during the detachment of the LEV. The optimal reduction expressed as a percentage of reduction of the peak-to-peak loads with respect to the baseline case is shown in table 6.5.

	$C_{l,max} - C_{l,min}/(C_{l,max} - C_{l,min})_{baseline}$	
	0.2 Hz	0.4 Hz
24 taps	51%	44%
8 taps	59%	57%

Table 6.5: Reduction of the peak-to-peak loads experienced during dynamic stall, for frequencies of 0.2Hz and 0.4Hz and time lags of 32ms and 12ms

These results are somewhat surprising, since the convection velocity of the LEV is expected to be invariant of the frequency [27], but higher reductions are observed for the case of 0.2Hz. However, the evolution of the C_l is different for each frequency. This is shown in figure 6.14 where the C_l of the baseline case is plotted with respect to the time elapsed since the maximum C_l is observed. In this figure it can be observed how the drop in loads is similar during the first 0.2 seconds after the peak C_l. If a convection velocity of $0.3V_\infty$ is assumed [27], as it has been consistently detected in literature, and the peak in loads assumed to occur when the LEV passes through the c/4 point, this implies that the LEV has fully convected downstream after 0.2 seconds. This coincides with the drop in loads experienced for both regimes, with the differences after those 0.2 seconds thought to appear due to different pitching motions. The performance of the controller under dynamic stall conditions appears to be driven first by the convective velocity of the LEV (frequency independent), and later by the motion of the wing (frequency dependent)

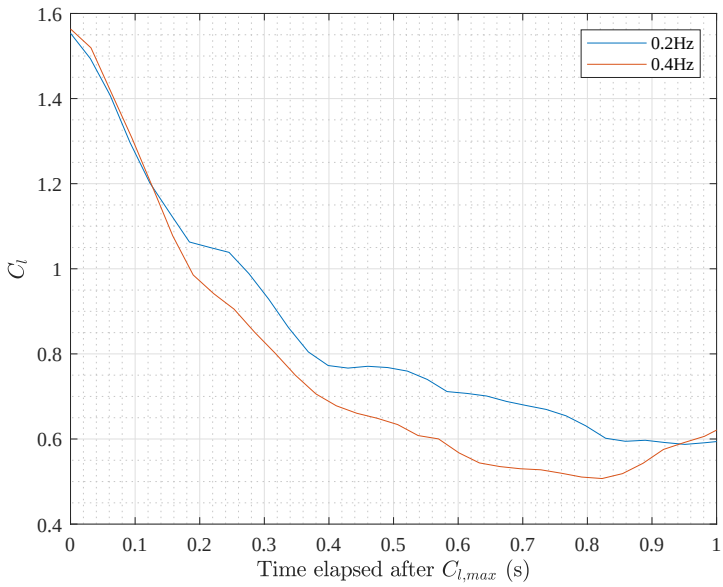

Figure 6.14: Evolution of the C_l with respect to the time elapsed since the maximum peak $C_{l,max}$, for the frequencies of 0.2Hz and 0.4Hz

6.2.3. Effect on Aerodynamic Damping

The effect of the flap actuation in the value of aerodynamic damping can be assessed by looking at figure 6.15. It was shown in section 5.2.2 that a negative aerodynamic damping was found for the dynamic stall cases, since the non-linear flow behaviour leads to the airfoil extracting energy from the

flow. The value of the aerodynamic damping for the baseline cases is frequency dependent. As it can be seen in figure 6.15, the effect of the active load control on the aerodynamic damping is also frequency dependent. For a frequency of 0.2Hz the aerodynamic damping is worsened, making it more susceptible to flutter. The effect is negligible for 0.4Hz, and a positive contribution to the aerodynamic damping is even found for a frequency of 0.8Hz.

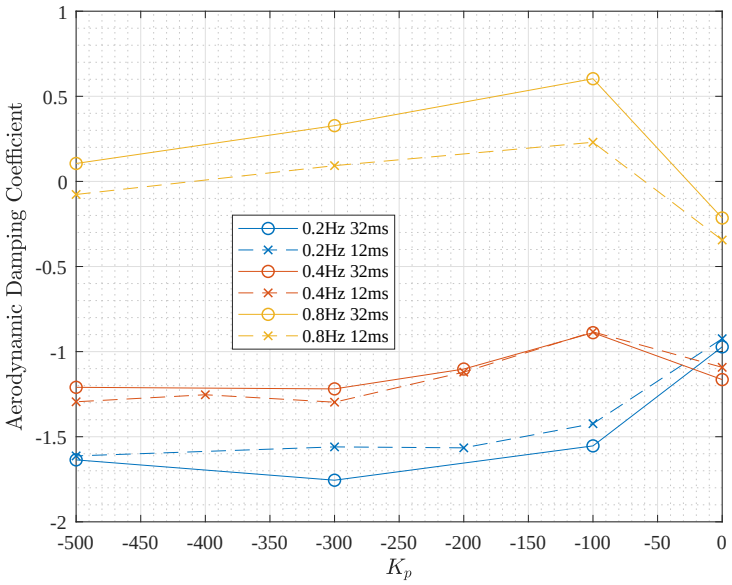

Figure 6.15: Aerodynamic damping coefficient Ξ_{cycle}, for different values of K_p, frequencies and integration schemes under dynamic stall conditions

The effect of the controller on the aerodynamic damping was found to be negligible during attached flow conditions. The motion of the flap, and hence the contribution to the moment coefficient, were almost in phase with the pitching motion of the whole model for the optimal values of K_p. However, this is not the case for dynamic stall conditions, since the optimal flap motion is highly dependent on the detachment of the dynamic stall vortex.

Figure 6.16 shows the contribution of the flap motion to the aerodynamic damping for the optimal value of K_p (defined as the largest reduction in $Std(C_l)$), at different frequencies, obtained using the methodology described in section 4.5. As it was discussed already, the effect on the aerodynamic damping is frequency-dependent. The flap reacts to the drop in lift by pitching down, and decreasing the C_m acting on the airfoil. The drop in lift occurs due to the detachment of the LEV, and this was shown to be frequency dependent on section 5.2.2.

For the frequency of 0.2Hz, the LEV detaches right before the start of the downstroke. Throughout the downstroke the C_m is decreased with respect to the baseline case, and this has a negative influence on the aerodynamic damping. The detachment of the LEV occurs at a later phase for the frequency of 0.4Hz, which delays this flapping down motion and hence the contribution of the flap to the aerodynamic damping at the beginning of the downstroke is positive, while later it becomes negative. For the largest frequency tested, 0.8Hz, the LEV detaches at an even later phase,which generates a big clockwise loop in the C_m, increasing the aerodynamic damping.

The effect of the controller on the aerodynamic damping depends thus on the type of dynamic stall. The one shown for 0.8Hz is expected to rarely appear for actual wind turbines, as it has already been discussed: it arises as a combination of the small amplitude of oscillations and large reduced frequency. The one studied for 0.2Hz is thought to be more representative, with the detachment of the LEV happening before the start of the downstroke. The aerodynamic damping is heavily worsened for

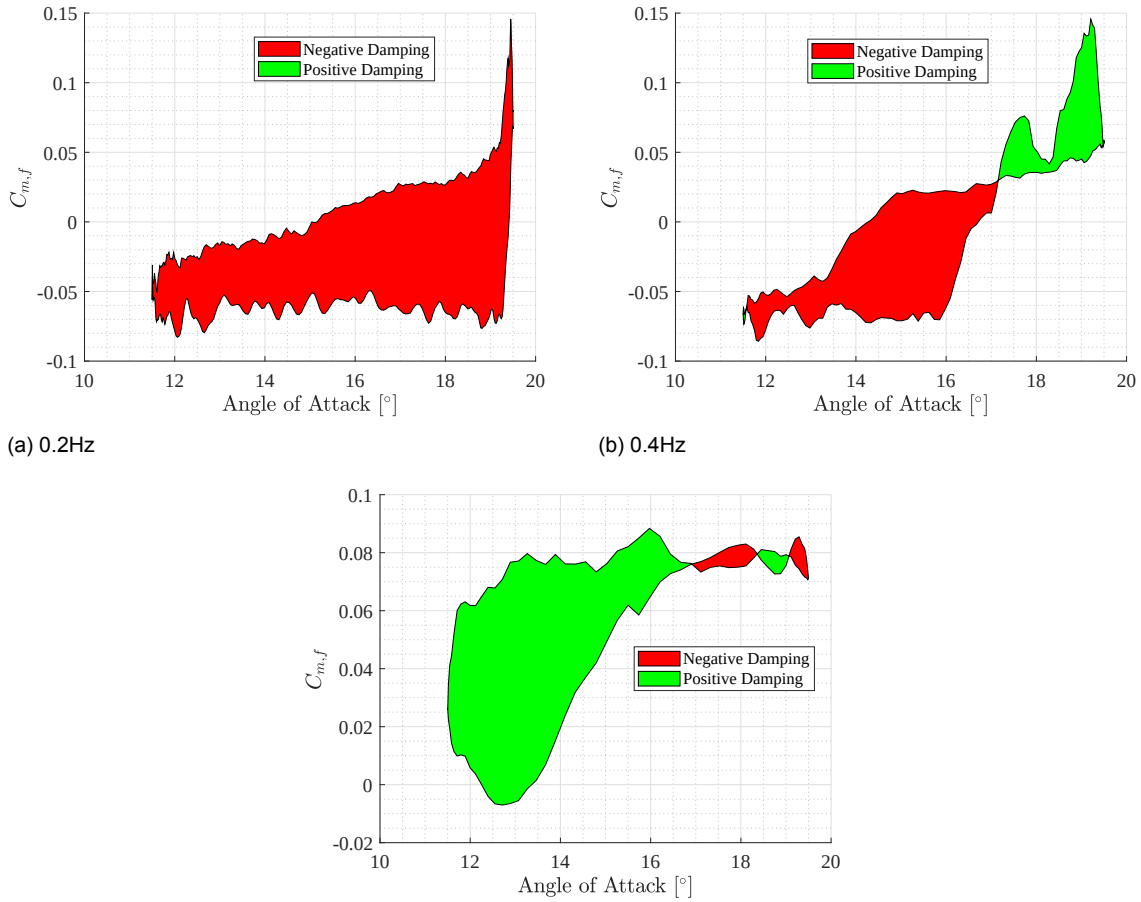

(a) 0.2Hz

(b) 0.4Hz

(c) 0.8Hz

Figure 6.16: Contribution of the flap motion to the C_m, as a function of the AOA of the model. Red regions indicate a negative contribution to the aerodynamic damping, while green regions indicate a positive contribution

this case. This brings forward the attention to one possible negative effect associated with this type of active load controller, which is the higher susceptibility to flutter if the inflow conditions result in dynamic stall conditions, even though the controller is able to reduce the loads experienced during dynamic stall. Unlike attached flow conditions, where the motion of the flap is dependent on the motion of the airfoil, in dynamic stall the motion of the flap is dictated by the detachment of the LEV. The phase at which this happens is thus going to influence the influence the active load control has on the aerodynamic damping.

6.2.4. Effect on Dynamic Stall Onset

Since dynamic stall is a leading-edge phenomenon, it is believed that a trailing edge actuation has little effect in the development of the cycle [35]. The onset of dynamic stall was studied by means of the methodology presented in section 4.5. In this section, the onset of dynamic stall (DS_{onset}) is studied for the optimal cases (largest reduction in $Std(C_l)$) and compared to the baseline case, to investigate the effect of the flap actuation on the dynamic stall cycle, apart from altering the loads.

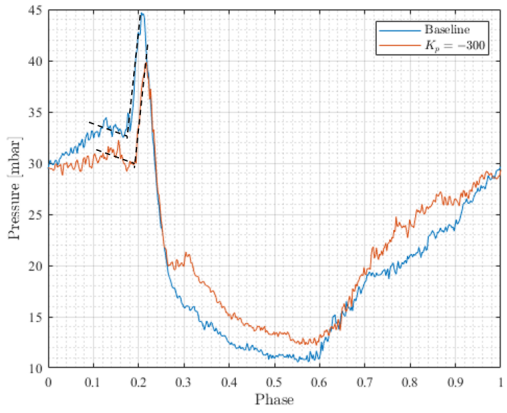

(a) 0.2Hz

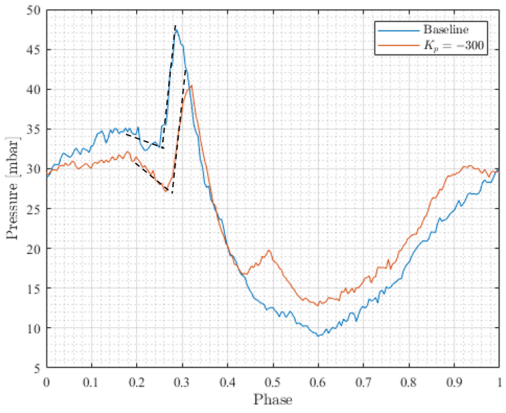

(b) 0.4Hz

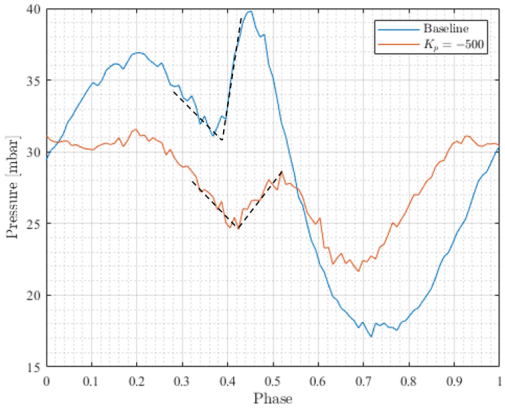

(c) 0.8Hz

Figure 6.17: Detction of onset of dynamic stall based on methodology by Sheng [50], from pressure at $c/4$. Comparison between baseline and optimal control case, for 0.2Hz (a), 0.4Hz (b) and 0.8Hz (c)

	DS_{onset} (Phase)		
	0.2Hz	**0.4Hz**	**0.8Hz**
Baseline case	0.18	0.26	0.39
Optimal case	0.19	0.28	0.42

Table 6.6: Phase when dynamic stall onset occurs, for the baseline case and the optimal case at different frequencies

Figure 6.17 shows the detection of the dynamic stall onset based on the pressure at the $c/4$, for the baseline case and the optimal case for each of the three frequencies. The values obtained are quantified in table 6.6. It can be seen how the onset of dynamic stall is consistently delayed for each of the three frequencies when the flap is actuated. Even though this effect is small, the flap actuation appears to affect the onset of dynamic stall. The hypothesis is that the actuation of the trailing edge flap delays the static stall angle of attack, since it deflects the flap upwards to reduce the loads acting on the airfoil when the flow is still attached, and that the dynamic stall onset starts developing after α_{ss} has been surpassed. This relationship between the static stall angle and the dynamic stall onset is not new [44, 50, 51], but it had not been considered before when studying the effect of trailing edge flaps in the development of dynamic stall to the author's knowledge.

7

Conclusions and Recommendations for Future Work

The present experimental study focus on the ability of a proportionate controller to reduce the unsteady loads appearing on a 2D-blade during dynamic stall conditions, by controlling the velocity of a trailing edge flap. This type of control is supposed to be representative of a Smart Rotor, and it is performed as the first step towards understanding the effect of this phenomenon on such a concept, since a lack of knowledge regarding this has been identified during the review of literature. In this chapter some conclusions and recommendations are drawn based on the findings of the study.

7.1. Conclusions

The proposed proportionate controller is first studied by oscillating it around an angle of 0°. The flow around the arfoil under these conditions is expected to be largely attached to the surface. This first part of the study is done in order to assess the validity of the proposed control as an active load control mechanism, so that the first research question can be answered:

Is a proportionate controller that is acting on the velocity of actuation of the flap a feasible control mechanism in terms of load reduction capabilities during attached flow conditions?

This question is answered by looking at the reduction in the standard deviation of the C_l with respect to the uncontrolled case. In order to fully quantify the performance of the controller, different controller time lags are studied (32ms and 12ms), as well as unsteadiness frequency (0.2Hz, 0.4Hz and 0.8Hz, corresponding to reduced frequency k of 0.05, 0.1, 0.2).

For the smaller time lag of 12 ms, the reduction in standard deviation of the C_l with respect to the baseline case is 87.5% for 0.2Hz, 80% for 0.4Hz and 67.5% for 0.8Hz. These values drop to 82% for 0.2Hz, 70% for 0.4Hz and 44% for 0.8Hz when the time lag in the control system is 32 ms. Besides the increased load reduction, the reduced time lag results in a system less prone to instabilities, since it is found that the time lag of 32 ms introduces large excitations of a resonance frequency around 1.6Hz.

Based on these findings, it can be concluded that a proportionate controller acting on the velocity of the flap is an effective mechanism for load reduction capabilities. Besides this, any system involved with active control of aerodynamic loads, such as a Smart Rotor, should place high emphasis in reducing the time lag present in the controller system, as this will improve its performance. The frequency of unsteadiness is also important, as the load reduction capabilities are deteriorated when the time scale of unsteadiness is decreased.

Once the first research question has been answered positively, the second research question can be investigated, which deals with the performance under dynamic stall conditions:

Is the controller capable of performing when dealing with a stalled flow, such as in the dynamic stall regime?

The same parametric study is performed under dynamic stall conditions, for variable unsteadiness frequency and controller frequency. These conditions are reproduced by oscillating the model at angles close to the static stall angle. The first conclusion that can be drawn from the results is that the proposed controller is able to reduce the loads during dynamic stall conditions, as shown by the reduction of the standard deviation of the C_l of between 35-40% for the cases at 0.2Hz and 0.4Hz.

The time lag is again found as an important parameter in the performance of the controller during dynamic stall. This is not shown in the reductions in the standard deviation of the C_l, but rather in the diminishing peak-to-peak observed in the lift during the detachment of the LEV associated with dynamic stall: This peak is reduced in 44% for the time lag of 32 ms, and increased to 57% when the time lag is reduced to 12 ms for the frequency of 0.4Hz, which highlights again the importance of reducing the time lag even for the control during dynamic stall conditions, as the drop in lift can be detected sooner. For a frequency of 0.2Hz, these reductions are increased to 51% for a time lag of 32ms and 59% for a time lag of 12ms. It is thought that the small differences appear since the drop in loads is first frequency independent as the LEV convects downstream, and dependent on the pitching motion once the LEV has fully convected downstream.

However, flap actuation has a negative effect in the cycle aerodynamic damping during the oscillations under dynamic stall conditions. This is a measure of the work extracted by the flow from the wing, and hence negative values imply a higher susceptibility to aero-elastic instabilities such as flutter. While the effect was found to be negligible during attached flow conditions, the alleviation of loads during dynamic stall at 0.2Hz deteriorates the value of the aerodynamic damping. This cycle is thought to be the most representative of the dynamic stall happening on a wind turbine, since the detachment of the LEV happens during the upstroke. This finding places attention in the use of a Smart Rotor for reducing loads under dynamic stall conditions. Even though the controller is able to reduce the loads acting on the blade, it may be at the cost of higher susceptibility to aero-elastic instabilities, since the optimal flap actuation is not in-phase with the pitching motion, but is dependent on the detachment of the LEV.

Lastly, the actuation of the flap has an effect on the development of the dynamic stall cycle, although this effect is small. As the flap is deflected to control the unsteady loads acting on the blade, the static stall angle is increased (since the flap is deflected upwards during the upstroke), and this consistently delays the onset of dynamic stall throughout the frequencies tested. This effect is pointed out, although has a negligible effect in the load reduction capabilities of the controller.

7.2. Recommendations for Future Work

A study with a simple proportionate controller on a 2D rigid blade has been performed. Such a simple setup is chosen due to the complexity of the phenomenon of dynamic stall, which is hard to study under 3D conditions. However, the conclusions extracted from this study have to be extrapolated to a real wind turbine. Several steps should thus be taken to fully understand the behaviour of a Smart Rotor under dynamic stall conditions.

It has been concluded that the one of the effects of an active load controller driving a trailing edge flap during dynamic stall conditions is the higher susceptibility to aero-elastic instabilities such as flutter. This is quantified by means of the aerodynamic damping, but the study is done in a rigid-wing. An elastic wing could be considered, and the unsteadiness of the flow generated by means of an unsteady inflow rather than oscillating the wing itself. In this way the full aero-elastic coupling could be studied, and the effect of the active load control on the aero-elastic instability of the system better assessed.

The obvious next step would be to test the performance of the controller on an actual wind turbine.

Oscillations could be introduced in the incoming flow, and pitch control used to position the blade so that the mean effective angle of attack experienced during the oscillations can promote the appearance of dynamic stall at some (or all) of the sections of the blade. Great effort should be expended on the design of such a setup, so that dynamic stall conditions can be studied, but it could help better quantify the fatigue loads introduced by such a condition and the ability of an active load controller to reduce the oscillating loads appearing on the wind turbine.

Lastly, it was observed during the review of literature that there is a lack of homogeneity in the Smart Rotor studies. A real effort should be expended into performing a full parametric study of the Smart Rotor capabilities. In this sense, it is recommended to use the same simulation tool, wind turbine, set of inflow conditions, sensing system, controller, and actuation system as a baseline. The influence of the different parameters can then be assessed accurately, by modifying the parameter to be studied, like for example the optimal form of control. Such a study should be done numerically, since it would be impossible to test such a variety of conditions in a wind tunnel.

Bibliography

[1] S Ahmed and MS Chandrasekhara. Reattachment studies of an oscillating airfoil dynamic stall flowfield. *AIAA journal*, 32(5):1006–1012, 1994.

[2] Peter Bjoern Andersen, Lars Henriksen, Mac Gaunaa, Christian Bak, and Thomas Buhl. Deformable trailing edge flaps for modern megawatt wind turbine controllers using strain gauge sensors. *Wind Energy: An International Journal for Progress and Applications in Wind Power Conversion Technology*, 13(2-3):193–206, 2010.

[3] Peter Bjørn Andersen, Mac Gaunaa, Christian Bak, and Thomas Buhl. Load alleviation on wind turbine blades using variable airfoil geometry. In *Proceedings of the EWEC*, 2006.

[4] Christian Bak, Mac Gaunaa, Peter B Andersen, Thomas Buhl, Per Hansen, and Kasper Clemmensen. Wind tunnel test on airfoil risø-b1-18 with an active trailing edge flap. *Wind Energy: An International Journal for Progress and Applications in Wind Power Conversion Technology*, 13 (2-3):207–219, 2010.

[5] Thanasis K Barlas and Gijs AM van Kuik. Review of state of the art in smart rotor control research for wind turbines. *Progress in Aerospace Sciences*, 46(1):1–27, 2010.

[6] TK Barlas, GJ Van der Veen, and GAM Van Kuik. Model predictive control for wind turbines with distributed active flaps: incorporating inflow signals and actuator constraints. *Wind Energy*, 15(5): 757–771, 2012.

[7] Santiago Basualdo. Load alleviation on wind turbine blades using variable airfoil geometry. *Wind Engineering*, 29(2):169–182, 2005.

[8] Dale E Berg, Jose R Zayas, Donald W Lobitz, CP van Dam, Raymond Chow, and Jonathon P Baker. Active aerodynamic load control of wind turbine blades. Technical report, Sandia National Lab.(SNL-NM), Albuquerque, NM (United States), 2007.

[9] Leonardo Bergami and Niels K Poulsen. A smart rotor configuration with linear quadratic control of adaptive trailing edge flaps for active load alleviation. *Wind Energy*, 18(4):625–641, 2015.

[10] Lars O Bernhammer, Gijs AM van Kuik, and Roeland De Breuker. Fatigue and extreme load reduction of wind turbine components using smart rotors. *Journal of Wind Engineering and Industrial Aerodynamics*, 154:84–95, 2016.

[11] Gunjit Bir. Multi-blade coordinate transformation and its application to wind turbine analysis. In *46th AIAA aerospace sciences meeting and exhibit*, page 1300, 2008.

[12] T Brooks, M Marcolini, and D Pope. Airfoil trailing edge flow measurements and comparison with theory, incorporating open wind tunnel corrections. In *9th Aeroacoustics Conference*, page 2266, 1984.

[13] Thomas Buhl, Mac Gaunaa, and Christian Bak. Potential load reduction using airfoils with variable trailing edge geometry. *Journal of Solar Energy Engineering*, 127(4):503–516, 2005.

[14] Tony Burton, David Sharpe, and Nick Jenkins. *Handbook of wind energy*. John Wiley & Sons, 2001.

[15] CP Butterfield, WP Musial, and DA Simms. Combined experiment phase 1. final report. Technical report, National Renewable Energy Lab., Golden, CO (United States), 1992.

[16] Franklin O Carta and Charles F Niebanck. Prediction of rotor instability at high forward speeds. volume 3. stall flutter. Technical report, UNITED TECHNOLOGIES CORP STRATFORD CT SIKORSKY AIRCRAFT DIV, 1969.

[17] Damien Castaignet, Thanasis Barlas, Thomas Buhl, Niels K Poulsen, Jens Jakob Wedel-Heinen, Niels A Olesen, Christian Bak, and Taeseong Kim. Full-scale test of trailing edge flaps on a vestas v27 wind turbine: active load reduction and system identification. *Wind Energy*, 17(4):549–564, 2014.

[18] Zhenrong J Chen, Karl A Stol, and Brian R Mace. System identification and controller design for individual pitch and trailing edge flap control on upscaled wind turbines. *Wind Energy*, 19(6): 1073–1088, 2016.

[19] Raymond Chow and Cornelis van Dam. Computational investigations of deploying load control microtabs on a wind turbine airfoil. In *45th AIAA aerospace sciences meeting and exhibit*, page 1018, 2007.

[20] Thomas C Corke and Flint O Thomas. Dynamic stall in pitching airfoils: aerodynamic damping and compressibility effects. *Annual Review of Fluid Mechanics*, 47:479–505, 2015.

[21] Robert Dudley. *The biomechanics of insect flight: form, function, evolution*. Princeton University Press, 2002.

[22] Charles P Ellington. The novel aerodynamics of insect flight: applications to micro-air vehicles. *Journal of Experimental Biology*, 202(23):3439–3448, 1999.

[23] Wind Europe. Wind in power: 2016 european statistics. *Bruksela: Wind Europe*, 2017.

[24] BF Ewald. Wind tunnel wall corrections (la correction des effets de paroi en soufflerie). Technical report, ADVISORY GROUP FOR AEROSPACE RESEARCH AND DEVELOPMENT NEUILLY-SUR-SEINE (FRANCE), 1998.

[25] Peter Fuglsang, Ioannis Antoniou, Niels N Sørensen, and Helge Aagaard Madsen. *Validation of a wind tunnel testing facility for blade surface pressure measurements*. 1998.

[26] D. Giaquinta. The flow topology of the ahmed body in cross-wind. Master's thesis, TU Delft, the Netherlands, 2017.

[27] RB Green, RA McD Galbraith, and AJ Niven. Measurements of the dynamic stall vortex convection speed. *The Aeronautical Journal*, 96(958):319–325, 1992.

[28] Benjamin Heine, Karen Mulleners, Gilles Joubert, and Markus Raffel. Dynamic stall control by passive disturbance generators. *AIAA journal*, 51(9):2086–2097, 2013.

[29] Ivo Houtzager, Jan-Willem van Wingerden, and Michel Verhaegen. Rejection of periodic wind disturbances on a smart rotor test section using lifted repetitive control. *IEEE Transactions on Control Systems Technology*, 21(2):347–359, 2012.

[30] Scott J Johnson, Jonathon P Baker, CP Van Dam, and Dale Berg. An overview of active load control techniques for wind turbines with an emphasis on microtabs. *Wind Energy: An International Journal for Progress and Applications in Wind Power Conversion Technology*, 13(2-3):239–253, 2010.

[31] Jason Jonkman, Sandy Butterfield, Walter Musial, and George Scott. Definition of a 5-mw reference wind turbine for offshore system development. Technical report, National Renewable Energy Lab.(NREL), Golden, CO (United States), 2009.

[32] Tan Kok Kiong, Wang Qing-Guo, Hang Chang Chieh, and Tore J Hägglund. *Advances in PID control*. Springer, 1999.

[33] Matthew A Lackner and Gijs van Kuik. A comparison of smart rotor control approaches using trailing edge flaps and individual pitch control. *Wind Energy: An International Journal for Progress and Applications in Wind Power Conversion Technology*, 13(2-3):117–134, 2010.

[34] Matthew A Lackner and Gijs AM van Kuik. The performance of wind turbine smart rotor control approaches during extreme loads. *Journal of solar energy engineering*, 132(1):011008, 2010.

[35] Tim Lee and Panayiote Gerontakos. Dynamic stall flow control via a trailing-edge flap. *AIAA journal*, 44(3):469–480, 2006.

[36] Gordon J Leishman. *Principles of helicopter aerodynamics*. Cambridge university press, 2006.

[37] JG Leishman. Dynamic stall experiments on the naca 23012 aerofoil. *Experiments in Fluids*, 9 (1-2):49–58, 1990.

[38] RR Leknys, M Arjomandi, RM Kelso, and CH Birzer. Dynamic stall flow structure and forces on symmetrical airfoils at high angles of attack and rotation rates. *Journal of Fluids Engineering*, 141 (5):051104, 2019.

[39] William Levine and Michael Athans. On the determination of the optimal constant output feedback gains for linear multivariable systems. *IEEE Transactions on Automatic control*, 15(1):44–48, 1970.

[40] LEM Lignarolo, D Ragni, C Krishnaswami, Qing Chen, CJ Simão Ferreira, and GJW Van Bussel. Experimental analysis of the wake of a horizontal-axis wind-turbine model. *Renewable Energy*, 70:31–46, 2014.

[41] William J McCroskey. The phenomenon of dynamic stall. Technical report, National Aeronuatics and Space Administration Moffett Field Ca Ames Research …, 1981.

[42] William J McCroskey. Unsteady airfoils. *Annual review of fluid mechanics*, 14(1):285–311, 1982.

[43] Robert J Moffat. Describing the uncertainties in experimental results. *Experimental thermal and fluid science*, 1(1):3–17, 1988.

[44] Karen Mulleners and Markus Raffel. The onset of dynamic stall revisited. *Experiments in fluids*, 52(3):779–793, 2012.

[45] RPL Nijssen and Povl Brøndsted. Fatigue as a design driver for composite wind turbine blades. In *Advances in wind turbine blade design and materials*, pages 175–209. Elsevier, 2013.

[46] Weronika N Nowicka, Bing Chu, Owen R Tutty, and Eric Rogers. Load reduction in wind turbines with smart rotors using trial varying iterative learning control law. In *2017 American Control Conference (ACC)*, pages 1377–1382. IEEE, 2017.

[47] John G Proakis. *Digital signal processing: principles algorithms and applications*. Pearson Education India, 2001.

[48] Marco Raiola, Andrea Ianiro, Stefano Discetti, Thijs Gillebaart, Daniele Ragni, Gijs van Kuik, and Jan-Willem van Wingerden. Smart rotor: controlling dynamic stall by means of an actuated flap. In *8th AIAA Flow Control Conference*, page 4242, 2016.

[49] Marco Raiola, Stefano Discetti, Andrea Ianiro, Farid Samara, Francesco Avallone, and Daniele Ragni. Smart rotors: Dynamic-stall load control by means of an actuated flap. *AIAA Journal*, 56 (4):1388–1401, 2017.

[50] W Sheng, RA McD Galbraith, and FN Coton. A new stall-onset criterion for low speed dynamic-stall. 2006.

[51] W Sheng, RA Galbraith, and FN Coton. Prediction of dynamic stall onset for oscillatory low-speed airfoils. *Journal of Fluids Engineering*, 130(10), 2008.

[52] Derek E Shipley, Mark S Miller, and Michael C Robinson. Dynamic stall occurrence on a horizontal axis wind turbine blade. Technical report, National Renewable Energy Lab., Golden, CO (United States), 1995.

[53] Georgios Sieros, Panagiotis Chaviaropoulos, John Dalsgaard Sørensen, Bernard H Bulder, and Peter Jamieson. Upscaling wind turbines: theoretical and practical aspects and their impact on the cost of energy. *Wind energy*, 15(1):3–17, 2012.

[54] Christoph Stangfeld, Christopher L Rumsey, Hanns Mueller-Vahl, David Greenblatt, C Nayeri, and Christian O Paschereit. Unsteady thick airfoil aerodynamics: experiments, computation, and theory. In *45th AIAA Fluid Dynamics Conference*, page 3071, 2015.

[55] Karl Stol, Hans-Georg Moll, Gunjit Bir, and Hazim Namik. A comparison of multi-blade coordinate transformation and direct periodic techniques for wind turbine control design. In *47th AIAA Aerospace Sciences Meeting including the New Horizons Forum and Aerospace Exposition*, page 479, 2009.

[56] Theodore Theodorsen and WH Mutchler. General theory of aerodynamic instability and the mechanism of flutter. 1935.

[57] Owen Tutty, Mark Blackwell, Eric Rogers, and Richard Sandberg. Iterative learning control for improved aerodynamic load performance of wind turbines with smart rotors. *IEEE Transactions on Control Systems Technology*, 22(3):967–979, 2013.

[58] CP Van Dam, R Chow, JR Zayas, and DE Berg. Computational investigations of small deploying tabs and flaps for aerodynamic load control. In *Journal of Physics: Conference Series*, volume 75, page 012027. IOP Publishing, 2007.

[59] Jan-Willem Van Wingerden, Anton Hulskamp, Thanasis Barlas, Ivo Houtzager, Harald Bersee, Gijs van Kuik, and Michel Verhaegen. Two-degree-of-freedom active vibration control of a prototyped “smart” rotor. *IEEE transactions on control systems technology*, 19(2):284–296, 2011.

[60] JW Van Wingerden, AW Hulskamp, T Barlas, B Marrant, GAM Van Kuik, D-P Molenaar, and M Verhaegen. On the proof of concept of a ‘smart’wind turbine rotor blade for load alleviation. *Wind Energy: An International Journal for Progress and Applications in Wind Power Conversion Technology*, 11(3):265–280, 2008.

[61] Jan Robert Wright and Jonathan Edward Cooper. *Introduction to aircraft aeroelasticity and loads*, volume 20. John Wiley & Sons, 2008.